ENHANCED PHOTODETECTORS OF MOS_2 WITH PLASMONIC NANOARRAYS AND SI/SI STRUCTURES BY REACTIVE PULSED LASER DEPOSITION

By

Haojun Wang

A DISSERTATION

Submitted to
Michigan State University
in partial fulfillment of the requirements
for the degree of

Electrical Engineering – Doctor of Philosophy

2023

ABSTRACT

This Ph.D. dissertation presents two novel approaches in the field of materials science and nanotechnology. The first part introduces an integrated photodetector design that combines a two-dimensional material, MoS_2, with plasmonic structures. Nanoantenna arrays (NAs) are positioned above and below the MoS_2 layer to enhance the electric field, reducing the gap between the NA layers to the nanometer scale. The fabrication process of the NAs/MoS_2/NAs photodetector is detailed, encompassing the transfer of MoS_2 nanosheets, patterning of NAs, and alignment of the top layer NAs. The characterization of the fabricated photodetector includes the morphology analysis of MoS_2, Raman spectrum evaluation, and scanning electron microscope imaging. Finite difference time domain (FDTD) simulations investigate the plasmonic enhancement mechanism, revealing the distribution of electric field enhancement and absorption for different incident light polarizations. The results demonstrate a significant local electric field enhancement at the nanoantenna interface, with an enhancement factor of up to 25. These findings substantiate the potential of the proposed integrated photodetector for enhanced optical field and absorption, which can be leveraged in photodetection and nonlinear optical processes.

The thesis then investigates the electrical characterization of MoS_2-based photodetectors, focusing on photosensitivity and optimization parameters. Experimental measurements of photoconductivity, resistance, and photocurrent under laser-on and laser-off conditions reveal increased photosensitivity with laser power and applied bias voltage. By incorporating NAs on the top and bottom, the electron-hole pair generation is enhanced and resistance is reduced. Moreover, intentional adjustments are made to increase the lateral distance and size of the NAs to specifically focus on the nanoscale vertical gap and eliminate the lateral gap effect during the experiment. The study identifies the optimized conditions for high net photocurrent and minimal power consumption. The NAs/MoS_2/NAs device exhibits the highest responsivity among the tested devices, providing insights into the electrical characteristics of MoS_2-based photodetectors.

Next, the thesis explores the nonlinear absorption behavior of NAs integrated devices, in bare MoS_2, NA/MoS_2, and NA/MoS_2/NA layouts. Hyperspectral stimulated Raman scattering

(hsSRS) imaging is employed to investigate the impact of the layered nanostructure on nonlinear absorption. Experimental results reveal distinct absorption characteristics in bare MoS_2, NA/MoS_2, and NA/MoS_2/NA regions for various beam separation times. The double-layered NA/MoS_2/NA structure exhibits the strongest two-photon absorption (2PA) and demonstrates the influence of pulse timing on the nonlinear absorption process. The exceptional nonlinear optical properties observed in the NA/MoS_2/NA structure make it a promising candidate for various applications, including near-infrared detection, energy harvesting, and spectroscopy of organic materials.

On the second part of the dissertation, a novel technique called reactive pulsed laser deposition of SiC is introduced, enabling precise and controlled deposition of large amount of SiC particles. The technique utilizes a pulsed laser to generate a localized hot spot on a target source, leading to the ejection of sillicon (Si) and carbon (C) atoms towards a substrate through laser-induced plasma expulsion. The ejected atoms combine to form SiC nanoparticles, which condense onto the substrate surface, allowing for selective local processing and pre-patterned shape printing. The fabricated SiC particles exhibit interesting photoluminescent properties and enable the fabrication of a diode with distinct current rectification behavior. The experimental results demonstrate the effectiveness of the reactive pulsed laser deposition technique in achieving controlled SiC deposition, showcasing its potential for advancing SiC-based electronic devices and structures.

This Ph.D. thesis contributes to the understanding of integrated photodetectors, nonlinear optical effects, and precise material deposition techniques. The findings pave the way for enhanced optical field and absorption in photodetection, nonlinear optical processes, SiC-based devices, and offer opportunities for various research fields.

To my family, whose unwavering support and encouragement have been my guiding light throughout this journey. Your love and belief in me have been my constant motivation.

And to all the mentors, educators, and friends who have shaped my academic path, thank you for your guidance, knowledge, and inspiration. This dissertation is a testament to the collective effort that has brought me to this point.

ACKNOWLEDGEMENTS

I am filled with a profound sense of gratitude as I reflect upon the completion of my doctoral journey. This milestone would not have been possible without the unwavering support, guidance, and encouragement of numerous individuals who have played pivotal roles in shaping my academic and personal growth. I would like to express my heartfelt appreciation to the following individuals:

First and foremost, I extend my deepest gratitude to my esteemed advisor, Professor Timothy Hogan and Lixin Dong. Their exceptional expertise, intellectual guidance, and constant encouragement have been invaluable throughout my research. Their unwavering belief in my abilities, insightful feedback, and tireless dedication have shaped me into the researcher I am today. I am truly honored to have had the opportunity to work under their mentorship.

I would like to express my sincere appreciation to the members of my dissertation committee, Professor Qihua Fan, Virginia Ayres, and Shiyou Ding. Their insightful comments, constructive criticism, and scholarly expertise have significantly enriched my research. I am grateful for their time, commitment, and valuable contributions to the development and refinement of my work.

My deepest gratitude goes to my loving family. Their unwavering support, encouragement, and belief in my abilities have been the foundation of my success. I am forever grateful for their sacrifices, understanding, and constant motivation throughout this demanding journey. Their love, guidance, and unwavering presence have given me the strength to persevere and overcome challenges.

To my cherished friends, thank you for your unwavering support, laughter, and shared experiences. Your presence has brought joy, camaraderie, and a sense of belonging to my life. I am grateful for the moments of respite, encouragement, and celebration we have shared along this demanding path. Your friendship has been a source of inspiration and has made this journey more meaningful.

To my beloved Feng Zhao, your unwavering love, support, and understanding have been my anchor throughout this arduous endeavor. Your patience, encouragement, and belief in my abilities have given me the strength to overcome challenges and persevere. Your unwavering presence and

unwavering belief in me have made this journey more meaningful and rewarding. I am deeply grateful for your unwavering support and for being my source of inspiration.

I extend my gratitude to the faculty and staff at Michigan State University for their dedication to fostering a stimulating academic environment. Their commitment to excellence in teaching, research, and professional development has greatly contributed to my growth as a scholar.

I am grateful to the ECE department for their financial support, which has allowed me to focus on my research and academic pursuits. Their investment in my work has been instrumental in the successful completion of this thesis.

I would like to express my sincere appreciation to the participants who generously contributed their time and expertise to my research. Their involvement and willingness to share their insights and experiences have significantly enriched the findings of my study.

Lastly, I would like to acknowledge all the individuals who have supported me in ways both big and small, directly or indirectly, throughout this journey. Your words of encouragement, acts of kindness, and belief in my abilities have made an indelible impact on my personal and professional growth.

To everyone mentioned above and to those whose names may not appear here but have contributed to my journey, I offer my deepest gratitude. Your support, guidance, and belief in my abilities have been vital in helping me reach this significant milestone in my academic career.

I dedicate this thesis to my advisor, committee members, family, friends, and loved ones. Your unwavering support and belief in me have been my constant inspiration. Thank you for accompanying me on this remarkable journey and for making it truly extraordinary.

TABLE OF CONTENTS

LIST OF TABLES

LIST OF FIGURES

LIST OF ABBREVIATIONS

2D Two-Dimensional

2PA Two-Photon Absorption

AFM Atomic Force Microscopy

Al Aluminum

APBs Anti-phase Boundaries

a-Si Amorphous Silicon

CMOS Complementary Metal-Oxide-Semiconductor

CVD Chemical Vapor Deposition

CO_2 Carbon Dioxide

Cr Chromium

CW Continuous Wave

D Beam Diameter

DI Deionized Water

DFT Density Functional Theory

DOE Diffractive Optical Elements

EBL Electron Beam Lithography

Edmund Optics A company specializing in optics products

FDTD Finite Difference Time Domain Simulation

FET Field-Effect Transistor

GaAs Gallium Arsenide

GaN Gallium Nitride

HEMTs High-Electron-Mobility Transistors

hsSRS Hyperspectral Stimulated Raman Scattering System

ICs Integrated Circuits

IPA Isopropyl Alcohol

IV Current-Voltage

J Leakage current density

LDR Light-Dependent Resistor

LSPR Localized Surface Plasmon Resonance

LO Longitudinal Optical mode

MALDI Matrix-Assisted Laser Desorption/Ionization

MAPLE Matrix Assisted Pulsed Laser Evaporation

MBE Molecular Beam Epitaxy

MMICs Monolithic Microwave Integrated Circuits

MoS_2 Molybdenum Disulfide

MOSFETs Metal-Oxide-Semiconductor Field-Effect Transistors

MTs Micro-twins

NA Nanoantenna

Nd-YAG Neodymium-doped Yttrium Aluminum Garnet

NV Nitrogen Vacancy

PECVD Plasma-Enhanced Chemical Vapor Deposition

PL Photoluminescence

PLA Pulsed Laser Ablation

PLAL Pulsed Laser Ablation in Liquid

PLD Pulsed Laser Deposition

PMMA Polymethyl Methacrylate

PSN Polyureasilazane

PVP Polyvinylpyrrolidone

RF Radio Frequency

SEG Selective Epitaxial Growth

S_n Sample with n-type doped silicon substrate

S_p Sample with p-type doped silicon substrate

SAB Surface-Activated Bonding

SEM Scanning Electron Microscope

Si Silicon

SiC Silicon Carbide

Si-SiC Silicon-Silicon Carbide hybrid system

SPPs Surface Plasmon Polaritons

TEOS Tetraethyl Orthosilicate

TO Transverse Optic mode

T Temperature

TMDCs Transition Metal Dichalcogenides

UHV Ultra-high Vacuum

UV Ultraviolet

CHAPTER 1

INTRODUCTION

1.1 Motivation

Semiconductor nanotechnology has witnessed remarkable advancements in recent years, offering tremendous potential for revolutionizing various scientific and technological domains. The ability to engineer and manipulate materials at the nanoscale has opened up new opportunities to enhance device performance, energy efficiency, and functionality. In this context, the focus of this research is on exploring semiconductor nanotechnology and investigating plasmonic nanostructures in two-dimensional semiconductor materials. Additionally, the development of a reactive pulsed laser deposition technique is pursued to address the challenges and limitations associated with material synthesis and fabrication.

In our present epoch, the pervasive penetration of electronic materials into the fabric of everyday life is undeniable. Billions of individuals now seamlessly integrate these materials into their quotidian routines. From the intricate ecosystem of computing devices to the intricate web of communication tools, the very essence of these systems is founded upon a symphony of electronic materials. Materials like Si, SiC, GaAs, and their ilk reign supreme, owing to their idiosyncratic properties that pivot upon the orchestrated dance of electrons. Yet, the ceaseless quest for heightened reliability, steadfast dependability, and cost-effectiveness remains an ongoing narrative.

The bedrock of our emphasis on semiconductor nanotechnology finds its rationale in the distinct advantages it unfurls. At the nanoscale, materials exhibit distinct properties and behaviors compared to their bulk counterparts. Two-dimensional semiconductor materials, such as molybdenum disulfide (MoS_2), possess exceptional properties like high carrier mobility, direct bandgap, and mechanical flexibility. These properties make them highly attractive for a wide range of applications, including electronics, photonics, optoelectronics, and sensing [4], [5]. However, the optoelectronics, such as phototransistors based on MoS_2, have exhibited limited performance in terms of photoresponsivity. This limitation can be attributed to the inadequate light absorption properties of MoS_2, which significantly affects its ability to efficiently convert incident light into

electrical signals [6], [7]. Thus, there is a critical need to enhance the light absorption capabilities of MoS_2-based phototransistors in order to improve their overall performance and enable their practical applications in various fields.

The development of the reactive pulsed laser deposition technique is motivated by the need for a precise, efficient, and environmentally friendly method for synthesizing and fabricating sillicon carbide material. Conventional fabrication techniques, such as plasma-enhanced chemical vapor deposition or epitaxy growth, pose challenges in terms of their impact on existing devices on the wafer [8], [9]. These techniques involve subjecting the entire wafer to high temperatures and pressures, which can potentially affect the functionality of the already present devices. Additionally, after SiC synthesis, traditional approaches often require etching steps to shape the desired structure. However, this introduces a risk of damaging the existing devices on the wafer. As a result, alternative fabrication techniques are sought to overcome these limitations and enable the precise synthesis and shaping of SiC structures without compromising the integrity of the surrounding devices.

Moreover, metal-oxide-semiconductor field-effect transistors (MOSFETs) have served as the cornerstone of the semiconductor industry for a long time, encompassing a wide range of materials beyond silicon. These MOSFETs are integral components in modern microprocessors, memory chips, and telecommunication circuits, playing a pivotal role in driving advancements across various sectors. The performance improvements in MOSFETs are instrumental in fueling progress in fields such as electronics, telecommunications, and computing. With the semiconductor chip market boasting an annual volume of approximately 300 billion US dollars, digital integrated circuits (ICs) account for a substantial portion, representing around 70% of the overall market [10]–[12]. Today's digital ICs heavily rely on complementary metal-oxide-semiconductor (CMOS) structures, which incorporate both n-channel and p-channel transistors to facilitate efficient electron-dominated and hole-dominated transistor currents, respectively. As the dimensions of MOSFETs continue to shrink, the integration density and speed capabilities of CMOS ICs have experienced remarkable advancements over the past few decades.

To sustain this progress and push the boundaries of semiconductor technology, it is essential to

explore new materials beyond silicon and develop innovative synthesis methods. The semiconductor industry seeks to leverage the unique properties of alternative materials such as gallium nitride (GaN), indium phosphide (InP), and gallium arsenide (GaAs) to overcome the limitations of silicon and enhance device performance. However, the integration of these materials into practical devices requires the development of reliable and scalable synthesis techniques. New material synthesis methods, such as reactive pulsed laser deposition, present exciting opportunities for selective and controlled deposition of materials like SiC nanoparticles and films, opening doors to enhanced device functionalities and applications.

The exploration of new materials and the development of advanced synthesis methods are critical for sustaining the growth and innovation within the semiconductor industry. By expanding the range of materials and improving their synthesis techniques, researchers and engineers can continue to drive progress, enabling more powerful, energy-efficient, and versatile electronic devices that will shape the future of technology.

1.2 Unleashing the Power of Plasmonics: Exploring the Fundamentals

As highlighted in the preceding section, there exists a pressing requirement to amplify the light absorption capabilities of phototransistors or photodetectors based on low dimensional semiconductors. In response to this critical demand, recent advancements in the comprehension of plasmon-enhanced light-matter interactions at the nanometer scale offer a promising avenue for augmenting light absorption [13]. This emerging understanding provides a viable solution to address the aforementioned challenge, presenting significant opportunities for advancing the field of semiconductor-based optoelectronics. By harnessing the principles of plasmonics, novel approaches can be devised to enhance the efficiency of light absorption in low dimensional semiconductor devices, ushering in a new era of improved performance and functionality.

The profound insights into classical electrodynamics serve as the cornerstone for investigating the fundamental concepts of classical plasmonics. Within the realm of classical electrodynamics' validity, researchers can unlock the secrets of plasmonic excitations in a given system by employing Maxwell's equations, along with the relevant boundary conditions, and complementing them

with the characterization of the materials' local response. Within this context, we review the fundamentals of the prominent characteristics displayed by propagating surface plasmon polaritons residing at planar interfaces between dielectric and metal materials. Additionally, we delve into the realm of localized surface plasmons, with particular emphasis on metal particles.

1.2.1 Plasmonics in Metallic Nanostructures

Figure 1.1 provides valuable insights into the fundamental principles of plasmonics, the behavior of charges inside a metallic nanostructure under the influence of external electrostatic fields. In our research, the metallic nanostructures are made of gold, which can be seen as very good electric conductors. As very good electric conductors, they exhibit a distinct property wherein mobile conduction electrons redistribute themselves within the material to nullify the net electric field inside. Consequently, the application of an external field prompts the displacement of conduction electrons, leading to the accumulation of negatively charged mobile electrons on one side, while fixed positive ions reside on the other side, as demonstrated in Figure 1.1.

This charge separation engenders an internal electrostatic field effectively counterbalancing the

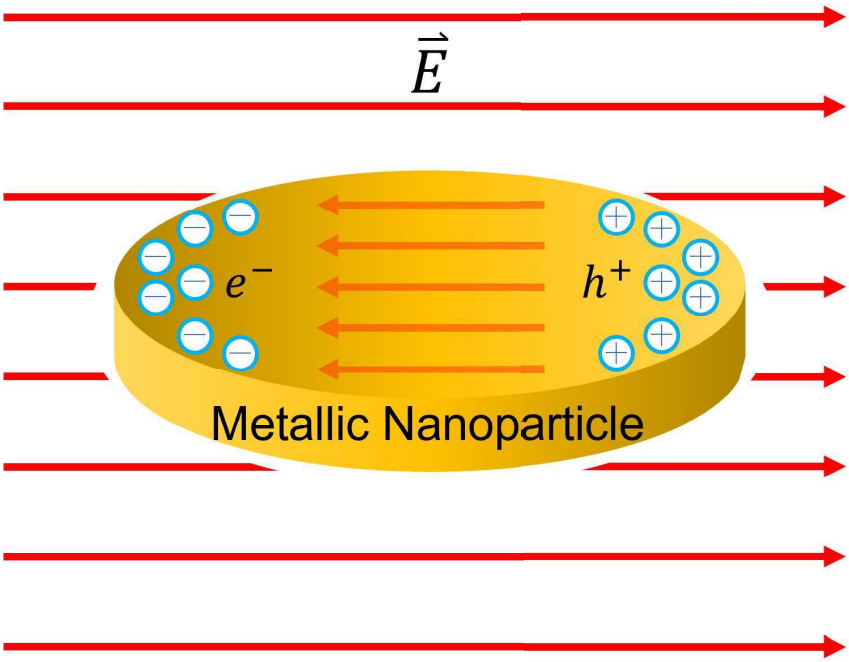

Figure 1.1 Electron and ion distribution within a metallic nanostructure under an applied external electric field.

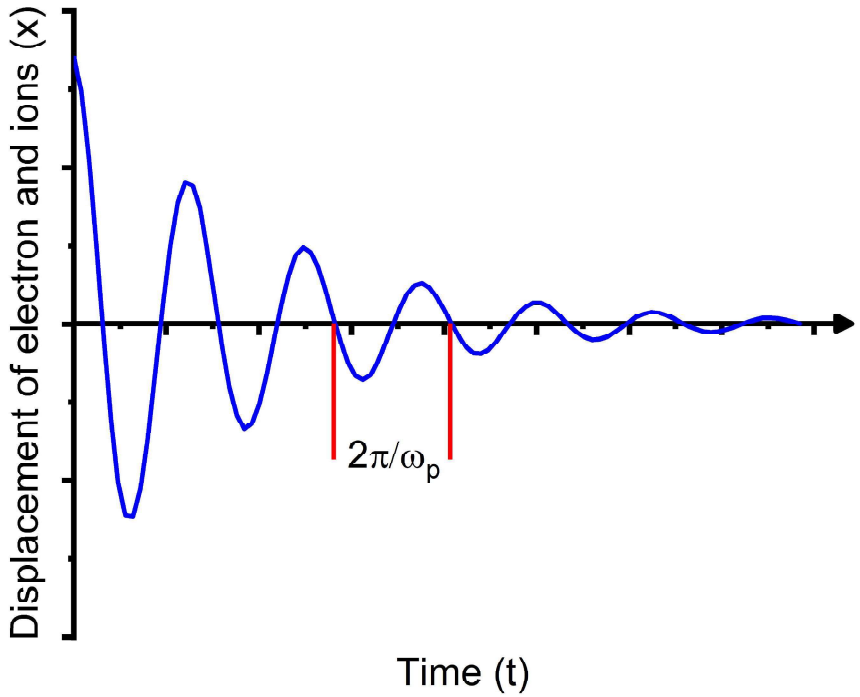

Figure 1.2 Temporal evolution of electron-ion displacement in metallic nanoparticles. The plot illustrates the displacement of electrons relative to ions as a function of time.

external field. Thus, the opposing internal field generated by the charge separation within the material cancels out the external field and the net electric field inside the nanostructure is zero. After the removal of the external electrostatic field, the system undergoes a response, where the charge separation still exists within the material, resulting in the internal electric field. However, the field within the nanostructure is no longer balanced at zero. As a consequence, the mobile electrons experience a restoring force that pulls them back towards the ion side. Here, the electrons do not immediately recombine with the ions. Instead, their inertia carries them to the opposite side of the ions. The oscillatory motion of the electrons around the ions is decaying over the time. As in Figure 1.2, the oscillation occurs at a characteristic frequency ω_p, with a period of $2\pi/\omega_p$. Over time, this oscillation decays due to ohmic losses until the electrons reunite with their ions, and the net field within the material returns to zero [14].

Two distinct types of oscillations exist within conductive nanostructures, namely bulk plasmons and surface plasmons. Bulk plasmons entail charge oscillations that propagate throughout the entire volume of the conductive material. On the other hand, surface plasmons exclusively occur at the

surface of the metallic material, with no influence on the sea of conducting electrons that can move around the immobile Au ions within the material's interior. This dissertation and the subsequent work primarily focus on the investigation of surface plasmons and their potential for inducing local electric field enhancements.

1.2.2 Frequency Domain Maxwell's Equations in Nanophotonics

Having established the general picture of the classical plasmon oscillation in a metallic nanostructure, we now possess the essential knowledge necessary to introduce the fundamental concepts of classical plasmonics. Within the realm of classical electrodynamics', the plasmonic excitations exhibited in a given system can be comprehensively determined by applying the Maxwell's equations, accompanied by the appropriate boundary conditions, and supplementing them with the characterization of the local response of the material. This integrated approach allows for a complete understanding of the plasmonic phenomena and their behavior in various systems.

To recapitulate the foundational knowledge, we begin with the macroscopic Maxwell's equations, which serve as a fundamental framework for describing classical electromagnetic systems [15]. These equations are as follows:

$$\nabla\cdot\mathbf{D}(\mathbf{r},t) = \rho_f(\mathbf{r},t) \qquad \text{Gauss' law,} \tag{1.1}$$

$$\nabla\cdot\mathbf{B}(\mathbf{r},t) = 0 \qquad \text{magnetic Gauss' law,} \tag{1.2}$$

$$\nabla\times\mathbf{E}(\mathbf{r},t) = -\frac{\partial}{\partial t}\mathbf{B}(\mathbf{r},t) \qquad \text{Faraday's law,} \tag{1.3}$$

$$\nabla\times\mathbf{H}(\mathbf{r},t) = \frac{\partial}{\partial t}\mathbf{D}(\mathbf{r},t) + \mathbf{J}_f(\mathbf{r},t) \qquad \text{Maxwell-Ampère's law,} \tag{1.4}$$

Within the defined three-dimensional vector space, $\mathbf{r} \equiv x\hat{\mathbf{x}} + y\hat{\mathbf{y}} + z\hat{\mathbf{z}}$. Here, $\mathbf{E}$ and $\mathbf{H}$ represent the fundamental components of electromagnetic fields, namely the electric and magnetic fields, respectively. Vector $\mathbf{D}$ denotes the electric displacement, while $\mathbf{B}$ represents the magnetic induction. The symbol $\mathbf{J}_f$ corresponds to the (free) current density, and ρ_f signifies the charge density. An important relationship is revealed by the continuity equation, which ensures charge conservation

and is expressed as:

$$\nabla \cdot \mathbf{J}_v(\mathbf{r}, t) + \frac{\partial}{\partial t}\rho_v(\mathbf{r}, t) = 0, \tag{1.5}$$

where the subscript v can pertain to free, induced, or external circumstances, respectively [15].

Assuming the fields to be monochromatic and harmonic in time, characterized by a decay factor of $e^{-i\omega t}$, the aforementioned equations can be conveniently reformulated in the frequency domain:

$$\nabla \cdot \mathbf{D}(\mathbf{r}, \omega) = \rho_f(\mathbf{r}, \omega), \tag{1.6}$$

$$\nabla \cdot \mathbf{H}(\mathbf{r}, \omega) = 0, \tag{1.7}$$

$$\nabla \times \mathbf{E}(\mathbf{r}, \omega) = i\omega \mathbf{B}(\mathbf{r}, \omega), \tag{1.8}$$

$$\nabla \times \mathbf{H}(\mathbf{r}, \omega) = -i\omega \mathbf{D}(\mathbf{r}, \omega) + \mathbf{J}_f(\mathbf{r}, \omega). \tag{1.9}$$

Simultaneously, the continuity equation can be simplified as:

$$\nabla \cdot \mathbf{J}_v(\mathbf{r}, \omega) - i\omega\rho_v(\mathbf{r}, \omega) = 0. \tag{1.10}$$

The free current density, $\mathbf{J}_f$, comprises contributions from both the induced current density, represented by $\mathbf{J}_{ind}$, and the external current density, denoted as $\mathbf{J}_{ext}$. These two components collectively determine the overall behavior of the free current within the system. The induced current density arises as a response to the electric field present within the medium, while the external current density represents any additional current sources that exist in the system. Consequently, the total free current density can be expressed as the sum of the induced current density and the external current density. Similarly, the free charge density, ρ_f, can be written as the sum of the induced charge density, ρ_{ind}, and the external charge density, ρ_{ext}.

In the realm of understanding electromagnetic interactions within materials, it is recognized that both the conductivity and the dielectric function offer distinct but complementary perspectives. These two approaches serve as alternative means of describing the same physical properties [16]. In various textbooks and literature, it is often observed that when considering both the electric displacement $\mathbf{D}$ and the induced current density $\mathbf{J}_{int}$ simultaneously, the former is utilized to quantify

the response originating from bound polarization charges, expressed through the parameter $\epsilon \equiv \epsilon_\infty$, given the relationship $\mathbf{D} = \epsilon_0 \epsilon \mathbf{E}$. On the other hand, the contribution arising from free carriers is typically described by $\mathbf{J}_{ind}$ via the conductivity term σ, as represented by $\mathbf{J} = \sigma \mathbf{E}$. In the case of insulators, the induced current density is inherently zero. However, for metals, it accounts for the involvement of conduction electrons or holes, while the electric displacement serves to characterize the background polarization attributed to core electrons. It is observed that segregating a material's response into two distinct components, namely $\mathbf{D}$ and $\mathbf{J}_{ind}$, can present tedious in certain scenarios. Consequently, in the realm of nanophotonics, where nanoscale phenomena are of interest, it is more advantageous to combine the effects of bound polarization and free charges into a unified total dielectric function, resulting in a comprehensive representation of the material's electromagnetic response:

$$\epsilon = \epsilon_\infty + \frac{i\sigma}{\omega \epsilon_0}. \tag{1.11}$$

By employing the relationship in equation 1.11, one can effectively substitute $\mathbf{D}$ with $\mathbf{D} + i\omega^{-1}\mathbf{J}_{ind}$, thereby yielding a modified displacement vector. As a result, the Maxwell's equations presented in equations 1.6 - 1.9 can be reformulated as follows:

$$\nabla \cdot \mathbf{D}(\mathbf{r}, \omega) = \rho_{ext}(\mathbf{r}, \omega), \tag{1.12}$$

$$\nabla \cdot \mathbf{H}(\mathbf{r}, \omega) = 0, \tag{1.13}$$

$$\nabla \times \mathbf{E}(\mathbf{r}, \omega) = i\omega \mathbf{B}(\mathbf{r}, \omega), \tag{1.14}$$

$$\nabla \times \mathbf{H}(\mathbf{r}, \omega) = -i\omega \mathbf{D}(\mathbf{r}, \omega) + \mathbf{J}_{ext}(\mathbf{r}, \omega). \tag{1.15}$$

Thus, the revised formulation consolidates the representation of all free conduction carriers and currents within the modified displacement vector, $\mathbf{D}$. In contrast, the scalar quantities ρ_{ext} and $\mathbf{J}_{ext}$ serve the purpose of delineating external charges and currents, respectively. Importantly, the equation highlights that when excluding external charges and currents, one only needs to consider the term $\mathbf{D}$ and the total dielectric function ϵ. By adopting this unified approach, the comprehensive framework encompasses both the response of the induced background polarization and the induced current arising from free carriers.

1.2.3 Interface Between Metal and Dielectric

Here, we present a comprehensive overview of the distinctive characteristics exhibited by propagating surface plasmon polaritons, which are sustained at planar interfaces between dielectric and metal materials as in Figure 1.3. This setting closely resembles the experimental conditions employed, enabling us to effectively simulate and analyze the intricate dynamics associated at the top surface of the nanostructure.

Consider the scenario depicted in Figure 1.3, where we examine a simple planar interface that separates two distinct media. Specifically, the region where $z > 0$ represents a dielectric medium characterized by its dielectric constant, denoted as ϵ_{d} (assumed to be frequency-independent for simplicity). Conversely, the region where $z < 0$ corresponds to the metallic component, whose dielectric function $\epsilon_{\mathrm{m}}(\omega)$ exhibits a dependence on frequency. To simplify our analysis, we assume that the media are uniform along the y axis. Our focus lies on investigating solutions for p-polarized (parallel) waves or transverse magnetic (TM) waves.

It is important to note that traditional dielectric-metal interfaces have been shown to support surface plasmon polaritons primarily for p-polarization, as indicated by previous studies [17], [18]. However, recent investigations have revealed that in the case of doped graphene, a two-dimensional material, both p- and s-polarized (perpendicular) surface waves can exist [17]. Nevertheless, it is

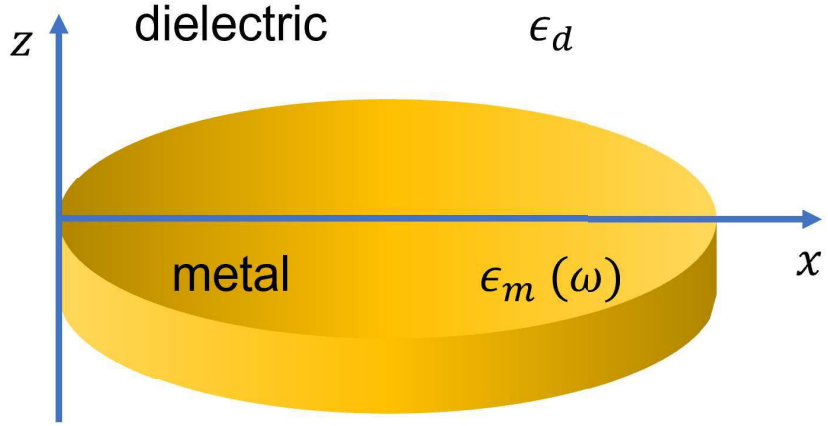

Figure 1.3 Schematic depiction of a planar interface between a dielectric medium and a metal at $z = 0$ plane. The dielectric constant, ϵ_{d}, is used to characterize the the dielectric medium, where we ignore the frequency dependence for simplicity. The frequency dependent dielectric function, $\epsilon_{\mathrm{m}}(\omega)$ is used to describe the electromagnetic perperties within the conductor.

noteworthy that s-polarized waves exhibit weaker confinement effects and are generally of lesser significance compared to the profound field confinement observed in p-polarized surface waves. In our analysis, we specifically focus on the propagation of p-polarized waves along the x-axis direction, which decay exponentially along the z-axis. To account for time dependence, we assume a harmonic decay factor of $e^{-i\omega t}$. Consequently, the decay of the wave in the dielectric medium can be expressed as follows [19]:

$$\mathbf{E}_d(\mathbf{r}) = [E_{x,d}\hat{\mathbf{x}} + E_{z,d}\hat{\mathbf{z}}]e^{iqx}e^{k_d z}, \tag{1.16}$$

$$\mathbf{H}_d(\mathbf{r}) = H_{y,d}e^{iqx}e^{k_d z}\hat{\mathbf{y}}. \tag{1.17}$$

Similarly, the decay in the metallic region can be described by:

$$\mathbf{E}_m(\mathbf{r}) = [E_{x,m}\hat{\mathbf{x}} + E_{z,m}\hat{\mathbf{z}}]e^{iqx}e^{k_m z}, \tag{1.18}$$

$$\mathbf{H}_m(\mathbf{r}) = H_{y,m}e^{iqx}e^{k_m z}\hat{\mathbf{y}}. \tag{1.19}$$

In the above equations, the parameter q represents the wavevector or the propagation constant of the surface plasmon polaritons. Additionally, k_m and k_d characterize the decay of the electromagnetic fields in the perpendicular direction, influencing the vertical field confinement.

To establish the relationships among the various field components within each medium, we can insert the derived expressions in equations 1.16 - 1.19 into the corresponding Maxwell's equations, 1.12 - 1.15. This process leads us to the following relations:

$$H_{y,j} = -\frac{\omega}{q}\epsilon_0\epsilon_j E_{z,j}, \tag{1.20}$$

$$H_{y,j} = -s_j i\frac{\omega}{k_j}\epsilon_0\epsilon_j E_{x,j}, \tag{1.21}$$

$$E_{z,j} = s_j i\frac{q}{k_j}E_{x,j}. \tag{1.22}$$

Here, the subscript j represents either the dielectric (d) or the metal (m) medium. It is noteworthy that ϵ_0 denotes the permittivity of vacuum, $c = 1/\sqrt{\epsilon_0\mu_0}$ signifies the speed of light in free space, and μ_0 represents the magnetic permeability of vacuum. Additionally, the quantity s_j is defined

using Kronecker delta functions as $s_j = \delta_{jd} - \delta_{jm}$. Furthermore, we can derive the decay factor for the field along the perpendicular direction as follows:

$$k_j{}^2 = q^2 + (\omega/c)^2 \epsilon_j. \tag{1.23}$$

Considering the continuity and tangential component of boundary conditions, which are well-established in the literature for the two-dimensional version [15], [20]–[22], we have the following expressions:

$$\hat{\mathbf{n}} \times (E_2 - E_1) = 0, \tag{1.24}$$

$$\hat{\mathbf{n}} \times (H_2 - H_1) = \mathbf{K}, \tag{1.25}$$

In this context, the subscripts 1 and 2 correspond to the two adjacent mediums separated by the interface. The unit vector $\hat{\mathbf{n}}$ points normal to the interface, and K is a quantity derived from the two-dimensional continuity equation.

Now, the next step involves ensuring the consistency of the electromagnetic fields on both sides of the interface by satisfying the boundary conditions as in equations 1.24 and 1.25. These conditions express the continuity of the tangential components of the electromagnetic field across the interface, and they lead us to the following results:

$$E_{x,d} - E_{x,m} = 0, \tag{1.26}$$

$$H_{y,d} - H_{y,m} = 0. \tag{1.27}$$

Upon substituting equations 1.20 - 1.22 into the aforementioned conditions, an implication emerges for the dispersion relation of surface plasmon polaritons [17], [18]:

$$\frac{\epsilon_d}{k_d} + \frac{\epsilon_m}{k_m} = 0. \tag{1.28}$$

This equation holds as an implicit condition, driven by the explicit dependence of $k_{d,m}$ on both the frequency ω and the parallel wavevector q, symbolized by $k_{d,m} \equiv k_{d,m}(q, \omega)$. Additionally, it is important to note that the dielectric function for metals or metallic nanostructures in experimental settings is frequency-dependent, represented as $\epsilon_m \equiv \epsilon_m(\omega)$.

Based on these fundamental relations and conditions, a crucial requirement for the presence of surface plasmon polaritons is that the real part of the wavevector, Re $k_{d,m}$, must be greater than zero (Re $k_{d,m} > 0$). This condition ensures that the electromagnetic wave decays along the direction perpendicular to the medium interface. Consequently, it necessitates that the dielectric functions of the two mediums, ϵ_d and ϵ_m, possess opposite signs. Typically, insulators have a positive sign for their dielectric function (Re $\epsilon_d \equiv$ Re $\epsilon_d > 0$), indicating that the dielectric function for the other half-space must be negative (Re $\epsilon_m < 0$). These conditions are essential for the existence of SPPs and are particularly relevant in scenarios involving metallic mediums under frequencies ranging below the visible/near-infrared [17], [18].

Finally, the relationship between the wavevector of surface plasmon polaritons (SPPs) and their corresponding frequency can be established by using the alternative form of equation 1.23 [17], [23], [24]. This allows us to express the SPPs' wavevector as follows:

$$q_{spp} = \frac{\omega}{c}\sqrt{\frac{\epsilon_d \epsilon_m}{\epsilon_d + \epsilon_m}}. \tag{1.29}$$

In this expression, q_{spp} represents the wavevector of the SPPs, which is intimately linked to its frequency. The equation demonstrates the dependency of the SPPs' wavevector on the permittivity of the dielectric medium (ϵ_d) and the permittivity of the metallic medium (ϵ_m). As the frequency ω is varied, the corresponding wavevector q_{spp} is determined by the intricate interplay between the dielectric and metallic properties.

1.3 Two-Dimensional (2D) Materials: Properties and Applications

Two-dimensional (2D) materials have garnered significant attention in the field of materials science and condensed matter physics due to their unique and fascinating properties in the past decade. These materials are composed of a single or few layers of atoms, creating an ultrathin structure with intriguing electronic, mechanical, and optical characteristics. Graphene, a single layer of carbon atoms arranged in a honeycomb lattice, is the prototypical 2D material and has been extensively studied since its discovery in 2004 [25]–[28]. However, beyond graphene, a diverse family of 2D materials with varying chemical compositions and structures has emerged,

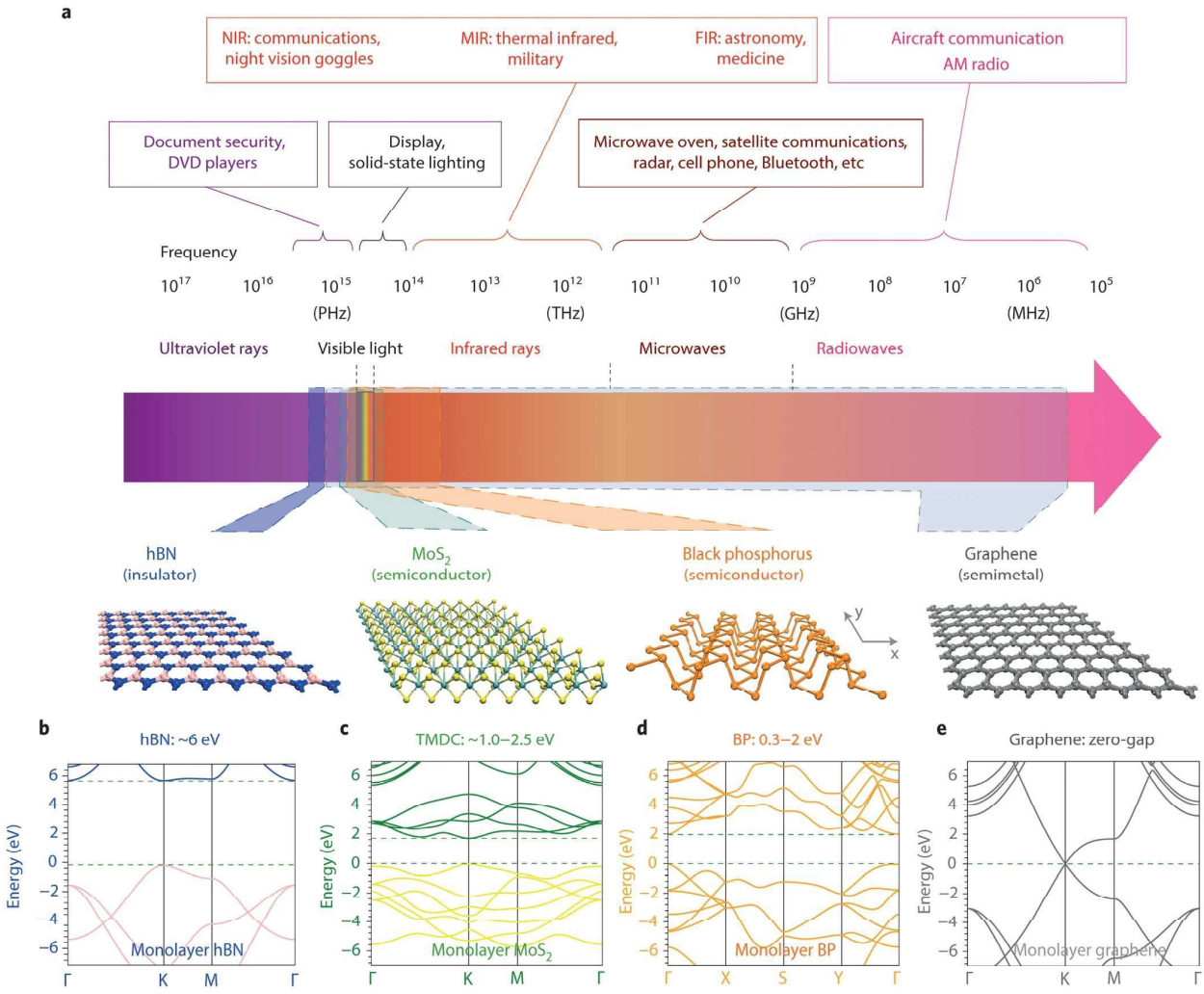

Figure 1.4 Illustration of the electromagnetic spectrum and highlights of the applications that leverage distinct spectral ranges. The atomic structures of four 2D materials, namely hexagonal boron nitride (hBN), molybdenum disulfide (MoS_2), black phosphorus (BP), and graphene, are displayed in the bottom part of the panel from left to right [29].

each possessing distinct properties and potential applications. Recent experimental investigations have provided compelling evidence that a wide range of 2D materials exhibit a rich spectrum of electronic properties. These materials encompass diverse characteristics, spanning from insulating hexagonal boron nitride to semiconducting transition metal dichalcogenides like MoS_2 and black phosphorus (BP), and even extending to the semimetallic nature of graphene, as visually represented in Figure 1.4 [29].

Within this section, we aim to provide a concise overview of some of the most prominent 2D semiconductors, elucidating their electronic and optoelectronic characteristics.

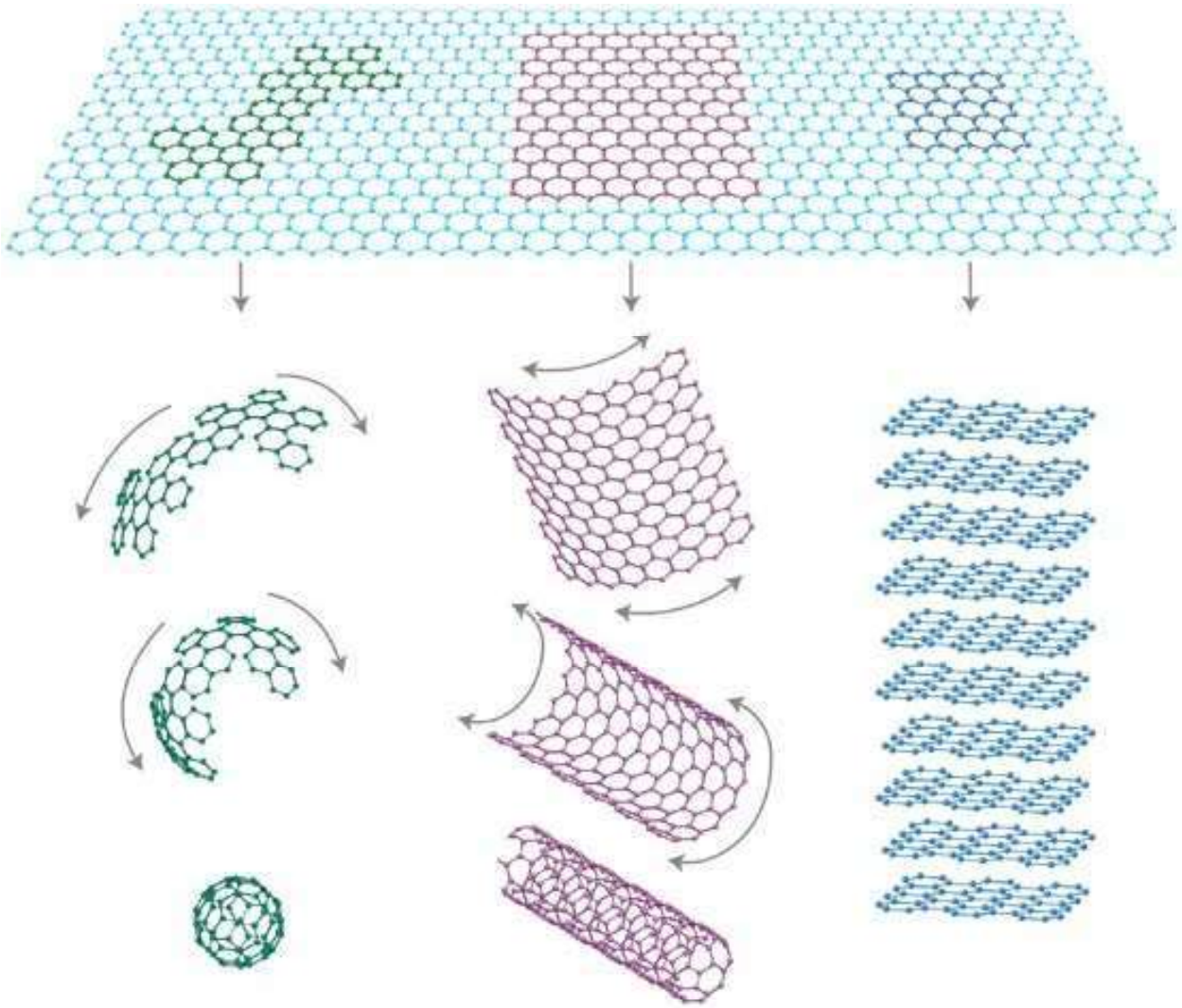

Figure 1.5 Graphene, a foundational 2D carbon material, serves as the building block for carbon structures across all dimensionalities. It manifests as 0D buckyballs when wrapped up, transforms into 1D nanotubes upon rolling, and assembles into 3D graphite when stacked. [30].

1.3.1 Graphene

The atomic arrangement in 2D materials plays a pivotal role in dictating their unique properties. As a consequence of confinement along the vertical direction, electrons within these materials experience quantum confinement effects, leading to exceptional electronic characteristics, such as high electron mobility. Furthermore, the absence of dangling bonds on the surface of 2D materials renders them remarkably stable, even under ambient conditions. Graphene, an iconic member of the emerging class of 2D materials (Figure 1.5), exhibits a distinctive electronic structure characterized by a linear energy dispersion relation near the Fermi level, giving rise to massless Dirac fermions

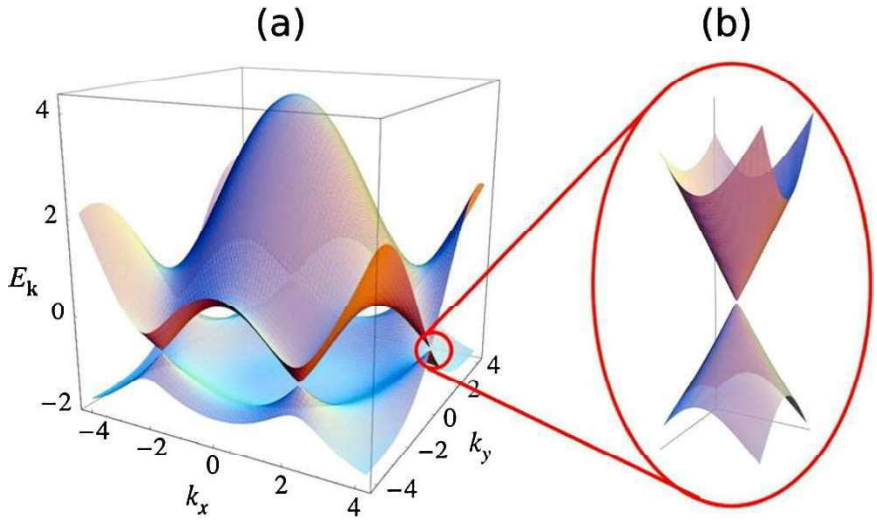

Figure 1.6 The energy band structure of graphene is depicted in panel (a), illustrating the unique arrangement of energy bands resulting from the two-dimensional hexagonal lattice of carbon atoms. Notably, graphene exhibits a linear energy dispersion around the Fermi energy, as shown in panel (b). This linear dispersion is represented by the Dirac cone at the high-symmetry points K and K' in the Brillouin zone, indicative of the massless Dirac fermions behavior of charge carriers in graphene. [33], [34].

[31]. These Dirac fermions bestow graphene with extraordinary electronic properties, including high electron mobility and remarkably high thermal conductivity [30]. However, the lack of a bandgap in pristine graphene's electronic structure presents both opportunities and challenges in electronic applications.

Graphene possesses a honeycomb lattice structure, comprising a single layer of carbon atoms arranged in a two-dimensional hexagonal lattice, resembling a flat sheet. Each carbon atom forms sp^2 hybridized carbon-carbon bonds with three neighboring carbon atoms [32]. Additionally, within the lattice, each carbon atom exhibits one unhybridized p-orbital that lies perpendicular to the plane of the sheet. These delocalized π-electrons facilitate π-bonding interactions between adjacent carbon atoms, resulting in a continuous system of conjugated electrons spanning the entire graphene sheet. As a consequence, graphene showcases a linear energy dispersion relation near the Fermi level [33].

The band structure of graphene stands as a fundamental aspect governing its electronic properties, playing a decisive role in defining its unique behavior. At the high-symmetry points K and K' within the Brillouin zone, situated at the corners of the hexagonal lattice, the valence and con-

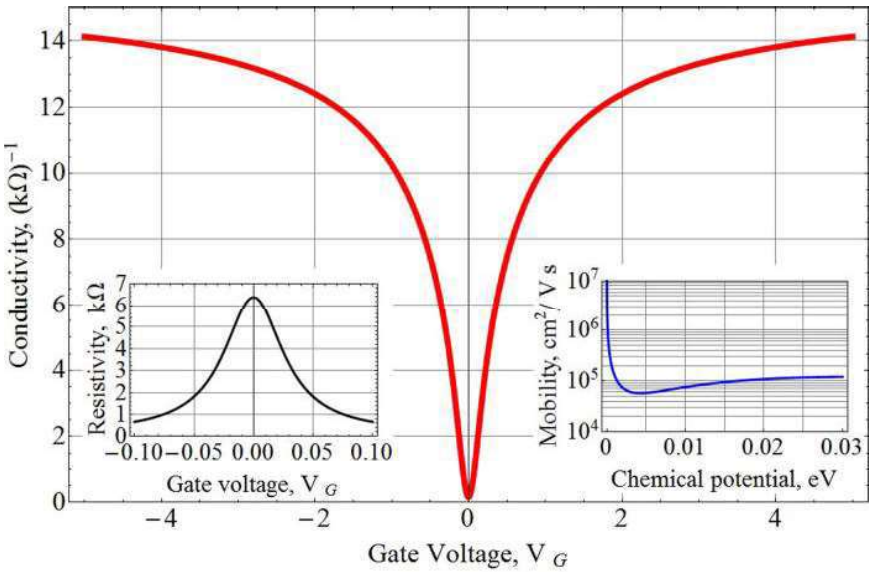

Figure 1.7 Graphene conductivity (G) as a function of gate voltage at a temperature of T = 300 K, showcasing the variation of conductivity with the applied gate voltage [39].

duction bands intersect tangentially, giving rise to a conical energy dispersion widely recognized as the Dirac cone, illustrated in Figure 1.6 [33], [34]. This linear dispersion relation serves as a characteristic hallmark of the relativistic-like conduct of charge carriers in graphene, with the charge carriers being described as massless Dirac fermions [30].

The energy dispersion relation for charge carriers in graphene can be described by the Dirac relativistic equation, which captures the linear relationship between energy (E_{2D}) and wave vector (k). Near the Fermi level, the energy of charge carriers in graphene can be approximated as $E_{2D} = \hbar v_F k$, where $\hbar$ is the reduced Planck's constant and v_F is the Fermi velocity [35]. The Fermi velocity in graphene is approximately 10^6 m/s, resulting in high charge carrier mobility and electrical conductivity.

Graphene-based devices demonstrate remarkable carrier concentrations as well, surpassing 10^{13} cm^{-2}. The room temperature mobility achieved through mechanical exfoliation can exceed 10,000 cm^2/Vs, and at low temperature conditions, it can reach an impressive 200,000 cm^2/Vs [36], [37]. Comparatively, the common material for electronics, Si, reports a room temperature mobility of 1,400 cm^2/Vs [38].

Figure 1.7 presents the measured conductivity of graphene flakes, showcasing an increase in

conductivity on both sides of the applied gate voltage [39]. Moreover, an inverse relationship can be observed for the sheet resistivity, reaching its maximum at 0 V gate voltage. Additionally, the remarkable phenomenon of the 'magic' angle (Figure 1.8) emerges in bilayer graphene at approximately 1.1° [40]. This unique configuration leads to the formation of flat bands near the Fermi energy in the electronic band structure, resulting in intriguing correlated insulating states when the material is at half-filling. Remarkably, electrostatic doping of the material away from these correlated insulating states leads to the observation of tunable zero-resistance states. These zero-resistance states exhibit a critical temperature of up to 1.7 kelvin, representing a captivating avenue for potential applications and further exploration in graphene research.

Despite its extraordinary and promising properties, graphene is not ideal for electronic transistor applications due to its inherent zero band gap structure. This characteristic results in graphene transistors typically having an on-off ratio lower than 10 at room temperature, limiting their practical utility [41]. Consequently, this has motivated further research into exploring different 2D semiconductor materials that may hold the potential for future development in electronic applications. Understanding these mechanisms becomes challenging without delving into the specifics of graphene, as it forms the foundation for comprehending the intricacies underlying other 2D semiconductor materials.

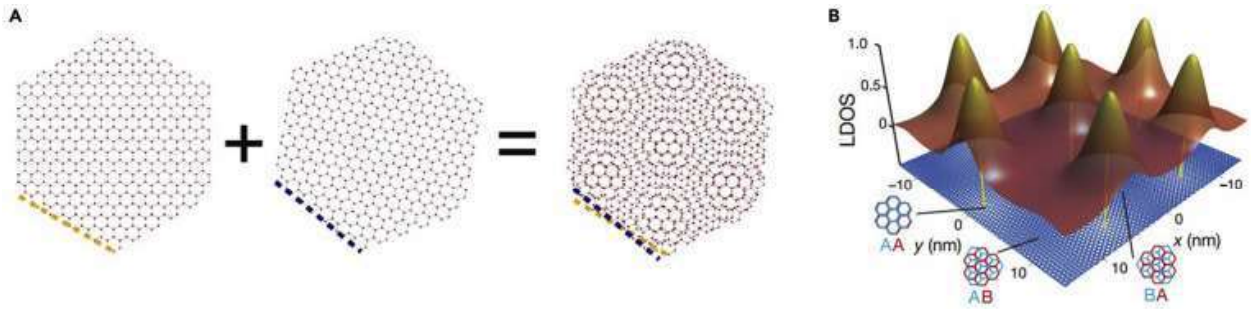

Figure 1.8 Moiré pattern formation depicted through a schematic illustration, arising from the twist angle between the two layers. The normalized local density of states (LDOS) is computed for the flat bands with energy greater than zero at a twist angle of $\theta = 1.08°$ [1], [2].

1.3.2 Molybdenum Disulfide (MoS_2)

Another novel 2D semiconductor material that garnered significant attention shortly after graphene's discovery [42] is Molybdenum disulfide (MoS_2). As one of the most typical 2D transition metal dichalcogenides (TMDCs), MoS_2 possesses a larger bandgap, rendering it distinctive in its electronic properties. MoS_2 has recently emerged as a subject of worldwide interest in various fields, including photodetectors, biosensors, field-effect transistors, and batteries [43]–[46]. Like graphene, the advantages of MoS_2, and other TMDCs, stem from their high surface-to-volume ratio and extraordinary electric, mechanical, chemical, optical, and magnetic behaviors, making them promising candidates for diverse applications and innovative research endeavors.

Similarly to graphene, MoS_2 can be mechanically exfoliated from bulk materials [48]. Recent research has also introduced rapid synthesis and characterization methods, including the micromechanical cleavage technique [49]. With a direct bandgap of approximately 1.8 eV in monolayer MoS_2, the material showcases its potential for electronic devices with significant on/off ratio and

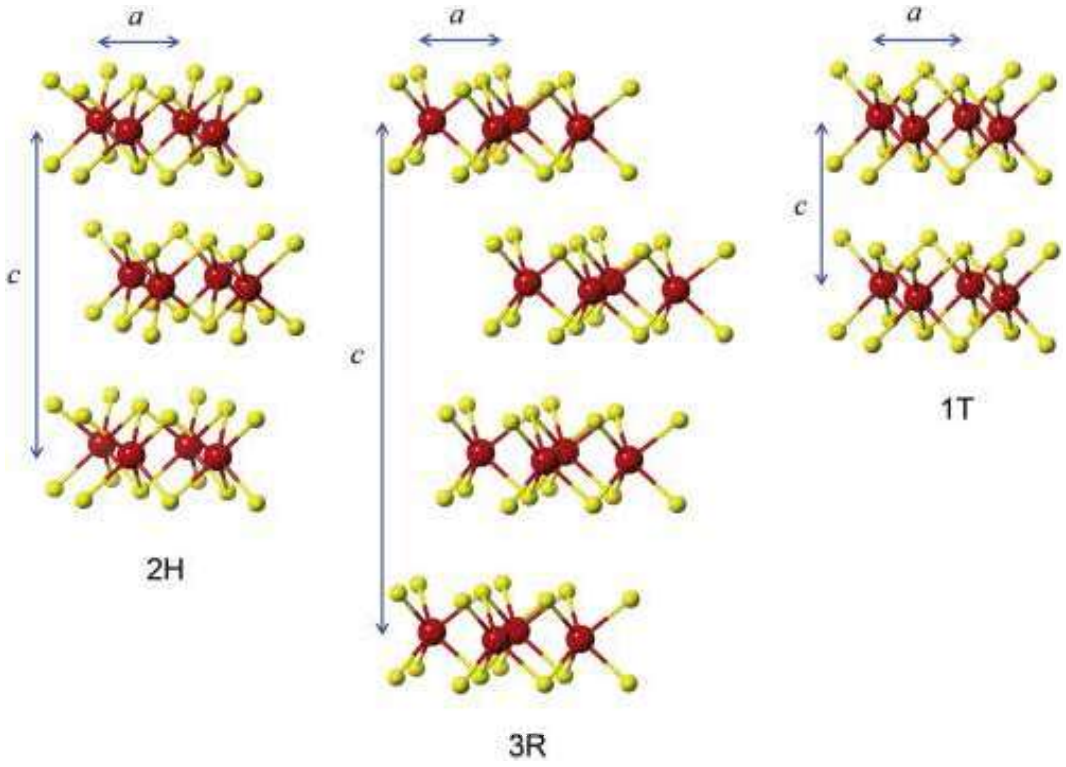

Figure 1.9 Crystal structures of MoS_2, illustrating the 2H, 3R, and 1T phase. In the representation, Mo atoms are denoted in red, while S atoms are shown in yellow. [47].

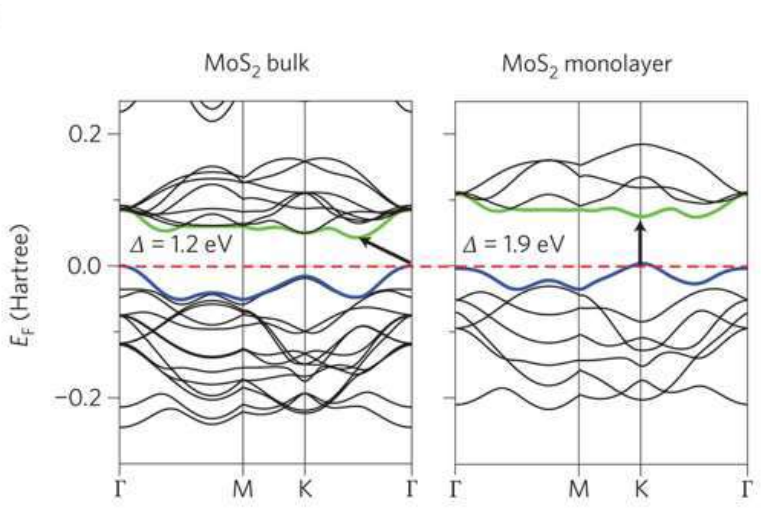

Figure 1.10 Band structures of bulk and monolayer MoS_2 computed using the first principles density functional theory [3].

logic operations [50]. Notably, the electron mobility in a 0.65 nm thick MoS_2 layer rivals that of a 2 nm thick Si sheet [51]. Considering that fabricating Si material at such thickness is not feasible, MoS_2-based chips hold the promise of achieving much smaller dimensions than state-of-the-art Si chips, ushering in a new era of compact and efficient electronic devices.

The atomic stacking configuration of MoS_2 manifests in three distinct polymorphs: 2H, 1T, and 3R, as depicted in Figure 1.9 [47]. Each polymorph corresponds to unique physical properties. In its bulk form, MoS_2 thermodynamically favors the 2H phase, characterized by a hexagonal stacking arrangement of S-Mo-S. On the other hand, the 1T metastable phase is not naturally occurring, but it can be obtained from the 2H bulk material through chemical or electrochemical exfoliation [47]. Notably, the 1T phase consists of only one layer per unit cell, with Mo atoms arranged in an octahedral symmetric configuration.

Comparing to the linear disperation band structure near the K point in graphene, the first density function theory (DFT) shows the bulk MoS_2 bandgap transition at Γ-potin is indirect (1.2 eV) and shifting to direct (1.8 eV) while decreasing the number of layers as shown in Figure 1.10 [3].

In the context of a field-effect transistor (FET), MoS_2 emerges as the channel material that connects the source and drain electrodes [52]. By incorporating a dielectric layer, the transistor can be equipped with either a top or a bottom gate. For the ideal logic transistor, specific properties

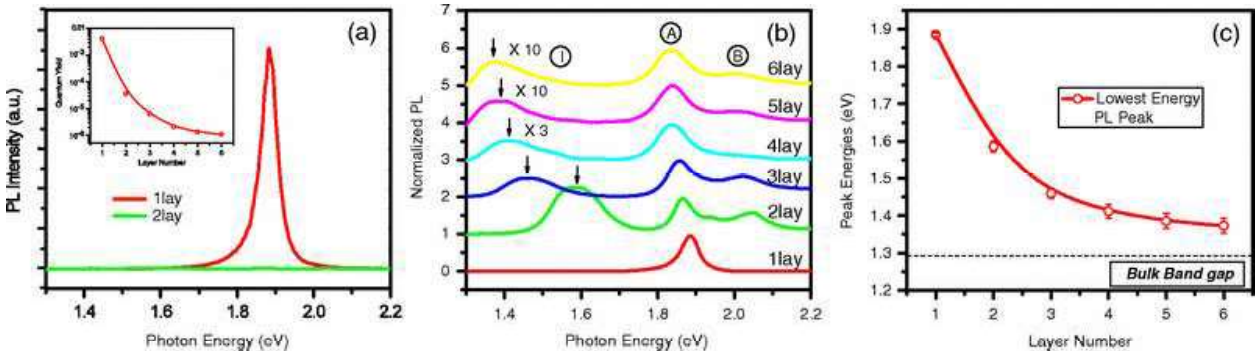

Figure 1.11 (a) Photoluminescence spectra of MoS_2 samples under continuous-wave laser excitation at 532 nm. The inset provides an overview of the photoluminescence quantum yield for different numbers of layers. (b) Distinct photoluminescence spectra obtained from various layers of MoS_2. (c) Bandgap energy of MoS_2 as a function of the number of layers [54].

are sought, such as high carrier mobility, efficient switching, improved conductivity, and minimal off-state leakage current [52]. Fortunately, MoS_2 fulfills these prerequisites due to its tunable bandgap while maintaining a high carrier mobility. Studies report that by adopting a back-gate configuration, the electron mobility in MoS_2 can be achieved within a range, from 0.1 cm^2/Vs to 10 cm^2/Vs [52]. Additionally, with a top-gate n-type conduction MoS_2 transistor, the mobility reaches an impressive value exceeding 200 cm^2/Vs at room temperature, characterized by an on/off ratio up to 10^8 and a subthreshold swing of 74 mV/dec [53].

In addition to its remarkable electrical properties, MoS_2 also presents highly intriguing optical characteristics, including photo absorption, photoluminescence, and photoconductivity on mono and few-layers [54]. During the photoluminescence experiment, continuous-wave solid-state laser excitation at a wavelength of 532 nm was employed to stimulate the material. A distinct trend of decreasing quantum yield with increasing thickness can be observed, as depicted in Figure 1.11 [54]. Notably, in bulk MoS_2, the quantum yield is negligible, akin to other indirect bandgap materials.

The availability of MoS_2 for photodetection and photovoltaic applications has been a focal point of interest, particularly in this thesis [55]. Few-layer MoS_2, whether obtained through exfoliation or chemical vapor deposition (CVD) growth, serves as the photoactive layer on desired substrates. To fabricate metal contacts, physical vapor deposition techniques can be employed. The performance

of MoS_2-based solar devices exhibits a correlation with its thickness, with superior performance observed for solar cells featuring thicker MoS_2 films. This is attributed to the enhanced photon absorption capability in the thicker MoS_2 film, a crucial factor contributing to the improved efficiency of the solar cell [55].

In the subsequent sections of this dissertation, a novel approach will be unveiled, aimed at enhancing the photo response in mono/few-layered MoS_2-based devices. This groundbreaking method introduces a promising pathway to further enhance the quantum yield. By exploring innovative strategies, this research seeks to optimize the optical properties of MoS_2 and unlock its full potential in photodetection and related optoelectronic applications.

1.4 Pulsed Laser Deposition: Principles and Applications

Pulsed laser deposition (PLD) is a remarkably versatile technique for the synthesis and deposition of a wide array of materials, encompassing a vast domain of fascinating phenomena that still remain not fully elucidated [56]. This section presents a comprehensive review, delving into the physico-chemical intricacies underlying the PLD process. The evolution of materials, from laser ablation to the formation of deposited films, takes center stage, with particular emphasis on the intricate interplay between laser and target materials. The exploration covers the dynamic journey of the target material transitioning into the gas phase upon laser impact, the intricate process of laser-induced material ejection, and the final condensation process, culminating in the transformation of material from the gas phase to its solid-state counterpart. A profound understanding of these fundamental aspects of traditional PLD is of paramount importance, laying the foundation for the subsequent development and elucidation of the novel reactive PLD technique for SiC, as expounded upon later in this dissertation.

1.4.1 Pulsed Laser Ablation: Understanding Material Transformations

PLD is a well-established technique that involves the utilization of laser to "ablate" or remove material from a solid target [57]. During its investigative phase, pulsed laser ablation (PLA) witnessed multifaceted advancements driven by the development of reliable and high-intensity lasers, such as nanosecond pulsed Nd-YAG and excimer lasers, as well as intense pico- or femtosecond

lasers. These versatile lasers, along with PLA methods, found extensive application not only in thin film deposition but also in micro-structuring, surface cleaning, and local annealing [58], [59]. A significant breakthrough in the understanding of PLA emerged when it was revealed that intact molecules, including large biomolecules, could be ejected into the gas phase, paving the way for the development of analytical techniques like matrix-assisted laser desorption/ionization (MALDI), widely applied in fields such as life science [60].

Figure 1.12 illustrates the dynamic process of pulsed laser ablation (PLA), where the rapid heating induced by the laser initiates significant volume changes in the material, leading to various phase transitions. Regions experiencing higher temperatures undergo boiling and vaporization, transitioning into the gas phase and leaving the substrate. On the other hand, regions with lower temperatures undergo a phase transition from solid to liquid but remain on the substrate. Within a picosecond timescale, material ejection commences, propelled by the laser-induced effects. The ejected material subsequently encounters the later part of the laser pulse, absorbing its energy and leading to an attenuation of the laser power striking the substrate [56]. This process induces the excitation and ionization of species within the ejected plume, giving rise to the formation of plasma. Upon the cessation of the laser pulse, the material within the laser-affected area begins to cool down

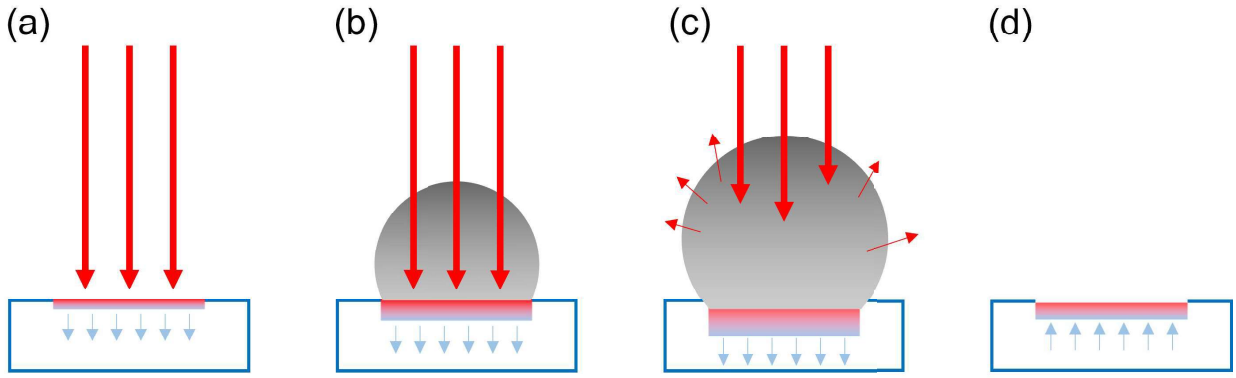

Figure 1.12 Illustration depicting the mechanisms involved during PLA events. (a) Initially, laser energy is absorbed, leading to surface material melting and vaporization, as indicated by the shaded areas representing the solid-liquid phase transition. (b) The melting front progresses deeper into the material, generating a laser-induced plume consisting of vaporized material. (c) The incident laser power is absorbed by the plume, resulting in plasma formation that attenuates the incident laser energy. (d) Following laser removal, the melting front recedes, and the material resolidifies.

and resolidify. Meanwhile, the laser-induced plume, carrying various species, including neutral and charged material, continues to expand and departs from the substrate.

1.4.2 Pulsed Laser Deposition

Pulsed laser deposition (PLD) and pulsed laser ablation share a common underlying concept, both employing laser-induced plumes to facilitate thin film deposition. As depicted in Figure 1.13, a pulsed laser is directed towards a target material positioned within a vacuum chamber, serving as the source for ablation and subsequent thin film generation [61]. PLD experiments utilize a diverse range of lasers, including UV (KrF, 248 nm), visible, near-infrared (Nd-YAG, 532/1064 nm), or mid-infrared (CO_2, 10.6 μm) lasers [62]–[64]. The laser beam passes through a transparent window into the vacuum chamber, with window materials selected to be laser-transmissive, such as quartz for UV light. Operating within a tightly controlled vacuum environment, typically at pressures below 10^{-6} Torr, the laser interacts with the target material, initiating ablation and giving rise to an ejected plume. This plume consists of plasma and neutral material that expands outward (normal to the target) from the target volume [65]. During the plume expansion, the internal heat and ionization energies within the plume are converted into kinetic energy, striking the substrate of interest [66]. Subsequently, the plume condenses and deposits onto the substrate, resulting in thin films with tailored properties.

The quality of film growth is influenced by various critical factors. In addition to the vacuum level, types of background gases, and the excitation wavelength/intensity, the substrate temperature (T_{sub}) and the absolute/relative kinetic energies of species within the plume play pivotal roles in the process [58], [67]. These parameters collectively impact the thin film deposition, making them essential considerations for achieving desired film properties and functionalities.

Upon considering the laser-target interactions, it is evident that a dense vapor layer forms in front of the target following laser striking, as previously discussed. Similar to the pulsed laser ablation (PLA) process, these vaporized species efficiently absorb the energy from subsequent laser pulses, leading to a substantial boost in temperature and pressure within the plume, ultimately resulting in ionization [66]. The significant pressure build-up causes the plume to rapidly expand away from

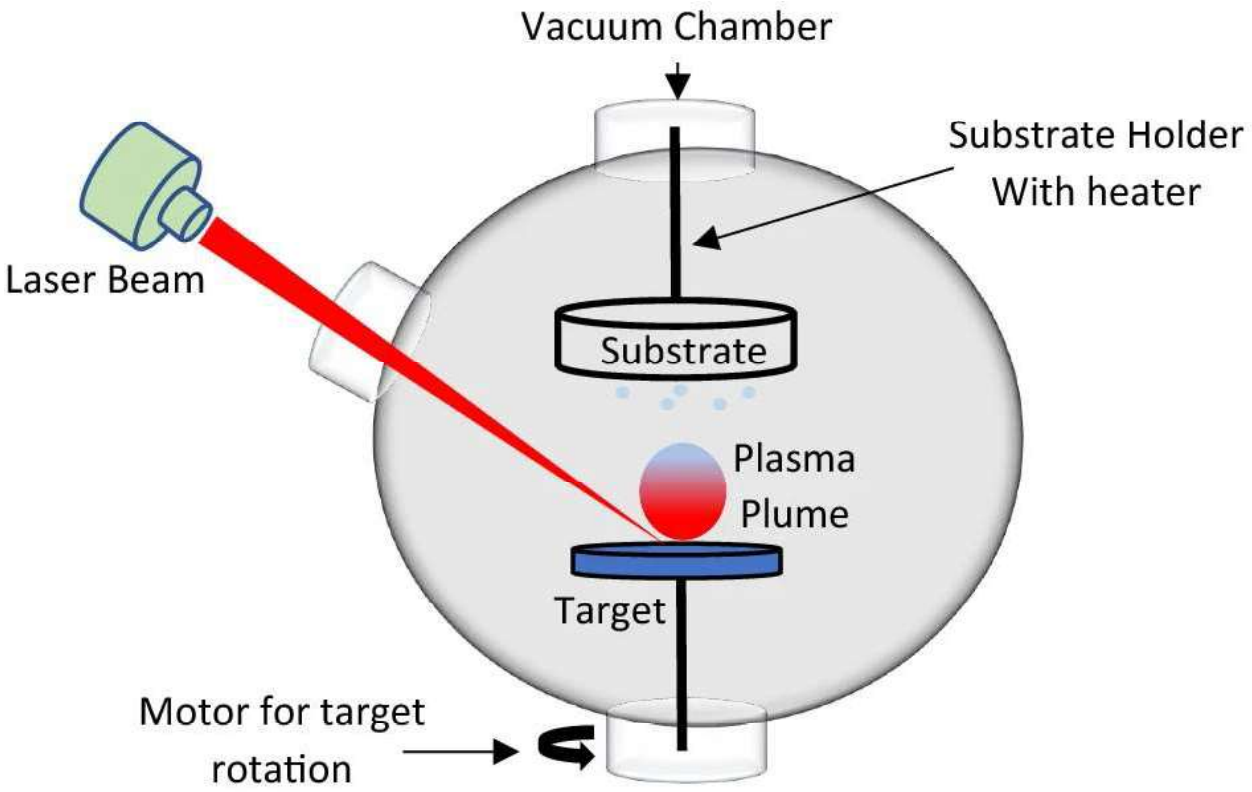

Figure 1.13 Schematic illustration of the pulsed laser deposition method within a vacuum chamber. The process involves the use of a pulsed laser to ablate or remove material from a solid target, which then condenses and deposits onto a substrate. The vacuum environment ensures controlled and precise deposition, making PLD a versatile technique for synthesizing a wide range of materials with diverse properties. [66].

the target surface. Now, envision a scenario where a specific location on the target consistently receives heating from a CW laser source and absorbs the energy. This leads to a significant portion of the energy penetrating deep into the material, thereby establishing a temperature gradient from the target surface to its bulk, resulting in varied vaporization rates [68]. Consequently, this disparate evaporation rate induces fluctuations in the material within the ejected plume over time, potentially yielding low-quality deposition. To counteract such issues, the target undergoes continuous rotation during the deposition process. This rotation ensures uniform heating and vaporization across the target surface, fostering a more controlled and homogeneous thin film deposition.

The intricate interaction between the laser and the material occurs at the atomic scale, facilitated through photon absorption. When the laser's energy is absorbed by the target material, the electrons

within undergo excitation, transitioning to high-energy states. Consequently, the material can rapidly reach extremely high temperatures within a short time frame. This process is best described as phonon-electron coupling, with certain factors influencing its dynamics. These factors include the material absorption coefficient, laser pulse frequency, laser fluence, and target material reflectivity. By taking these factors into account, one can estimate the laser-induced temperature ($T(x,t)$) at any point on the target using the heat flow equation [68]:

$$\rho_i(T)C_{p_i}(T)\frac{\partial T_i(x,t)}{\partial t} = \frac{\partial}{\partial x}\left(K_i(T)\frac{\partial T_i(x,t)}{\partial x}\right) + I_o(t)\left\{1 - R(T)\right\}e^{-\alpha(T)x}, \tag{1.30}$$

Here, the subscript $i = 1, 2$ represents the solid and liquid phases, respectively. $\rho(T)$ and $C_p(T)$ correspond to the temperature-dependent density and thermal heat capacity per unit mass. $R(T)$ and $\alpha(T)$ are the temperature-dependent reflectivity and absorption coefficient of the target material, relevant to the laser wavelength. $I_o(t)$ characterizes the laser intensity, encompassing both its magnitude and shape over time as dictated by the laser pulse. For fast pulsed lasers, radiation heat loss can be neglected at both the front and back sides of the target due to the extremely short timescale involved. At the solid-liquid interface, the temperature can be approximated as follows:

$$T_1 = T_2 = T_x, \tag{1.31}$$

Here, T_1 represents the temperature on the liquid side of the interface, T_2 on the solid side, and T_x can be set equal to the material's melting point (T_m), which is below its actual melting temperature.

Considering the ultrashort timescales involved, typically within the nanosecond or shorter range, the heat conduction of the material can be reasonably assumed to be extremely low. Consequently, the first component of the right-hand side of Equation 1.30 can be neglected. As a result, the target surface temperature at position $x = 0$ can be simplified as follows [66], [68]:

$$\rho(T)C_p(T)\big(T - T_0\big) = (1 - R)I_o\alpha(T)\tau. \tag{1.32}$$

In this expression, T_0 represents the initial temperature of the material, and τ denotes the duration of the laser pulse. Although this simplified equation provides valuable insights into the temperature change during laser-material interactions, obtaining precise numerical values through manual

calculations can prove challenging due to the presence of multiple temperature-dependent terms. Therefore, computational tools, such as COMSOL, are commonly employed to solve this intricate problem accurately. In the subsequent sections of this dissertation, a comprehensive COMSOL simulation of a KrF pulsed laser illuminating a PMMA-coated Si wafer using the heat transfer model will be presented [69]. These simulations will apply the fundamental principles outlined in this section, shedding light on the intricate thermal dynamics that underlie the laser-material interactions.

The thermal effects induced by the laser can be categorized into three distinct processes: vaporization, heterogeneous boiling, and explosive boiling [70]. However, due to the short timescale involved, only vaporization and explosive boiling are typically observed. It is also essential to note that explosive boiling occurs only when the target material's temperature reaches its thermodynamic critical value, making vaporization the predominant ablation mechanism [70], [71]. Thus, this material vaporization flow rate (ν) from the target surface at a given temperature (T) can be described by the Hertz-Knudsen equation [72]:

$$\nu(T) = (1-\beta)\sqrt{\frac{m}{2\pi k_B T}}\frac{P_0}{\rho}\exp\left[\frac{L_v}{k_B}\left(\frac{1}{T_b}-\frac{1}{T}\right)\right], \tag{1.33}$$

Here, β represents the back flux coefficient [73], k_B is the Boltzmann constant, T_B denotes the boiling temperature of the material at pressure p_0, L_v stands for the latent heat of vaporization of the material.

In addition to non-reactive PLD techniques, it is feasible to employ laser energy to break chemical bonds and initiate chemical reactions within the plume. This approach falls under the category of reactive pulsed laser deposition, which will be extensively explored in the subsequent sections of this dissertation, with a specific focus on SiC synthesis.

1.5 SiC Growth History, Challenges, and Si/SiC Diodes Overview

Within the realm of materials science, a prominent pursuit involves the development of wide-bandgap semiconducting materials capable of either substituting traditional silicon in operations under harsh environmental and high power density conditions, or working synergistically with

silicon to enhance device performance [74]. Silicon carbide (SiC) has garnered particular attention due to its exceptional properties, including a tunable wide bandgap (owing to different allotropes), high thermal conductivity, low thermal expansion, commendable chemical inertness, and remarkable material strength [75]–[77]. These distinctive attributes have catapulted SiC into the spotlight, especially in the domains of power electronics and hostile-environment electronics [78]–[80].

SiC exists in various allotropic forms, displaying diverse structures, including cubic, hexagonal, and rhombohedral arrangements. Of particular interest in research are the 3C (β), 4H (α), and 6H types [82], and their structures are illustrated in Figure 1.14. Each SiC type exhibits unique electrical properties, which are comprehensively summarized in Table 1.1. The table also presents a comparative analysis of different SiC allostropes with Si, providing key parameters such as the semiconductor energy bandgap (E_g), electron saturation velocity (ν_{st}), electron mobility (μ_n), material dielectric constant (ϵ_R), strength of the breakdown field (E_c), and thermal conductivity (κ).

To date, a plethora of SiC synthesis methods has been developed, encompassing diverse approaches ranging from nanostructures growth to film synthesis [84], [85]. Among these methods, SiC nanostructures can be classified into distinct categories based on their dimensional characteristics, namely 0D, 1D, 2D, and 3D structures. Each category holds unique applications across various fields, including optoelectronics, drug delivery systems, lightweight catalysts, mesoscopic physics, and energy conversion applications [84], [86]–[89].

This section provides a concise yet comprehensive overview of SiC synthesis methods, accompa-

	Si	3C-SiC	4H-SiC	6H-SiC
E_g (eV)	1.1	2.3	3.3	3
ν_{st} (cm/s)	1×10^7	2.5×10^7	2×10^7	2×10^7
μ_n (cm^2/Vs)	1350	1000	947	380
ϵ_R	11.8	9.66	9.7	9.7
E_c (V/cm)	2×10^5	3×10^6	3×10^6	4×10^6
κ (W/cmK)	1.5	4.9	5	5

Table 1.1 Comparative Analysis of Electrical and Physical Properties in Si, 3C-SiC, 4H-SiC, and 6H-SiC [81]–[83]

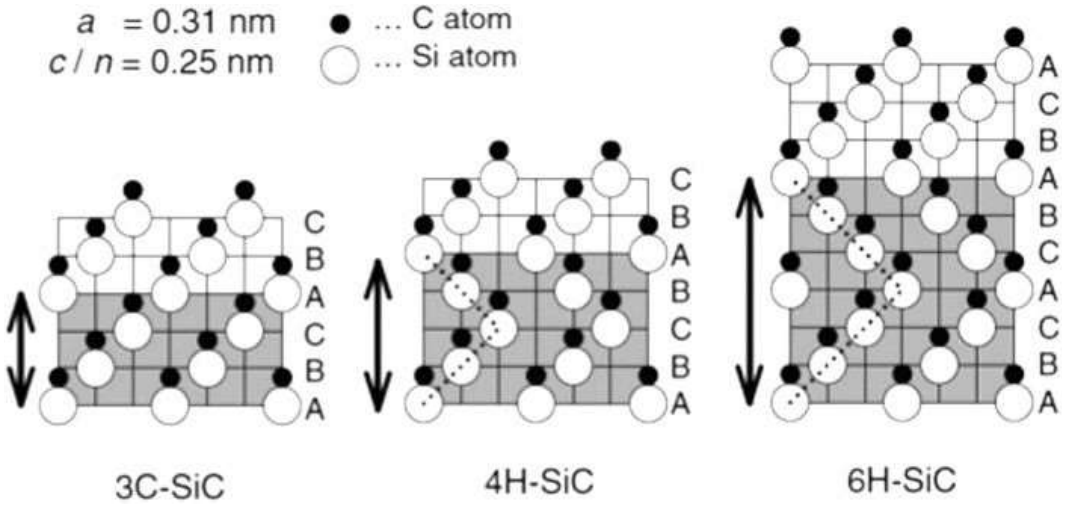

Figure 1.14 Figure illustrates the arrangements of Si and C atoms for 3C-, 4H-, and 6H-SiC. The occupation sites A, B, and C represent the positions within the hexagonal close-packed structures [90].

nied by a general discussion of the advantages and disadvantages of each technique. Understanding the SiC synthesis methods presented in this section is crucial to comprehend the motivation behind developing the proposed method in this dissertation and to recognize the distinct advantages of this novel approach in comparison to traditional methods.

1.5.1 Solid-Phase Synthesis of SiC

As previously mentioned, the investigation of SiC nanomaterials encompasses a diverse array of categories, each intrinsically linked to distinctive synthesis techniques. A focal point in this discussion pertains to methods based on phase differences, including solid-phase synthesis, liquid-phase synthesis, and vapor depositions.

Among the solid-phase synthesis methods, the carbothermal reduction approach stands as the most prevalent [91]. This technique employs a solid-phase precursor, typically silicon oxide (SiO_2), as the source to provide essential Si atoms. Under high-temperature conditions within an inert gas environment, the solid-phase carbon (C) atoms undergo chemical reduction with the silicon precursor, leading to the formation of SiC, alongside the liberation of carbon monoxide (CO) gas [92]. The chemical reaction can be succinctly described as $3\,C + SiO_2 \longrightarrow SiC + 2\,CO$. The versatility of this method is demonstrated by its applicability to different silicon precursors,

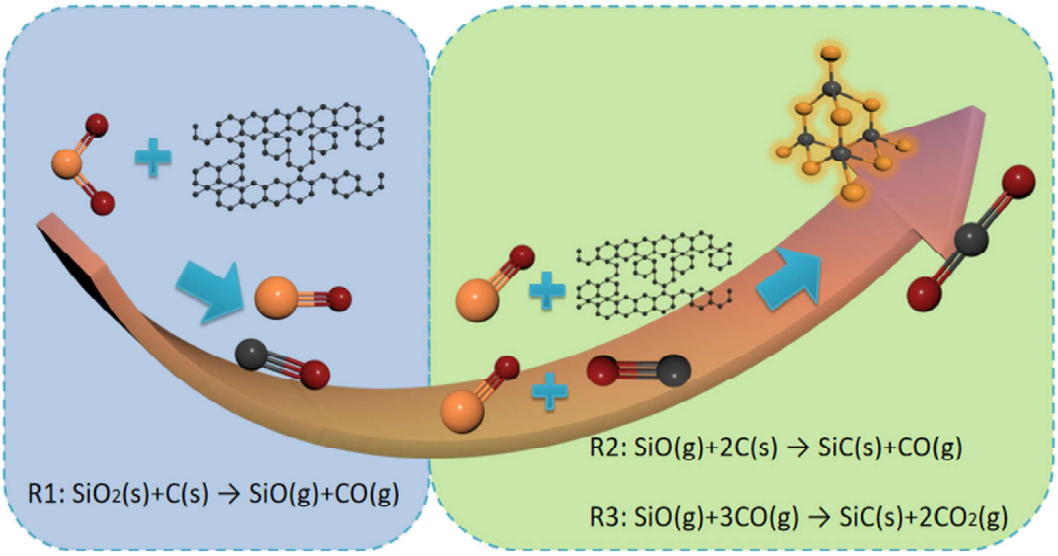

Figure 1.15 Schematic illustration of the general reaction mechanism of carbothermal reduction method [93].

including Si and even SiO. Notably, for the synthesis of high surface area SiC, the method can be adapted using SiO_2-based molecular sieves as an alternative silicon source. By employing diverse precursors and catalysts, it is feasible to lower the reaction temperature and reduce the synthesis time significantly. A comprehensive summary of these approaches is provided in the first half of the Table 1.2 [93].

SiC synthesis can also be achieved by utilizing Si as the primary precursor. Various forms of Si, including Si powder, Si substrate, and Si wafer, can undergo controlled reactions with C atoms under specific conditions to produce SiC nanotubes, nanowires, and nanowhiskers. The latter part of Table 1.2 provides a comprehensive overview of the key parameters for these distinct Si-based SiC synthesis cases.

Upon examining the above findings, it becomes evident that solid-phase synthesis techniques necessitate prolonged operations at high temperatures under atmospheric pressure or vacuum conditions. Moreover, the underlying chemical reactions can potentially lead to the generation of hazardous gases. These observations indicate a clear scope for improvement and innovation in the synthesis method to address these challenges and enhance the overall safety and efficiency of the process.

Si precursor	C precursor	Temp. (°C)	Pressure (kPa)	Time (h)	Product
Silica fume	Phenolic resin powders	1450	101	4	SiC nanowire
Mesoporous silica	Carbon nanotube	1100	101	20	SiC nanotube
Microfine silica	Graphite flakes	1600-1700	101	4	SiC nanoparticle
SiO2 nanoparticle	Glucose	1400	101	2	SiC nanoparticle
OMHS	Carbon nanofiber	1400	101	1	SiC nanofiber

C precursor	Si precursor	Temp. (°C)	Pressure	Time (h)	Product
Carbon nanotube	Si powder	1200	5×10^{-4} Pa	100	SiC nanotube
Multiwalled carbon nanotube	Si powder	1100-1300	5×10^{-2} Pa	5-100	Double-thick-walled SiC nanotube
Graphene powder	Si (111) wafer	1200	101 kPa	2	SiC nanowire
Graphite	Si powder	1300	101 kPa	3	SiC whisker

Table 1.2 Key parameters for various solid-phase SiC synthesis methods [92]–[100]

1.5.2 Liquid-Phase Synthesis of SiC

Liquid-phase synthesis of SiC involves utilizing either liquid reactants or dissolved substances in a solvent to produce highly dispersed SiC nanocrystals. Within this category, two prominent methods are employed: the pyrolysis method and the sol-gel method [101], [102].

In the pyrolysis treatment, a mixture solution of polyureasilazane (PSN) and polyvinylpyrrolidone (PVP) serves as the starting materials. Under argon gas, the solution is heated for one hour at 1400 °C, resulting in the synthesis of 3C-SiC hollow fibers [101]. On the other hand, the solvothermal-assisted sol-gel method employs tetraethyl orthosilicate (TEOS) and phenolic resin as source materials, which are dissolved in ethanol. This process requires a reaction time of several hours at 1600 °C to form SiC nanoparticles [102].

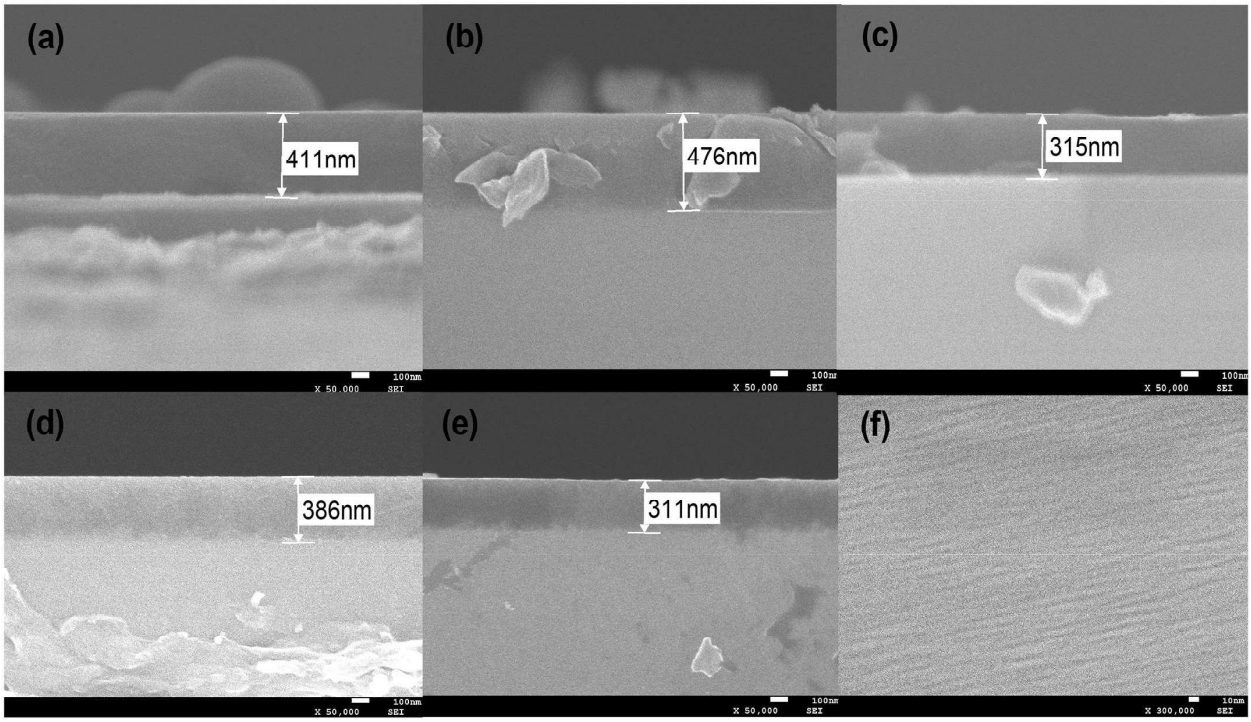

Figure 1.16 Figure displays the cross-sectional view of scanning electron microscopy images depicting the amorphous SiC thin film deposited through chemical vapor deposition. Panels (a) to (e) showcase images with a scale bar of 100 nm, while panel (f) exhibits a more detailed view with a scale bar of 10 nm. [103].

1.5.3 Vapor Deposition of SiC

Chemical vapor deposition (CVD) emerges as an effective surface coating technique, facilitating the production of high-purity SiC materials [93]. In this process, precursor gases are directed into a vacuum chamber housing a heated substrate. Commonly employed carbon sources encompass ethylene, methane, and propane, while silane serves as the silicon source. Within the reaction, the gas mixture undergoes decomposition on the heated substrate, leading to the formation of atomic species. Subsequently, these species engage in reactions, ultimately generating SiC. The resulting product morphologies are influenced by various factors, including chamber temperatures, precursor species, and substrate properties.

CVD represents a versatile and effective method for synthesizing a wide array of SiC nanostructures, encompassing nanowires, nanowhiskers, core-shell nanostructures, and thin films [103]–[106]. Of particular significance is the production of high purity SiC thin films, showcased in Figure 1.16 [103]. In this specific case, a gas mixture containing silane and hydrogen in a 1:9 ratio

serves as the silicon source, while pure methane is employed as the carbon source. The reaction takes place within a relatively lower temperature range of 100°C to 300°C, with a duration of 40 minutes, aided by plasma assistance at 120 W under a pressure of 60 Pa.

Generally speaking, CVD stands as a highly effective technique for yielding high-purity SiC products. Nonetheless, the implementation of CVD demands the use of flammable gases operating under high pressures and elevated temperatures [93]. This can lead to increased equipment costs and pose potential safety concerns, particularly for large-scale production endeavors. These challenges underscore the necessity for cost-effective and expedient SiC synthesis methods that can circumvent the use of hazardous or combustible chemicals.

1.5.4 Si/SiC Diodes and Anderson's Rule

With significant advancements in SiC growth, particularly on Si substrates, researchers have been able to harness higher power outputs from drives while maintaining the same packaging size as pure Si circuits [108]. Nevertheless, certain challenges have hindered further development [109], [110]. The primary issues lie in the substantial lattice mismatch and thermal expansion coefficient differences between the two materials, leading to the accumulation of high densities of residual stress and defects [111]. To address these challenges, the surface-activated bonding (SAB) method is commonly employed [107]. However, this process often results in the formation of high densities of interface states, which can lead to the pinning of the Fermi energy level in a heterojunction diode [112]. The Si/SiC heterostructure's conduction band discontinuities have been reported to exhibit a wide scattering range, from 0.21 eV to 1.9 eV, signifying that the electrical properties of this junction heavily depend on the presence of possible interface states [108], [113].

In this section, we will present current-voltage (IV) measurements of a Si/SiC heterojunction from previous research, using the SAB method, which demonstrates the top performing Si/SiC heterojunctions. While the proposed reactive pulsed laser deposition method in this dissertation may unavoidably lead to the creation of high densities of interface states and defects, significantly degrading device performance, it is crucial to understand the underlying reasons behind these challenges.

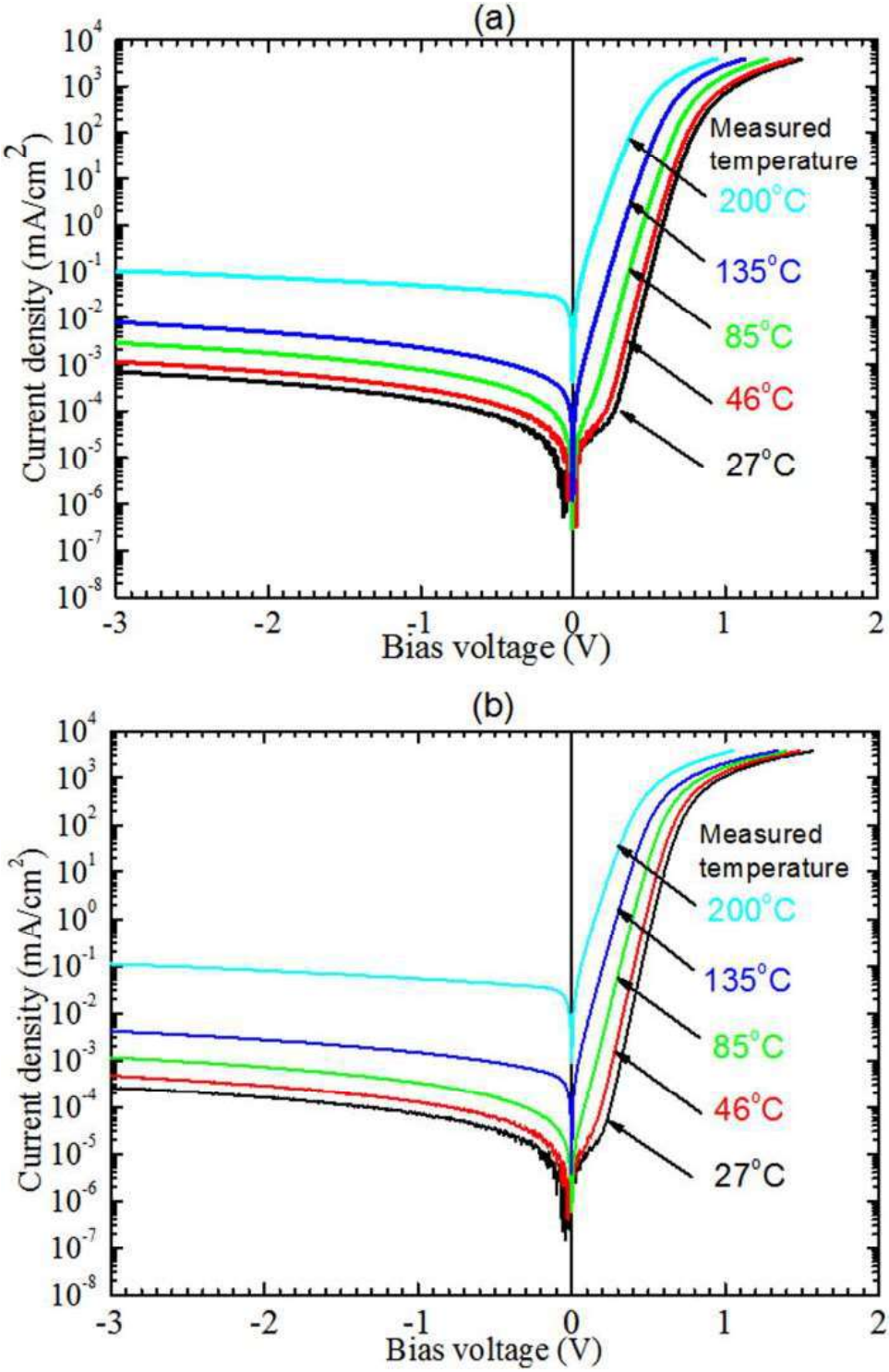

Figure 1.17 Temperature-dependent IV characteristics of (a) p^+-Si/n^--SiC junctions and (b) n^+-Si/n^--SiC junctions [107].

Figure 1.17 presents the IV characteristics of the p^+-Si/n^--SiC and n^+-Si/n^--SiC heterojunctions at various temperatures [107]. The material properties of these junctions can be found in Table 1.3 [107]. For the fabrication process, a thermal annealing step was performed at 400°C and 1000°C for the heterojunction. Ti/Au electrodes were utilized on the Si side, while Ni was employed on the SiC side to form the electrodes.

Type	Carrier concentration (cm^{-3})	Thickness (μm)
n^+-Si	2.61×10^{19}	525
p^+-Si	2.64×10^{19}	525
n^--SiC	$\sim 5\times10^{15}$	2.8

Table 1.3 Physical properties of the investigated semiconductors [107]

The measurements depicted in the figure demonstrate typical pn diode rectifying behavior for both the p^+-Si/n^--SiC and n^+-Si/n^--SiC heterojunctions at different operating temperatures. Notably, as the reverse bias voltage and operating temperature increase, there is a corresponding rise in the reverse bias current. The relationship between the Fermi level difference for these heterojunctions, commonly referred to as the flat-band voltage (V_F), is given by the following expressions:

For the p^+-Si/n^--SiC heterojunction:

$$qV_F = E_{gp} + \Delta E_c - \delta_{n-SiC} - \delta_{p-Si}, \tag{1.34}$$

For the n^+-Si/n^--SiC heterojunction:

$$qV_F = \Delta E_c - \delta_{n-SiC} + \delta_{n-Si}. \tag{1.35}$$

Here, q represents the electron charge, E_{gp} is the bandgap of p^+-Si, ΔE_c represents the conduction band discontinuity, and δ_n and δ_p indicate the position difference of the Fermi level with respect to the conduction band and valence band, respectively. The subscripts $_{-Si}$ and $_{-SiC}$ indicate the type of material being referred to.

Based on the provided equations and material properties, the estimated values of ΔE_c for the p^+-Si/n^--SiC and n^+-Si/n^--SiC junctions are found to be 0.05 eV and 1.09 eV, respectively. The

similarity in the current-voltage behavior observed in the measured results, along with the disparity between the measured and estimated values from the aforementioned equations, strongly suggests the presence of high densities of interface trap states within the junctions [107]. These trap states at the bonding interface are responsible for the pinning of the Fermi energy level.

The Anderson's rule, first proposed by R. L. Anderson in 1960 [114], serves as a valuable tool for analyzing heterojunctions with similar structures, which will be beneficial for the analysis presented in this dissertation. This rule enables the construction of energy band diagrams between two different semiconductor materials, as observed in heterojunctions, such as the Si/SiC junction used as an example here. According to Anderson's rule, when building the band diagram, the vacuum level on both sides of the heterojunction should align at the same level. This allows the estimation of conduction and valence band offsets using the electron affinity and material bandgap values. Employing this concept, we generate an example band diagram for both the n-Si and n-SiC materials, as depicted in Figure 1.18 before contact, which will be applicable to the analysis of the Si/SiC device in subsequent sections of this dissertation.

Upon achieving alignment of the vacuum level, the band bending in both sides of the semiconductors can be calculated, as illustrated in Figure 1.19. By setting the bands of n-Si as the position references, it follows that both the conduction and valence band bending of n-SiC will be equal to qV_F.

1.6 Miscellaneous Findings and Observations

1.6.1 Beam Homogenization

Laser-based micro-machining techniques often necessitate a uniform laser intensity profile [115]. Similarly, when implementing the reactive pulse laser deposition technique for SiC, achieving a homogeneous intensity profile is essential. To achieve this requirement, a beam homogenizer is employed to shape the laser intensity profile.

Various classical methods for laser beam homogenization have been explored, such as diffractive optical elements (DOE), aspheric lenses, and polygon homogenized rods [116]–[118]. While both DOE and aspheric lenses can shape the laser beam into a flat-top profile, they present drawbacks,

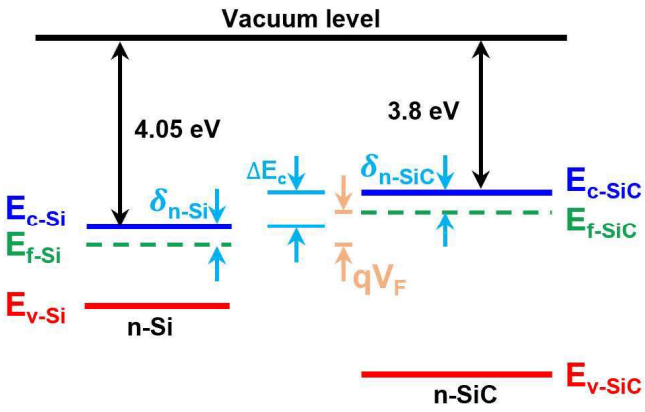

Figure 1.18 Energy band diagram at the interface of n-Si and n-SiC materials prior to contact, demonstrating the use of Anderson's rule.

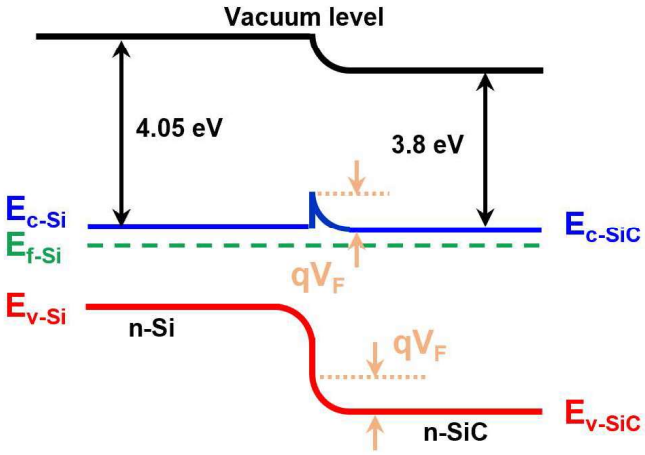

Figure 1.19 Energy band diagram at the interface of n-Si and n-SiC materials after contact: illustrating the electronic energy levels alignment across the semiconductor junction.

including the requirement for highly specified entrance intensity distributions and precise alignment [119]. On the other hand, polygon homogenized rods offer independence from the incident intensity profile, but they suffer from transmission losses due to their longer rod length [120].

However, recent advancements have overcome these limitations through the use of microlens array-based homogenization systems [121]. These systems offer several advantages, including the absence of specific requirements on the incident laser profile and relatively high conversion efficiency. Nonetheless, one issue to consider when using this system is the potential light diffraction effect, especially when dealing with highly coherent light [119].

In general, two widely applied types of microlens arrays are commonly utilized: the single and

dual lens array homogenizers. For the purposes of this dissertation, the single lens array was chosen to mitigate the diffraction effect. The specific microlens array (Edmund Optics) used is depicted in Figure 1.20, featuring precise dimensions for the array. Each individual lens in this array serves to divide the incident wavefront into separate beams. Subsequently, these divided beams are then focused onto the target area using a dedicated focusing lens, thus forming a comprehensive and efficient homogenization system, as illustrated in Figure 1.21.

To determine the product dimension (D_{FT}) at the homogenized plane, we use the following equation:

$$D_{FT} = \frac{f_{FL}}{f_0} p, \tag{1.36}$$

where f_{FL} represents the focal length of the focusing lens, and f_0 is the focal length of the microlens array.

1.6.2 Understanding the SiC Crystal defects

3C-SiC, a cubic variant distinguished by its orderly bilayer stacking arrangement of ABCABC..., resulting in a pristine zinc-blende structure. When aiming to maximize the growth area of 3C-SiC, silicon (Si) emerges as a particularly compelling choice for substrate material and crystal seed for both thin film growth and bulk 3C-SiC synthesis. However, this narrative is not without its challenges. As elucidated in the preceding section, the growth of 3C-SiC on a silicon substrate encounters notable challenges due to substantial mismatches in lattice parameters and thermal expansion coefficients [111]. Within the unfolding chronicle of 3C-SiC's growth, defects emerge as pivotal characters, casting nuanced shadows upon the crystal's pristine landscape. This ensemble of crystal imperfections includes volume defects, among which micro-twins (MTs), anti-phase boundaries (APBs), and protrusions play distinctive roles. In addition, stacking faults, known as planar defects, and their counterparts in the form of line defects weave a complex narrative. It is noteworthy that some of these defects, such as MTs, have shown a propensity to diminish as the thickness of the films increases. However, in a general context, extended defects tend to reduce in density but seldom entirely vanish [122].

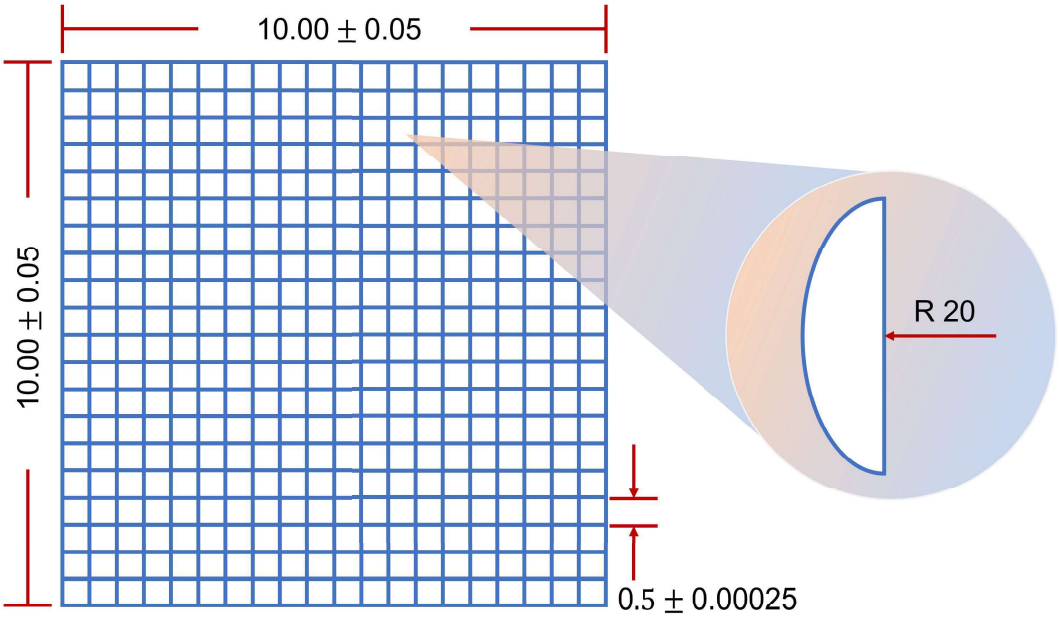

Figure 1.20 Dimensions of the fused silica microlens array (Edmund Optics) utilized in the subsequent sections of this dissertation, all measurements presented in inches (in).

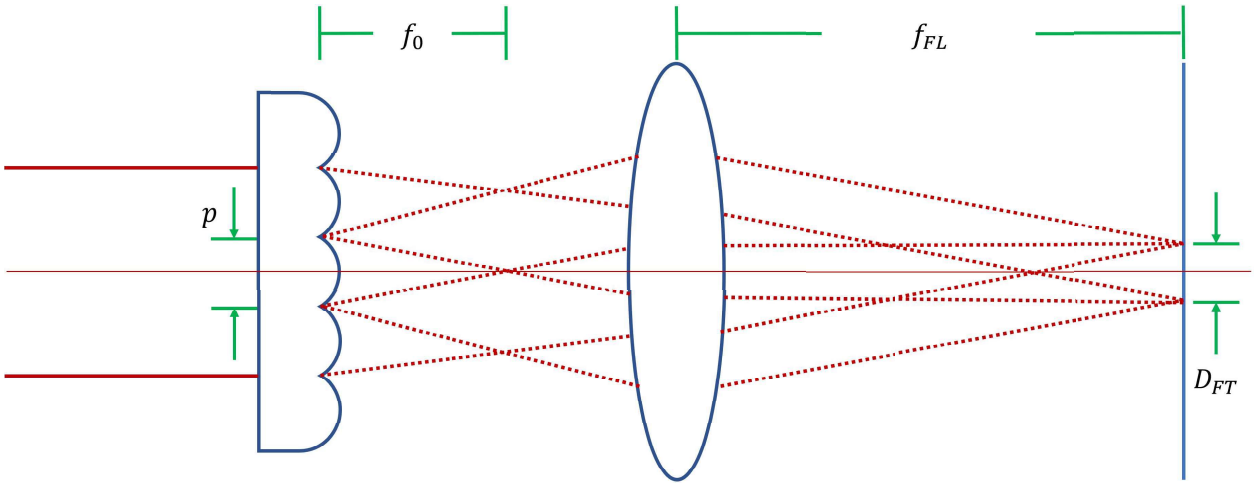

Figure 1.21 Schematic representation of the single lens array homogenization system, showcasing the dimensions of the setup.

To mitigate defects during film growth, a self-annihilation mechanism typically comes into play. Many of these defects, including stacking faults (SFs) and micro-twins (MTs), exhibit propagation along opposing crystallographic directions, ultimately converging within the film [123]. Moreover, some of these defects originate during the film's growth phase, primarily due to localized strain fields or inaccuracies in the sequential arrangement during deposition. Consequently, defects such

as stacking faults undergo a reduction in density, yet they tend to approach a saturation point without complete elimination. Consequently, as the thickness of 3C-SiC increases, the defect density within SiC decreases. Regardless of the specific defect considered, their density remains notably elevated when producing thin 3C-SiC films. In other words, this phenomenon is accentuated when the proximity to the Si substrate interface is close [122].

CHAPTER 2

UTILIZING PLASMONIC NANOSTRUCTURES TO ENHANCE LIGHT ABSORPTION IN SEMICONDUCTOR DEVICES

2.1 Background Knowledge

Energy conversion using plasmonic nanoresonators has become a popular topic when facilitating electron-hole pair separation processes as the way to increase photon-to-electron conversion efficiency for photoelectric devices. Accompanying the first photodetector fabricated, energy conversion efficiency has risen as the key factor, which affects the responsivity directly as well as the sensitivity of a photodetector. Plasmonic nanoresonators have been shown in previous studies as a way to enhance responsivity [124]. Nanostructures not only have good performance and a major contribution to the photocurrent but also can be easily fabricated on existing devices without changing their original layout. In Xi's research, the solar cell with wet chemical nucleated silver 200 nm nanoparticles achieved a broadband absorption enhancement compared to the solar cell without nanoparticles [125]. A 14.3% enhancement in short-circuit photocurrent density and a 23% increase in energy conversion efficiency are reported when comparing to the plain solar cell. Besides, due to the strong light-matter interaction property, the plasmonic concept permits a noticeable reduction in device physical thickness while maintaining the light absorption rate. Commercially, most crystalline silicon-based solar cells in the market have a thickness ranging from 180 μm to 300 μm and the cost of silicon material and processing remain high [126]. As a result, thin-film solar cells with thickness 1-2 μm have gained great interest. However, the main challenge for thin-film solar cells is the resulting low light absorption especially for those made by indirect bandgap semiconductors, such as the Si. Therefore, trapping light inside the material and increasing the absorptance becomes critical for such thin-film solar cells. Fortunately, plasmonic nanostructures have promising solutions to the problem. In Pillai's research, silver nanoparticles exhibit light absorption enhancement nearly over the entire solar spectrum [127]. After nanoparticle deposition, a 7-fold increase was observed for the traditional wafer-based solar cell at 1200 nm wavelength, and up to 12-fold increase at 1050 nm wavelength for the 1.25 μm thick silicon solar

cell was observed.

Before discussing plasmonic nanoresonators and surface plasmon enhanced photovoltaic devices, the term "plasma" has to be clarified. Plasma, the fourth state of matter, generates when the applied energy or temperature is extremely high. It can be understood as a kind of ionized or electrically charged gas. When electrons absorb energy from photons having energies greater than the barrier between the metal nanoparticles and the semiconductor, these energetic electrons can transfer from the metal to the adjacent semiconductor. If electrodes are connected to the semiconductor material, energetic electrons can join the flowing photocurrents, which results in a measurable change in resistance of the semiconductor. Material choices for the metal nanoparticles and the semiconductor also affect the energy barrier at the interface, and the geometrical shape and spacing of the nanoparticles influence the plasmon resonant frequency and hence the optimal absorption wavelength of the incident light. With such adjustable parameters, there has been considerable interest in nanoresonator-based plasmonics recently.

Anisotropic geometrical nanoarray structures can lead to strong dependences on the light polarization. Some scientists have reported rotational symmetry structures to have better performance for varying polarization of the light [128]. The ultra-high light contrast in the article is due to the intense electromagnetic field raised by the nanostructure. When photons with energies greater than the metal-semiconductor barrier height impinge on the structure, energetic electrons from the nanostructure metal will transfer to the semiconductor and contribute to the photocurrent. Less energetic visible and near-infrared range photons are major components in the solar spectrum and although they are unable to excite electrons across the bandgap in the semiconductor, they can be absorbed in the metal nanostructures. This phenomenon was observed in my experiments, where the molybdenum disulfide semiconductor has a larger bandgap (1.88 eV) than the near-infrared incident photons (840 nm) but with the nanoarray structure, photons were absorbed.

There are two mechanisms behind surface plasmons enhancing electron injection into the semiconductor, direct energy conversion through localized surface plasmon resonance (LSPR) excitation, and indirect energy conversion through surface plasmon polaritons (SPPs) [130]. Direct

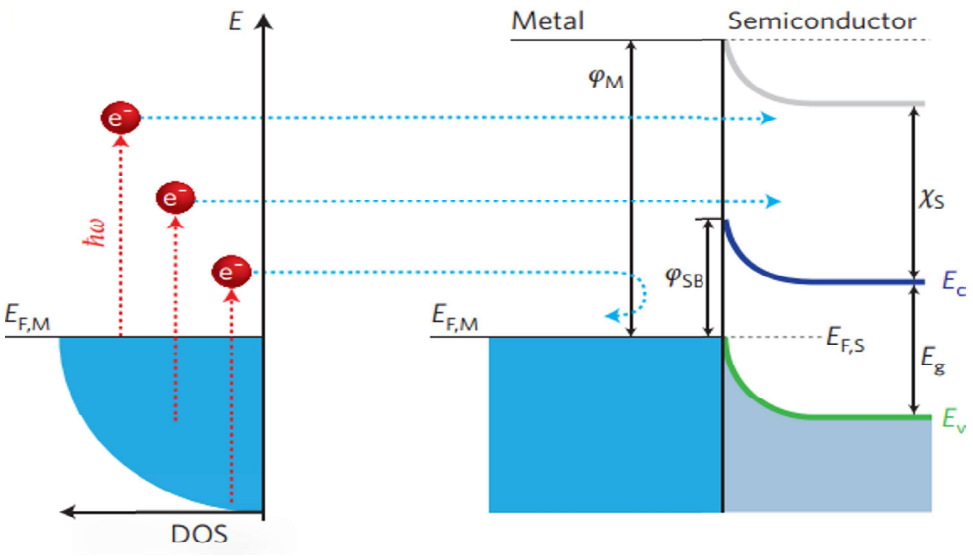

Figure 2.1 Plasmonic energy conversion. Image is from Clavero, et al [129].

LSPR excitation, as shown in Figure 2.1, happens when light is illuminated on metallic nanoantennas (NAs), which can be seen as a light-trapping process. During plasma decay, energy can transfer to electrons. Free electrons confined at the surface of the metal with high energy can escape from the nanostructures and be collected at the contacts to the semiconductor [131]. Those highly energetic electrons can stay in the conduction band of the semiconductor and contribute to the electric circuit, resulting a dynamic Schottky barrier and reducing the resistance of the semiconductor. In this context, the surplus positive charges residing on the nanostructure act as holes, facilitating oxidation reactions. Conversely, the loss of electrons leads to positively charged particles, progressively hindering further electron loss. As a result, the overall efficiency of the system relies on the rate at which electrons are replenished to the nanostructure from either the semiconductor or the surrounding environment [132].

The second mechanism is an indirect energy conversion process. After illumination, the SPP waves on the metal nanostructures can produce large magnitude electric fields between metal nanostructures and into the semiconductor. The enhanced electromagnetic field in the semiconductor can cause direct electron excitation and also increase the carrier count within the current, thus reducing the resistance of the semiconductor.

$$I = I_o(e^{\frac{qV}{\eta k_B T}} - 1) - I_{op} \tag{2.1}$$

$$I_{Therm}|_{s\to m} = I_{s\to m} + I_{m\to s} = \frac{4\pi q m^*(k_B T)^2}{h^3} \cdot e^{-\frac{q\phi_B}{k_B T}} \cdot \left[e^{\frac{qV}{k_B T}} - 1\right] \tag{2.2}$$

$$W \approx \sqrt{\frac{2\varepsilon_s(\phi_i - V)}{qN_d}} \tag{2.3}$$

With injected electrons accumulate near the junction of the nanostructure-semiconductor interfaces, the Fermi energy level shifts toward the conduction band in the semiconductor, assuming n-type semiconductor is used, which results in lowering the contact Schottky barrier height. Allowing more electrons injected into the semiconductor from metals through thermionic emission. Another approach to understanding the change in the semiconductor due to electron movements is to project the model as a light-sensitive p-n junction diode as in Figure 2.2. The diode equation can be expressed as in equation 2.1, where $I, V, q, n, k, T, I_o, I_{op}$ are diode current, diode voltage, electron charge, semiconductor ideality factor (1 for monolayer MoS_2 material), Boltzmann's constant, temperature, reverse saturation current, and light-induced current respectively. The light-induced current then can be written as $I_{op} = qAg_{op}(L_p + L_n + W)$, where A, g_{op}, L, and W are lighting area, material absorption rate, carrier diffusion length, and depletion width respectively. For our case, due to the semiconductor-gold nanostructure open-circuit layout, we can replace the p-side as MoS_2 material, n-side as the gold, and eliminate the total current I. It allows us to map the voltage difference between two sides directly to the light-material interaction. With an increased I_{op}, the effective bias voltage, V, increases correspondingly, which increases the thermionic current flow across the junction and the number of electrons injected into nearby MoS_2 semiconductors as well.

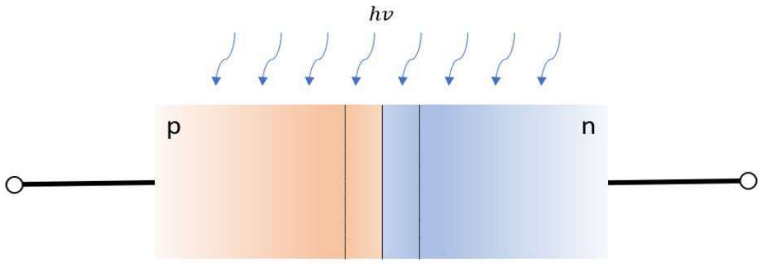

Figure 2.2 pn junction diode.

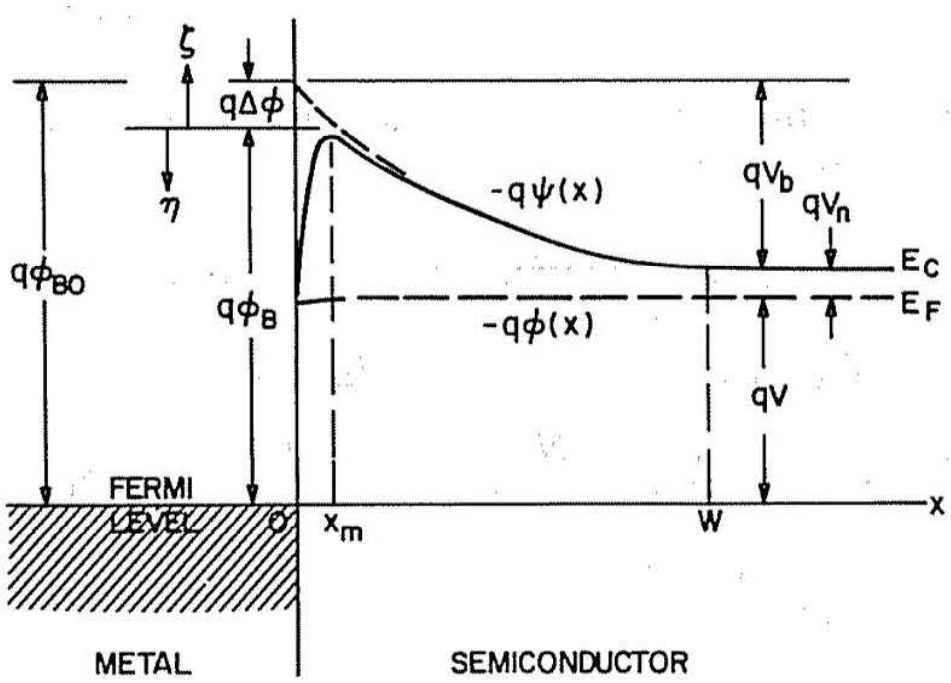

Figure 2.3 Metal-semiconductor junction. Image is from Sze, et al [133].

Figure 2.3 shows the band bending diagram with respect to the potential and the instant thermionic current, I_{Therm}, which can be estimated by using equation 2.2 with thermal energy k_BT, Planck's constant h, effective electron mass m^*, and barrier height ϕ_B.

Since a p-type MoS_2 was obtained in our experiment and the metal-semiconductor configuration, the depletion region extend into the MoS_2, which has a relationship that corresponds to the effective bias voltage expressed as in equation 2.3, where ϕ_i, N_d, and ε_s are junction build-in potential, donor density, and MoS_2 dielectric constant. Note that the dielectric constant of the MoS_2 material can be tuned by varying the external electric field [134].

Now, the two most basic issues are what is the corresponding resonance frequency for light-matter oscillations and how much electric field enhancement can the nanostructure induce. Thanks to Prashant's contribution, the localized surface plasmon resonance frequency in metal particles is well defined as below [135]:

$$\omega_{sp} = \sqrt{\frac{Ne^2}{m_e\epsilon_o(\epsilon_\infty + k\epsilon_m)}} \tag{2.4}$$

where N is the density of free electrons, e is the electric charge, m_e is the mass of a free electron, ϵ_0 is the permittivity of free space, ϵ_∞ is the high-frequency part of the dielectric function of the

metal, k is the shape factor that incorporates the polarizability on the geometry of the surface and ϵ_m is the medium dielectric constant. The equation is set up based on the fact that when the size of the nanoparticle, r, is much smaller than the wavelength, λ, of the incident light, $r \ll \lambda$, the predominant electron oscillation can be simplified as a dipolar oscillation [135]. In other words, the electron collective movement on the nanostructures can be described as a dipolar movement under an incident electromagnetic field. This equation also considers the inter-band transitions from the valence to the conduction band in the metal under high-frequency incident conditions by adding the high-frequency term, ϵ_∞. Note that the electron resonance frequency is determined by the real part of the metal-dielectric function and the broadening of the frequency is determined by the imaginary part of the function. By figuring out the shape factor ($k = -\frac{\epsilon_r}{\epsilon_m}$) based on the actual structure design, we can directly apply the equation and find the resonance frequency.

In Genov's work, the average electromagnetic field enhancement factor $\bar{G}$, over each unit cell, is well illustrated [136]. The reason why the average value is focused on in this report is that it has a better relevance to the overall design. An absolute high enhancement factor at a particular point does not reflect the performance throughout the entire sample. When analyzing the result for the average values, incident light polarization does not play a significant role either. This is illustrated in Genov's work. With the change in incident polarization angle change from 0° to 45°, $\bar{G}$ value only decreases by a factor of 2, as shown in Figure 2.4.

Genov and his group modeled the electromagnetic coupling inside the plasmonic system as an RLC circuit (Figure 2.5) and solved the average enhancement factor as:

$$\bar{G} = \left\langle \left| \frac{E_{log}(\lambda)}{E_0(\lambda)} \right|^4 \right\rangle \cong \frac{\pi(W+1)^{7/2}}{2((4-\pi)W+4)k_{loss}^{7/2}} \times \sqrt{\frac{4\Delta^2+9}{(\Delta^2+1)^{3/2}} - \frac{\Delta(4\Delta^4+15\Delta^2+15)}{(\Delta^2+1)^3}} \tag{2.5}$$

$$W = \frac{|\epsilon_m'|}{\epsilon_d} \tag{2.6}$$

$$\Delta = \frac{\frac{W}{\gamma} - 1}{k_{loss}} \tag{2.7}$$

where E_0 stands for the incident electrical field, E_{loc} is the local electrical field, ϵ_d is the dielectric medium, ϵ_m is the permittivity of the metal, k_{loss} is the loss factor, γ is the geometric parameter,

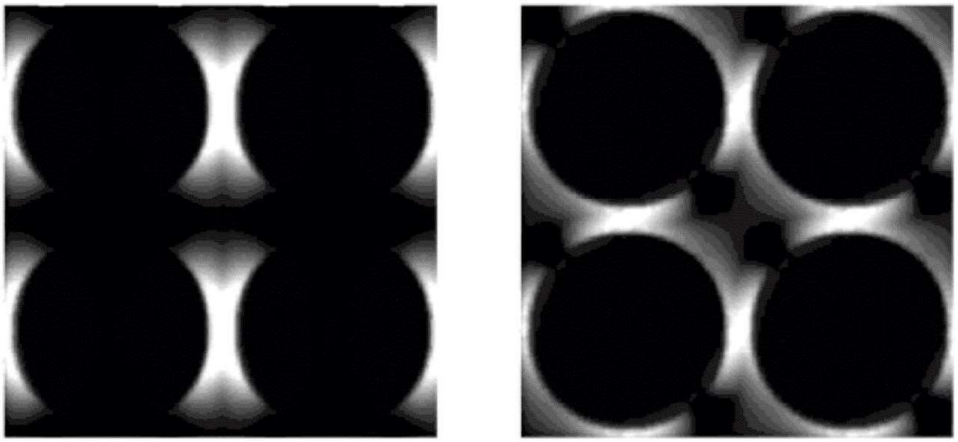

Figure 2.4 Electromagnetic field and field intensity distributions with 0° (left) and 45° (right) polarization angles. Image is from Genov, et al [136].

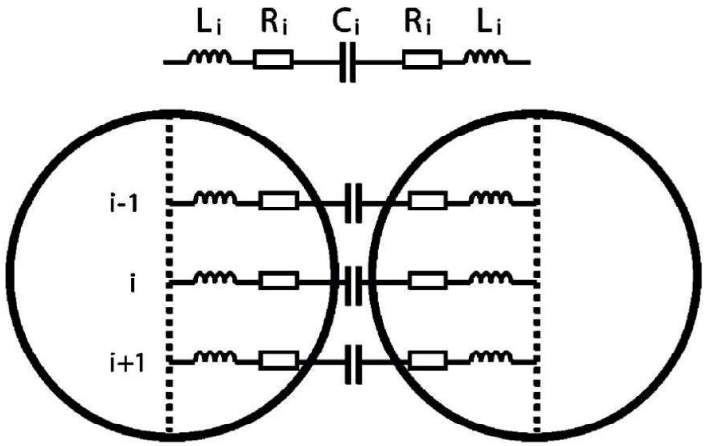

Figure 2.5 Frequency-dependent plasmon response as an RLC circuit. Image is from Genov, et al [136].

d is the particle diameter, and δ is the interparticle spacing, respectively. The loss factor can be calculated from $\epsilon = \epsilon^{'}(1 - ik_{loss})$ and the geometric factor expresses the size-spacing relationship, $\gamma = \frac{d}{\delta}$. From equation 2.5, we know the average electromagnetic field over the unit cell will reach its maximum when Δ goes to 0. Since the entire equation heavily relies on the size-spacing ratio, γ, one can conclude that nanostructures can generate larger $\bar{G}$ with the γ close to W, where the trend can be found in a given example in Genov's paper as in Figure 2.6. The trend indicates that the desired layout design should have a large diameter with small interparticle spacing. However, for real systems, a large diameter structure will block the incident light and result in low conversion efficiency. Moreover, shrinking the gap below ~10 nm remains challenging

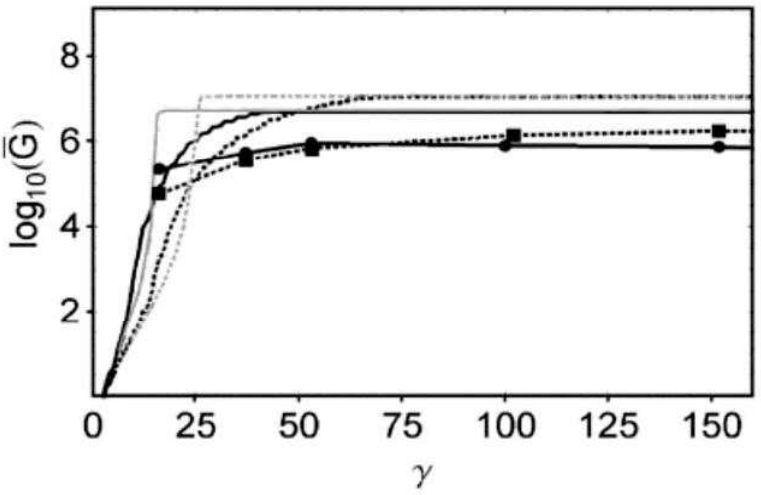

Figure 2.6 Average EM enhancements with respect to γ for 2D hexagonal arrays of Au nanospheres under 647 nm and 785 nm illuminations. Image is from Genov, et al [136].

with the current fabrication technology. It is not feasible to infinitely shrink the size while keeping high accuracy. Unpredictable shapes and interparticle spacings can result in significant changes in device performance, especially in shifting absorption peaks [137].

To minimize the fabrication difficulties and bypass the metal structure separation limitation, scientists have developed novel approaches to increase the photoresponses of plasmonic devices. For instance, Knight's group showed that the plasmonic decay path can be tripled by embedding the plasmonic structure into the semiconductor material [138]. This novel design yielded a substantial increase in photoresponsivity, approximately 25 times higher compared to traditional planar configurations. This enhancement can be attributed to the efficient transportation of excited electrons across the junction interfaces within the range of their mean free path. The result indicates that the contact geometry between the metal plasmonic structure and semiconductor plays a key role in facilitating energy tranfer from the photon to the electron. Research from Sobhani's group further investigated the electron movement in a nanograting plasmonic device [139]. From their simulation result, both the main absorption and electron generation occur near the adjacent area between the metal-semiconductor junction areas. Excited electron transportation, therefore, can be tuned by varying the feature size to expand the flow channel. The highest photoresponsivity in the infrared region can be achieved about 10 times higher (~600 nA/mW) than the previous report. When

applying the plasmonic nanostructure into a two-dimensional material, the embedded design may not be valid anymore due to the small thickness of the semiconductor material. However, the theory that plasmonic nanostructures can enhance photoresponses has been shown in previous research. Li's group demonstrated that a nanoparticle grating based MoS_2 photodevice can achieve more than 100 times higher photoresponses comparing to bare MoS_2 devices under 532 nm light incidence by enhancing the absorption through the localized surface plasmons coupling [140]. Even though these achievements are significant, the two-dimensional material-based plasmonic devices still suffer from low light absorption efficiency of the material itself. The common trend to further increase the photoresponss is summarized in shrinking the interparticle gaps into the nanometer range, where fabrication difficulties become an obstacle.

In this research, a novel sandwiched double-layer plasmonic nanostructure device was investigated. In this device, a thin layer of molybdenum disulfide (MoS_2) semiconductor was inserted between metal structures for electron-hole pair generation. The metal structures are responsible for the plasmonic effect, and the gap between the top and bottom layer structures can be reduced down to atomic dimensions since it is fully dependent on the thickness of the semiconductor between the gold nanoarrays. Due to the strong light-matter coupling and the corresponding absorption spectrum, we choose MoS_2 as the semiconductor [141]. It can be replaced by other two-dimensional (2D) materials for distinct properties in future studies.

The nonlinear optical phenomenon was also studied as part of this work. Due to the complex metal structures, nonlinear absorption is expected but the optical detection performance remained unknown. To further investigate this, a hyperspectral stimulated Raman scattering imaging (hsSRS) system to explore two-color two-photon absorption (2PA) was used. Higher-order nonlinear phenomena are typically very weak, and this hsSRS system is capable of detecting such small signals. The study obtained a fundamental understanding of 2PA excitation in the structure, which might be helpful for other uses.

2.2 Finite Difference Time Domain Simulation

In the previous section, equation 2.5 was introduced to find the maximum average field enhancement factor and a simple estimation method using a size-spacing ratio. In addition, finite difference time domain (FDTD) simulations were used for comparison with the results from equation 2.5. Research has shown this method is valid for local field enhancement calculations [142]–[144]. Since the research structure design focuses on the vertical gap, the nanostructure parameters are intentionally chosen as follows: 110 nm for the two layers' lateral displacement, 160 nm for nanodisk diameter, 25 nm for the nanodisk height, and the same setup for both top and bottom layers was used, as shown in Figure 2.7(a).

For simulation purposes, a slight modification from the actual fabricated device was used with the top layer set to be two rows in order to make the structure symmetric and help reduce the simulation time. A 1 V/m polarized plane wave was simulated to be coming in from the top, polarized along the x-axis and the wavelength of the incident plane wave swept from 300 nm to 1100 nm. The optical energy coupled to the nanoarrays, and consequently to the MoS_2 layer, is directly influenced by the wavelength at which maximum absorption occurs and the magnitude of absorption. These factors significantly impact the optical detection performance of the device, as they determine the amount of optical energy absorbed by the system.

With an x-axis polarized 830 nm incident wave, the electric field enhancement over the unit cell is plotted as in Figure 2.7(b). For simplicity, data were extracted from the middle plane between the top and bottom layers for the remaining simulation results. One can find high electric field locations, or "hotspots" around the boundary of the structures especially at the cross points where nanoarray discs overlap from the top and bottom arrays. A scale bar was introduced to evaluate the enhancement factor defined as E_{loc}/E_0, where E_{loc} is the induced local field and E_0 is the incident field, 1 V/m. Maximum enhancement was calculated to reach up to 25 times the original. As discussed before, the induced electric field can contribute to electron injection as well as photon absorption. The smaller the interparticle distance, the larger the electric field is obtained. In this design, the closest points are the overlay boundary cross points. A 3D E field distribution

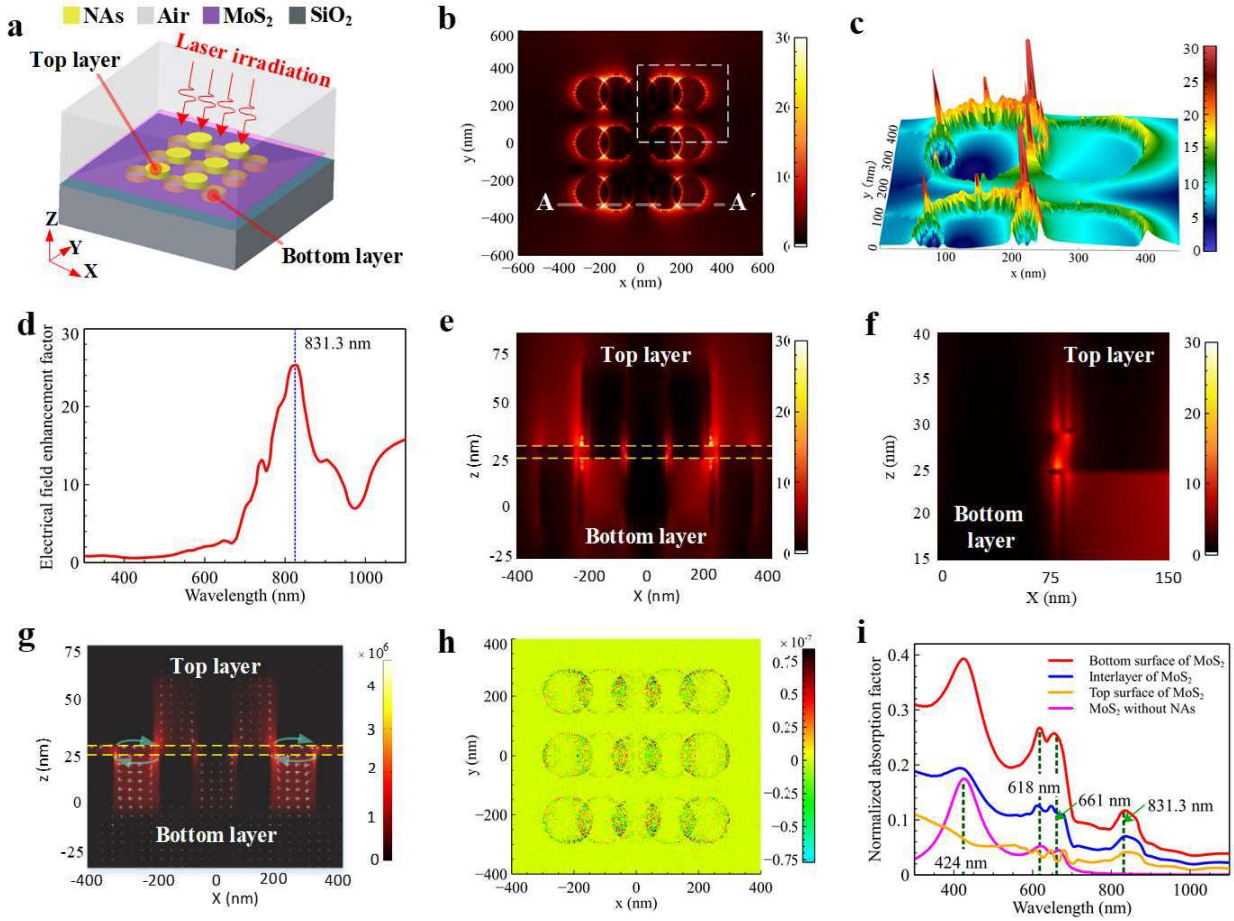

Figure 2.7 FDTD simulation of the proposed photodetector structure. (a) Sandwiched structure schematic. (b) Top view of the electrical field distribution under 831.3 nm laser illumination. (c) In this figure, the vertical gap between top and bottom nanostructures is set to be 5 nm, which is determined by the semiconductor thickness. (d) Variation of the maximum electric field enhancement factor as a function of the incident laser wavelength. (e, f) Lateral view of the electric field distribution on the excited NAs pattern along the A-A' plane, as highlighted in (b). (g) Current density distribution within the NAs. (h) Energetic carrier distribution at the interlayer of MoS_2. (i) Normalized absorption factor of MoS_2 nanosheet with and without NAs.

of the boxed area in Figure 2.7(b) is shown in Figure 2.7(c). The highest intensity locations are distinguished from other areas, which further supports the theory.

Figure 2.7(d) shows the enhancement peak occurs at 831.3 nm with a 25-fold increase and there is more than 10 times enhancement above the 1000 nm range. Recall, this FDTD simulation does not only simulate the metal structures. A thin layer of MoS_2 semiconductor material is inserted in the middle and the physical property shows the bandgap of the semiconductor is 1.88 eV, which corresponding to 659.5 nm wavelength. This means at a wavelength above 659.5 nm, even though there is an electric field enhancement, it may not correspond to absorption in an actual device. However, both the FDTD simulation and the real practice indicate that MoS_2 has absorption beyond 659.5 nm, which will be illustrated later.

To assess the local electric field coverage, we analyzed the electric field distribution along the XZ plane (as depicted by the white dashed line A-A' in Figure 2.7(b)). In Figure 2.7(e), we present the cross-section view showcasing the distribution. The effective region of electric field enhancement, measured in terms of width and height, was approximately 10 nm × 16 nm (Figure 2.7(f)). This observation aligns with the LSPR decay theory [13] and indicates that the enhanced electric field adequately covers the thickness of the MoS_2 nanosheet.

Examining the current density distribution near the A-A' cross-section (Figure 2.7(g)), we observed a direct correlation between the current density and the local electric field enhancement depicted in Figure 2.7(e). The maximum current density was observed at the vertical gap, indicating that the excitation of light effectively enhances the carrier concentration inside the MoS_2 nanosheet at this specific location. The energy flux direction, represented by the Poynting vector, was also illustrated in Figure 2.7(g). Notably, an energy flow circle formed within the MoS_2, as indicated by the blue arrows.

Considering the pivotal role of carrier concentration in photocurrent formation, we calculated and plotted the distribution of energetic carriers at the interlayer of MoS_2 in Figure 2.7(h). By leveraging the built-in electric field, energetic carriers generated from plasmonic decay can be efficiently transferred from Au nanoantennas to the MoS_2 nanosheet. This transfer mechanism

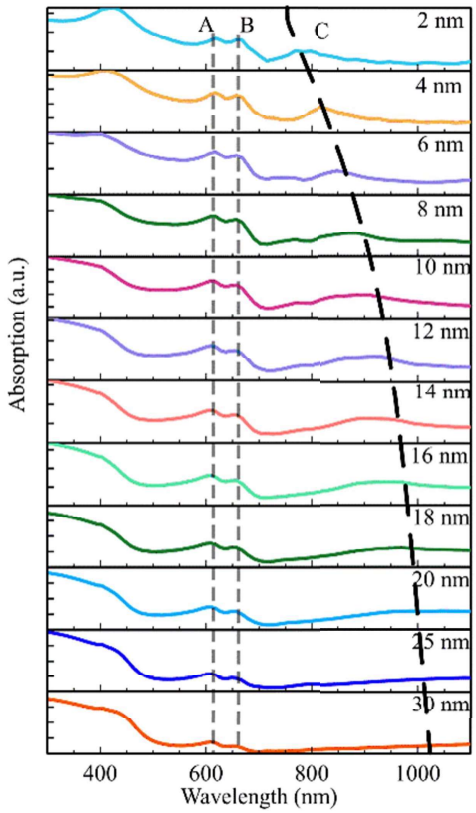

Figure 2.8 Variation of the absorption with MoS_2 thickness.

holds promise for enhancing photocurrent, photosensitivity, and the overall performance of the fabricated photodetector.

To predict the result, a normalized absorption curve with respect to incident wavelength is plotted in Figure 2.7(i). From this figure, it is clear that without any structure, a bare MoS_2 device does not absorb incident light that is above 661 nm. However, with the sandwiched nanoarray structure proposed the absorption is increased over the entire spectrum and new absorption peaks relative to the bare MoS_2 can be seen. This shows that the double-layer plasmonic nanostructure is responsible for the device response to near-infrared wavelengths.

The simulation was also used to investigate the absorption dependence on the thickness of the MoS_2 layer from 2nm to 30nm as shown in Figure 2.8. These simulation results are for the layered structure that includes the top and bottom nanoantenna arrays. Each of the three identified peaks labeled as A, B, and C in Figure 2.8 were also shown as a function of MoS_2 layer thickness in Figure 2.9.

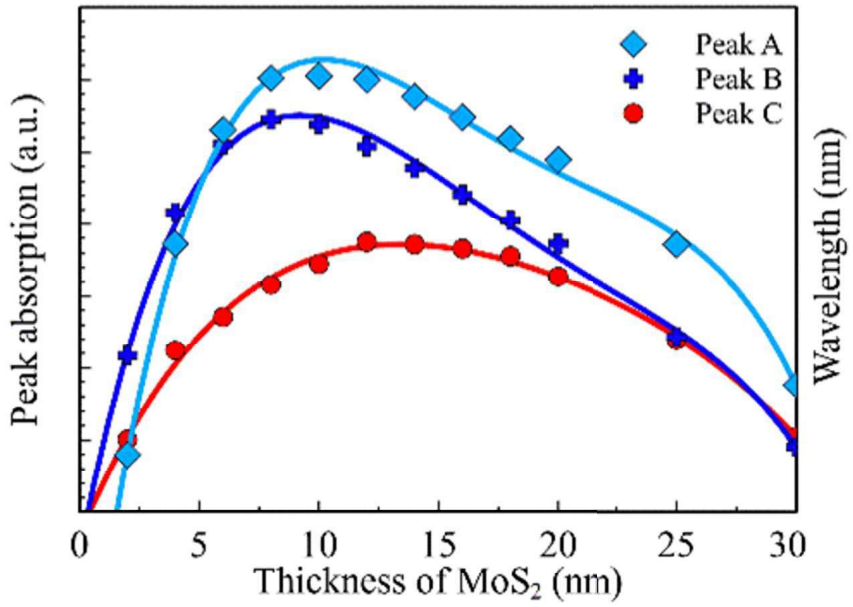

Figure 2.9 Extracted data for peak absorptions.

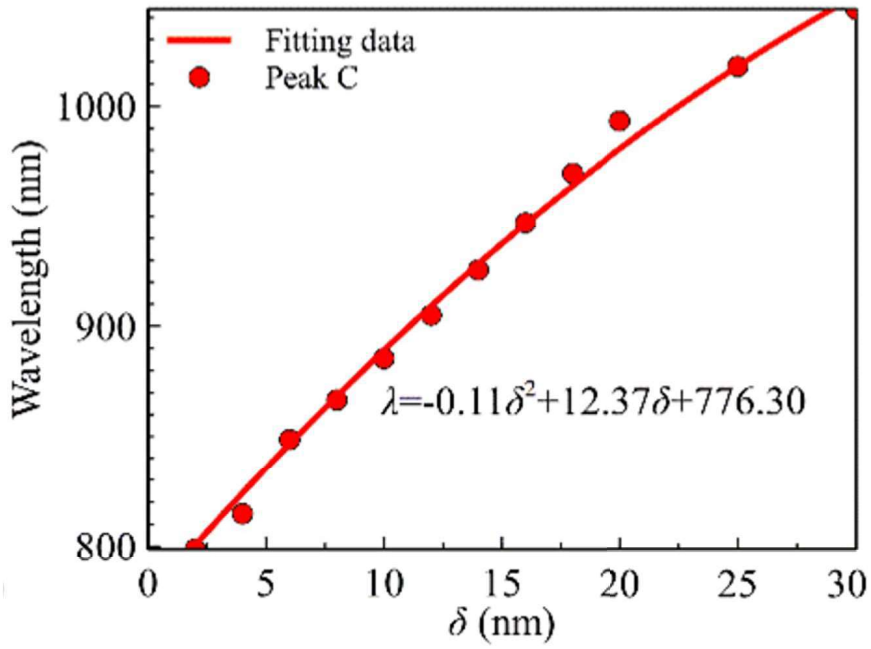

Figure 2.10 Peak C shifting to longer wavelength as MoS_2 thickness increases.

When the semiconductor layer is thin enough, the tunneling effect will happen, where the space between the top and bottom layers is not enough to separate the charge that gives rise to the electric field. When the gap is larger, the electric fields from the SPPs decrease and become less effective. The maximum absorptions are thus located in the middle range of the MoS_2 thicknesses. While peaks A and B maintain the same position, around 7 nm thick, peak C is varying with the incident wavelength and shifts to shorter wavelengths as the MoS_2 layer decreases in thickness. The wavelength of the C peak versus MoS_2 thickness can be fit to a quadratic equation as shown in Figure 2.10.

The FDTD simulations shown in this section support the proposed three-layer structure as an effective method for enhancing the electric fields within the MoS_2 layers caused by surface plasmons in the gold nanoarrays. For the experiments that use an 830 nm wavelength laser, the analysis has shown the highest absorption around 5 nm thickness for the semiconductor.

2.3 Device Fabrication and Characterization

The NAs/MoS_2/NAs layered structure device fabrication, as shown in Figure 2.11(a), was started from a heavily doped p-type silicon substrate ($N_a = 1{\times}10^{16} cm^{-3}$) with 300 nm thick silicon dioxide (SiO_2) dielectric layer. The wafer was carefully cleaned with acetone, isopropyl alcohol (IPA), and followed by 1-minute deionized water (DI) rinse. Similar cleaning steps were carried out multiple times when necessary during the fabrication. Next, external circuits and the biggest set of the alignment mark were patterned by applying the ultraviolet (UV) lithography technique and depositing 60 nm thick gold. External circuits served as contacts and measurement interfaces when testing. By going through electron beam lithography (EBL), metal deposition, and lift-off technique, the bottom layer of the proposed device was fabricated first with 3 nm titanium followed by 22 nm gold. Then, few-layered MoS_2 nanoflakes were mechanically exfoliated and examined under optical microscopy. The criteria to choose the eligible flakes can be concluded as follows: within the desired thickness range and a large uniform working space. Selected MoS_2 was dry transferred [145] onto the bottom nanostructures with a gentle press to ensure no significant air bubbles beneath it. With the limited contact area between the gold nanostructures and the MoS_2

nanoflake, the van der Waals force is relatively low. Hence, internal electrodes were fabricated to press and hold the flake. During this fabrication, two sets of alignment marks were introduced with smaller dimensions as shown in Figure 2.12(a) and Figure 2.12(b), where mark 2 has 1 μm line width and mark 3 has 250 μm line width. By utilizing the alignment marks, EBL enables precise fabrication with step sizes of 200 nm and 5 nm, respectively.

Finally, the top layer nanostructures with 110 nm offset relative to the bottom can be fabricated by using EBL. To achieve the desired resolution multiple focusing steps were used and alignment

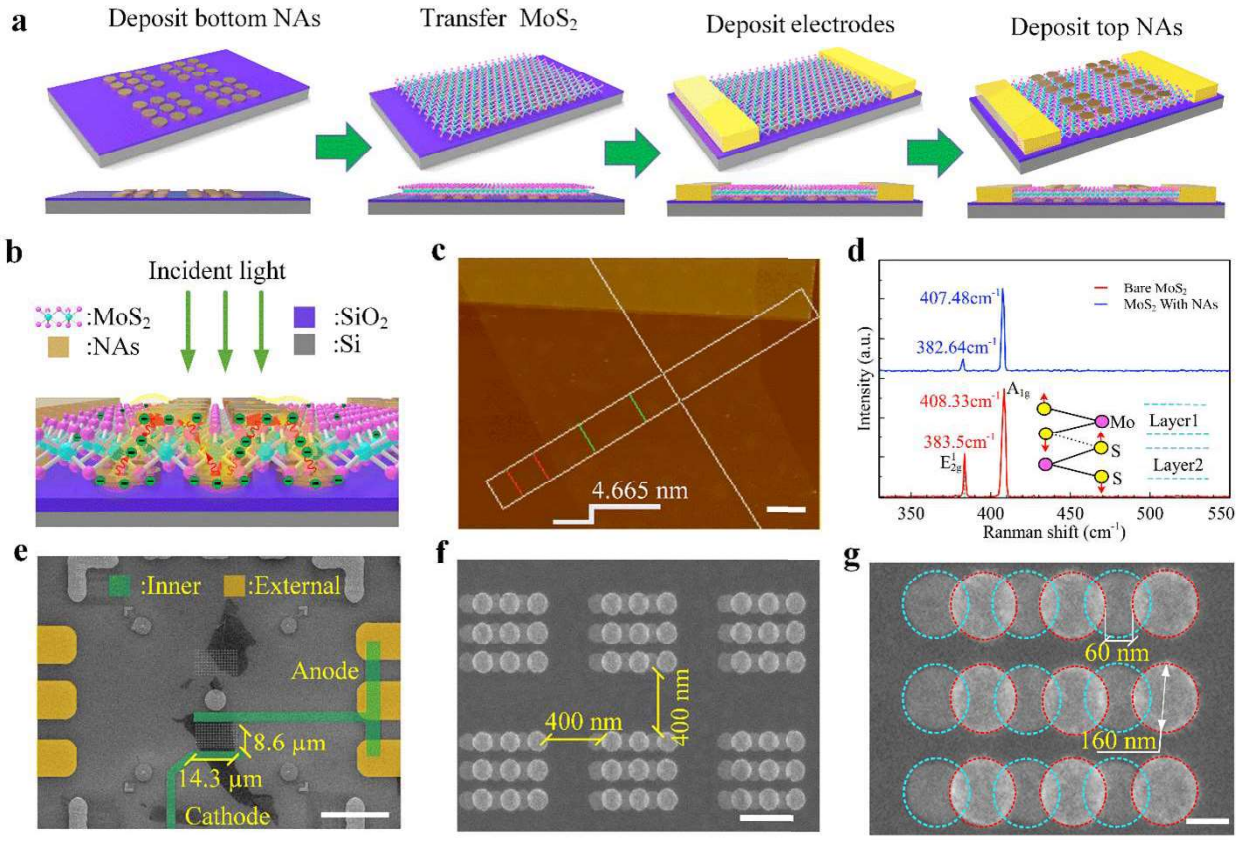

Figure 2.11 Fabrication and characterization of NAs/MoS_2/NAs layered photodetector. (a) Schematic illustration depicting the fabrication process for layered photodetectors. (b) Schematic representation demonstrating the excitation and transformation of energetic electrons generated through plasmon decay. (c) AFM image displaying a representative MoS_2 nanosheet. Scale bar: 2 μm. (d) Raman spectrum showing a representative few-layer MoS_2 nanosheet with and without NAs. (e) SEM image of the NAs/MoS_2/NAs layered photodetector. Scale bar: 20 μm. (f) SEM image showcasing representative NAs/MoS_2/NAs plasmonic nanoantennas on both sides of a few-layer MoS_2 nanosheet. Scale bar: 400 nm. (g) Enlarged SEM image displaying a single plasmonic nanoantenna pattern. The blue dashed circles indicate the bottom layer NAs, while the red dashed circles represent the top layer NAs. Scale bar: 100 nm.

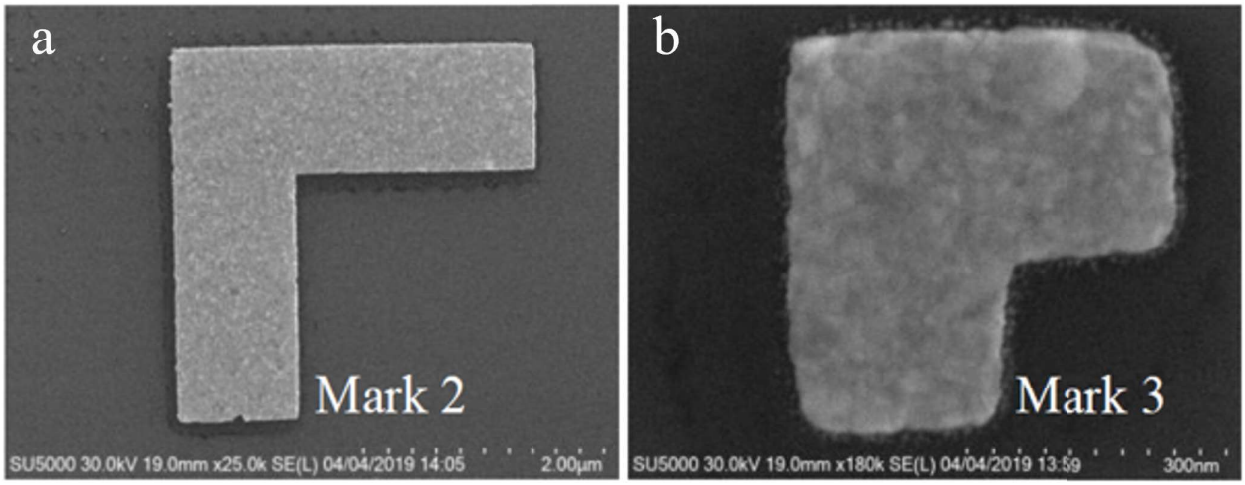

Figure 2.12 Alignment marks with (a) medium dimension and (b) smallest dimension.

marks of various dimensions were used. In the first step, a system window was focused on a 100nm × 100 nm area and then shrinking its size to focus on alignment mark set 2. Alignment with mark 2 can provide a 200 nm step moving size, which means each navigation arrow click on the keyboard will give us a 200 nm shift on the sample stage. However, 200 nm is not accurate enough to produce the desired offset value, 110 nm. Then magnification of the focus window was increased to focus on mark 3, where the final step size was 5 nm. The structure of the final product and corresponding charge transport mechnisms are shown in Figure 2.11(b) and (e). With the alignment marks set to the corners of the working space, we can get the smallest alignment error in the center. In Figure 2.11(b), the introduction of Au NAs on both sides of MoS_2 naturally establishes vertical built-in fields, forming Schottky barriers at the Au-MoS_2 interface. Upon illumination, plasmons are generated in the Au NAs with exponentially decaying fields extending into the MoS_2, generating energetic electron-hole pairs. A fraction of energetic electrons can overcome the Schottky barriers and inject into the conduction band of MoS_2, leading to an extended lifetime of these energetic carriers. The vertical built-in field within the MoS_2 layer prevents the injected electrons from returning to the Au NAs [146], thereby minimizing photocurrent loss and heat generation. In this configuration, the Au NAs function as electron donors, while the middle MoS_2 layer acts as the electron acceptor. Consequently, the detectable photocurrent is no longer limited to incident photon energies above the MoS_2 bandgap but can extend to photon energies above the Schottky

barrier height [147]–[149]. Thus, the proposed sandwich photodetector enables efficient detection of incident light below the MoS_2 bandgap through the LSPR within the vertical gaps.

The atomic force microscopy (AFM) image, Figure 2.11(c), shows the nanoflake is 4.665 nm thick, which is within the expected thickness range. Based on the literature, the thickness for a monolayer MoS_2 is about 0.615 nm [150], therefore we can estimate the one shown in Figure 2.11(c) is about 8 layers. Peak frequencies in the Raman spectrum shown in Figure 2.11(d) also are in good agreement with an 8 layer MoS_2 thickness [151].

With the second layer of the gold nanoarray fabricated on top of the MoS_2, both Raman peaks showed a slight decrease in intensity. This may due to the top layer structure suppressing the vibration of the MoS_2 molecule under it and resulting in a higher interlayer force constant [152]. Since the changes between E^1_{2g} and A_{1g} peaks are negligibly small, the result illustrates that the proposed double-layer nanostructure design generates an imperceptible impact on the original semiconductor material characteristics.

The final device fabricated with the proposed structure has an area of 14.3 μm × 8.6 μm between anode and cathode for photoresponses. The enlarged view of one unit cell of the nanostructures is shown in Figure 2.11(f) and (g). The dimensions are the same as those in FDTD simulation, 110 nm for the lateral displacement of the two layers, 160 nm for nanodisk diameter, 25 nm for nanodisk height. The design left a 60 nm lateral gap, which is much larger than the vertical one. This is intended for minimizing the lateral gap induced plasmonic effect such that the experimental results are dominated by the vertical gap that corresponds to the thickness of the MoS_2.

2.4 Electrical Characterization of MoS_2 Based Photodetectors

The photosensitivity of the MoS_2 photodetectors was measured as described below [153]:

$$S = \frac{\sigma_{LaserOn} - \sigma_{LaserOff}}{\sigma_{LaserOff}} = \frac{R_{LaserOff} - R_{LaserOn}}{R_{LaserOn}} \tag{2.8}$$

where S is the photosensitivity, σ is the photoconductivity, and R is the resistance as measured between the contact pads. The LaserOn and LaserOff subscripts indicate the two laser states. We assume the contact resistance at the measurement pads is independent of incident light and therefore

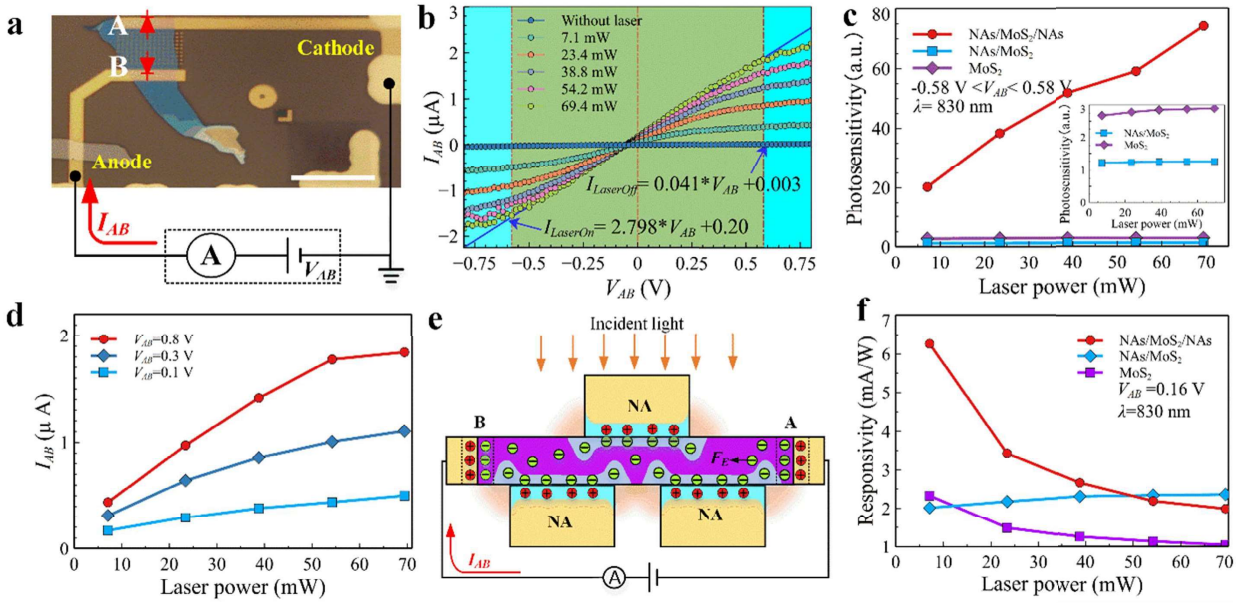

Figure 2.13 Optoelectronic response of the sandwich photodetector under near-infrared (λ=830 nm) laser stimulation. (a) Optical image showing the photodetector and the experimental setup used for measurements. Scale bar: 20 μm. (b) I-V curves of the layered photodetector under different laser stimulation conditions. (c) Photosensitivity plotted as a function of incident laser power under 830 nm laser stimulation. (d) Photocurrent displayed as a function of incident laser power for the sandwiched photodetector under various applied potential biases. (e) Electric circuit model illustrating the configuration of the sandwich photodetector. (f) Responsivity depicted as a function of incident laser power under V_{AB} = 0.16 V and λ=830 nm.

S only depends on the resistance change in the channel because the contact resistance will cancel from numerator and denominator in equation 2.8.

In our setup, a semiconductor parameter analyzer (Agilent 4156C) was connected to the two electrodes of the devices and a power-adjustable 831.1 nm laser was used to illuminate the sample, as in Figure 2.13(a). Current versus voltage (I-V) curves were obtained in Figure 2.13(b). With the increasing laser power, the photocurrent (I) increases due to a large number of electron-hole pairs excited. When increasing the applied bias voltage (V_{AB}), photocurrents raise almost linearly in the low bias region, shaded with a green background for the 69.4 mW case, and exhibit a deviation from Ohmic behavior at the high bias region, shaded with a blue background.

Linear fitting lines to the I-V responses for the currents with 69.4 mW illumination and with laser turned off are as follows: $I_{LaserOff} = 0.041V_{AB} + 0.003$ (μA) and $I_{LaserOn} = 2.798V_{AB} + 0.2$ (μA), where I represents the photocurrent obtained from the device and V_{AB} is the applied

bias voltage. From the fitting lines, we can get parameters $R_{\text{LaserOff}} = 1/0.041$ MΩ ≈ 24.39 MΩ, $R_{\text{LaserOn}} = 1/2.798$ MΩ ≈ 0.36MΩ, and from equation 2.8, the photosensitivity $S = 67.24$. Similarly, the photosensitivity under 7.1 mW, 23.4 mW, 38.3 mW, and 54.2 mW laser illuminations was found to be 20.24, 38.31, 51.55, and 58.82 respectively. For a detailed understanding, MoS_2 and NAs/MoS_2 devices are fabricated and corresponding photosensitivities plotted together as shown in Figure 2.13(c) for comparison. The inserted image shows the maximum photosensitivity is 2.90 for the MoS_2 device and 1.25 for the NAs/MoS_2 device. With the NAs/MoS_2/NAs structure, strong confinement of the light by surface plasmons to the small vertical gaps between upper nanoarrays and the lower nanoarrays significantly increases the photosensitivity. Both LSPR and SPPs will enhance the electron-hole pair generation in the semiconductor and reduce the measured resistance. For the NAs/MoS_2 structure, there is a decrease in the photosensitivity compared to the MoS_2 alone (no nanoarrays of gold). We interpret this as a comparison group that can help us exclude the doubt that lateral gaps may contribute to the enhancement as well. With 60 nm gap structures on top, the photosensitivity of the NAs/MoS_2 structure is much smaller than for the MoS_2 device. From this we conclude that the large lateral distance cannot efficiently excite the plasmonic effect and 160 nm diameter Au structures can be seen as light blockers, which prevented normal MoS_2 light absorption. Both resulted in fewer electrons being excited into the conduction band, thus the photosensitivity is even lower than the MoS_2 device as in the figure 2.13(f).

Figure 2.13(d) presents the investigation of the photocurrent as a function of laser power under various V_{AB} conditions. Within the effective voltage range, the photocurrents exhibit a more or less linear increase with the illuminated laser power for $V_{\text{AB}} = 0.1$ V and 0.3 V. However, when V_{AB} is increased to 0.8 V, the photocurrent levels off under high laser power. This behavior can be explained by drawing an analogy with the working principle of a light-dependent resistor (LDR). The electric circuit model of the photodetector is depicted in Figure 2.13(e). The vertical built-in field at the Au-MoS_2 interfaces facilitates the efficient separation of energetic carriers generated from plasmon decay and reduces carrier recombination rates. This leads to a significant reduction in the resistance of the MoS_2 layer. However, the injection of energetic electrons from Au to

the MoS_2 nanosheet is limited. As a result, a saturation mode is observed as the voltage bias increases. Therefore, it is crucial to select an appropriate laser power and V_{AB} to achieve a high net photocurrent while minimizing power consumption. In our study, we found that a bias voltage of 0.58 V combined with a laser power of 69.4 mW represents an optimized condition (Figure 2.13(b)).

Figure 2.13(f) compares the responsivity of the MoS_2, NAs/MoS_2, and NAs/MoS_2/NAs structures at a fixed bias of V_{AB} = 0.16 V within the linear range. Photoresponsivity in the figure can be defined as $R_{es} = I_{ph}/P_{in}$, where both I_{ph} and P_{in} are normalized over the nanostructures' covered area and the power of the laser used in the experiment was carefully measured with a PM100D energy meter. When increasing the laser power, only the responsivity for NA/MoS_2 case maintain stable while the other two cases drop significantly. As mentioned earlier, there is a saturation of available electron-hole pairs that can be excited. By comparing, one can find that the maximum responsivity is 6.26 mA/W for the NAs/MoS_2/NAs device, 2.02 mA/W for the NAs/MoS_2 device, and 2.33 mA/W for the bare MoS_2 device. Therefore, a low incident laser power is the ideal working condition to maintain high responsivity for the proposed sandwiched device at the near-infrared range and a 0.16 V bias.

2.5 Nonlinear Optical Absorption

The NAs/MoS_2/NAs layout proposed in this research contains complex metal structures, which can induce strong nonlinear optical effects. Therefore, the structure provides a good opportunity to investigate the phenomenon. In the experiment, the impact of the layered nanostructure on nonlinear absorption was probed through a hyperspectral stimulated Raman scattering imaging system [27]. A schematic diagram of the system can be found in Figure 2.14. In this system, an ultrafast dual output broadband laser source [46] was used for photon excitation with 80 MHz pulse frequency. Both output lasers used had Gaussian beam profiles and were chirped into 1.5 ps pulses by going through the SF57 nanorods, a pulse stretcher. To match the simulation and experiments, a 840 nm laser served as the probe laser (shown as the blue line in Figure 2.14) and transmitted through a delay stage to adjust the beam arrival time. A second laser centered at 1040 nm was

used as the pump laser (show as the red line in Figure 2.14). The pump laser was transmitted through an electro-optical modulator (EOM) and modulated to 20 MHz. The two beams were then combined and directed to an inverted laser-scanning microscope (Olympus IX83, with Fluoview 1200 scanning-head) with a water immersion objective lens (Olympus UPLSAPO 60X/IR) to focus on the sample. The transmitted beam was then filtered by a Chroma short-pass filter (ET890/220m SPF) to eliminate the 20 MHz 1040 nm pump beam. A photodiode with a lock-in amplifier was placed at the end of the system to detect the output signal. By varying the delay stage, the relative time between the two pulses was adjusted as in Figure 2.15. The time difference, Δt, between pulses corresponds to the x-axis in Figure 2.16(d) and 2.16(f). For each captured video frame, the system can derive three-dimensional images, which correspond to the variation of the 840 nm photon absorption of the device. The hsSRS system results help to understand the effect of a complex metal nanostructure on two-color two-photon absorption (2PA) since two beams were illuminating the sample with different wavelengths and higher-order nonlinear effects are generally small comparing the 2PA.

Note that, for effective utilization of the hsSRS imaging system, it is essential to fabricate the devices on transparent substrates such as glass. However, the presence of glass substrates can pose

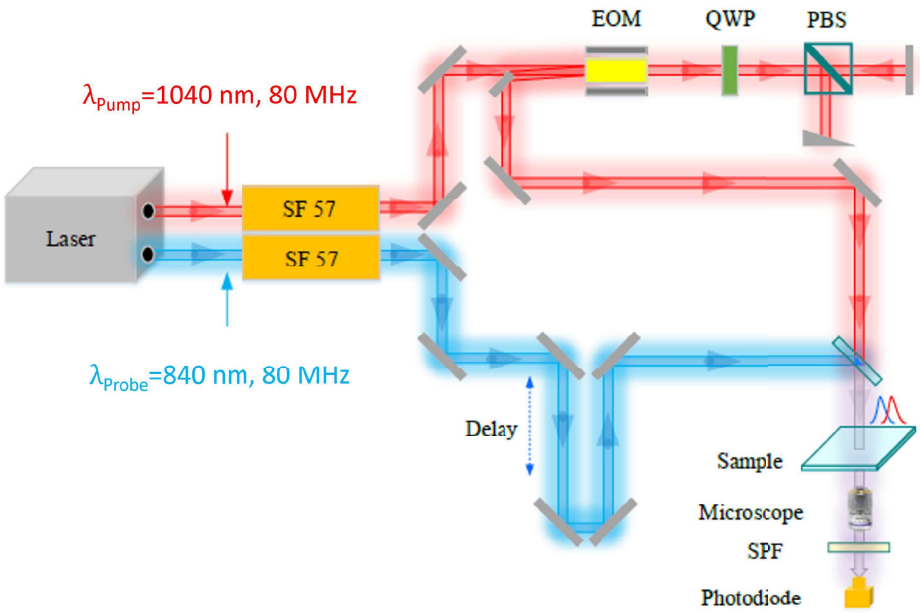

Figure 2.14 hsSRS imaging system setup.

notable challenges concerning charge accumulation in the samples during e-beam lithography. To address this issue, a conducting layer of a 10 nm thick Al film was carefully deposited onto the substrate. After completing the e-beam processing, the aluminum was removed using chemical etching before resist developing. The hsSRS imaging results for bare MoS_2, NAs/MoS_2, and NAs/MoS_2/NAs structures can be found for various beam separation times, Δt, in Figure 2.16. The region bounded by dashed lines in Figure 2.16(a) for bare MoS_2, NAs/MoS_2, and NAs/MoS_2/NAs have uniform thickness and are used for comparison. Figure 2.16(c) and (e) represent the distribution of 840 nm light absorption when the 1040 nm pump comes in first and the probe beam arrives with a 3.3ps and 33.3 ps delay, respectively.

The substrate, which shows little response to 2PA, is displayed as green color, and the relative absorption intensity scale bars are shown to the right of the images in Figure 2.16(c) and Figure 2.16(e). A 3D plot of Figure 2.16(c) is shown in Figure 2.16(b), the triangle-shaped area with the highest intensity marks the double-layered structure performance. Overall, these figures show the NAs/MoS_2/NAs region exhibits the strongest 2PA absorption followed by the NAs/MoS_2 region

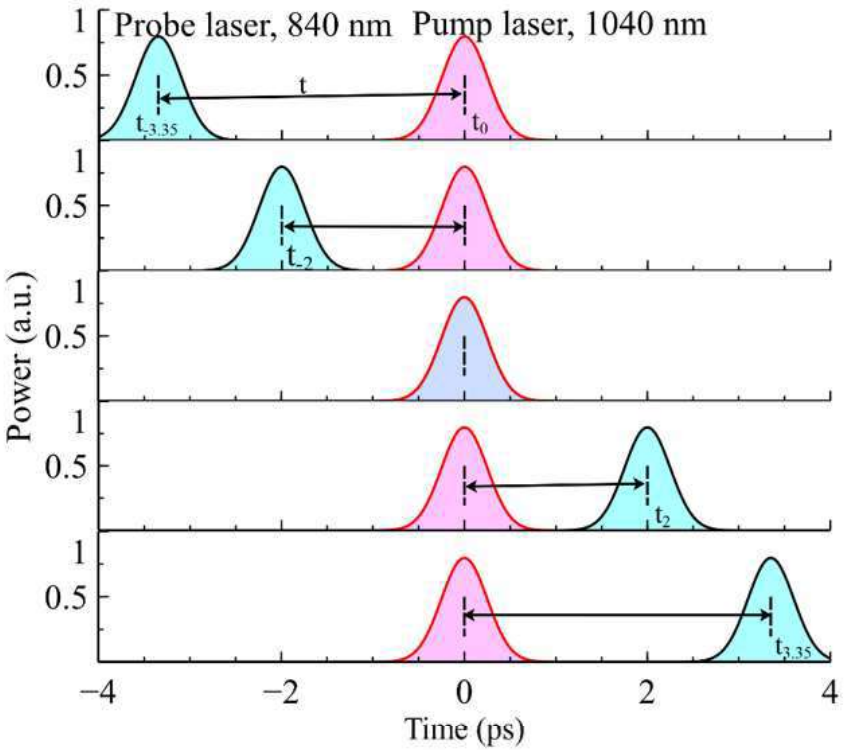

Figure 2.15 Time sequence of the probe and pump laser.

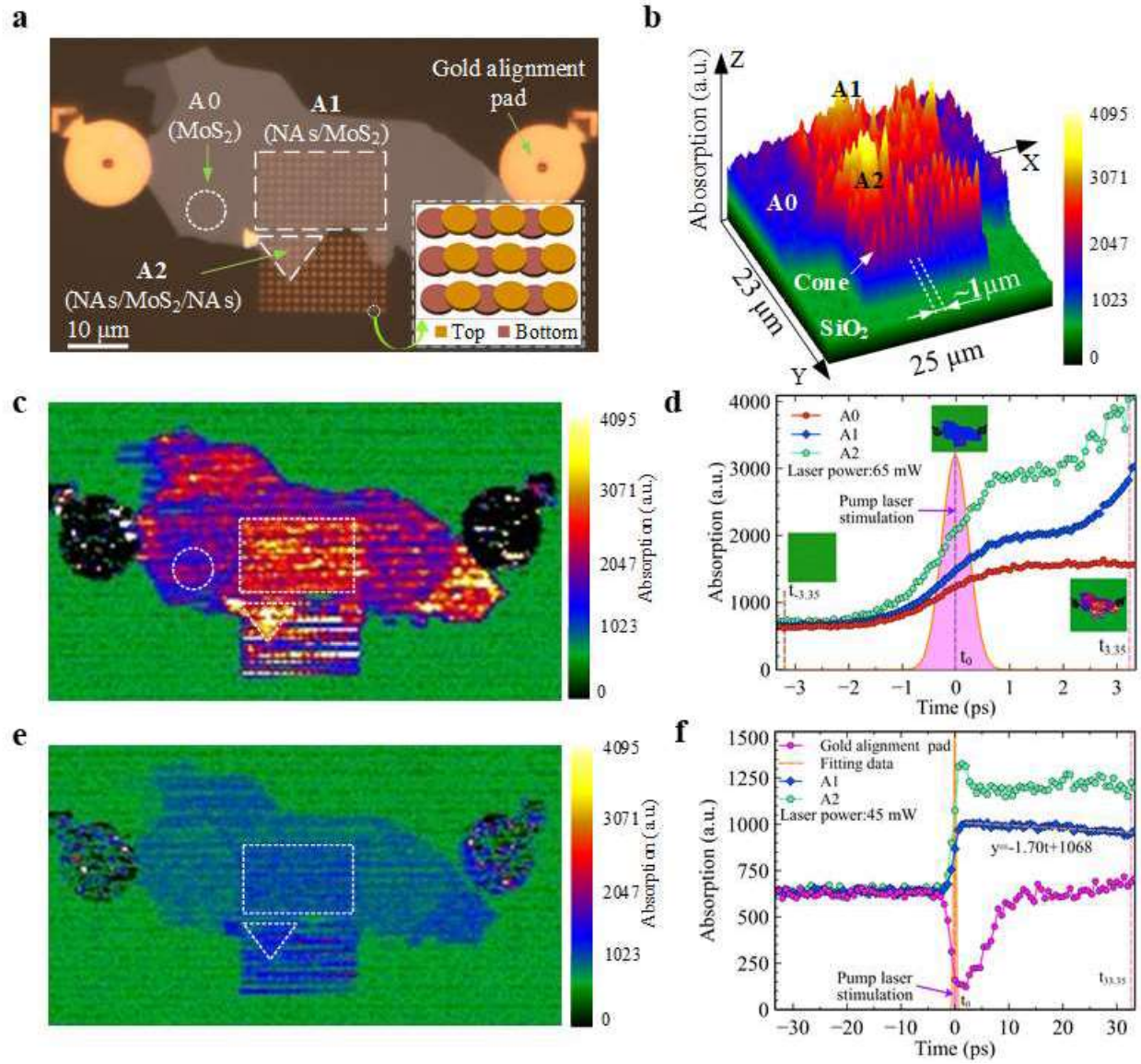

Figure 2.16 Transient photoresponse and a comparison of light absorption between MoS_2, NAs/MoS_2, and $NAs/MoS_2/NAs$ nanostructures using an hsSRS imaging system. (a) Optical image of a representative MoS_2 device, with an insert image highlighting the layered NAs without MoS_2. (b) A 3D surface plot demonstrates the distribution of 840 nm photon absorption under 65 mW laser stimulation. (c) The absorption distribution of 840 nm photons after 3.35 ps of 1040 nm photon stimulation. Here, the total power of incident 840 nm and 1040 nm photons is 65 mW. (d) Extracted absorption data for different sections in panel (c), representing averaged values of the corresponding sections. (e) The distribution of 840 nm photon absorption after 33.35 ps of 1040 nm photon stimulation is displayed, with the laser power lowered to 47 mW for enhanced contrast. (f) The extracted absorption data for the relevant sections in panel (e).

and bare MoS_2 region. Although 2PA is an intrinsically spatially resolved phenomenon, it can be influenced by the amplitude of the local field [154]. This is in good agreement with a strong local field in the layered structure shown in the FDTD simulations previously.

Figure 2.16(c) illustrates the change in 840 nm photon absorption in different regions (A0, A1, and A2) before and after the arrival of the 1040 nm beam. Initially, the amplitude reflects the excitation of the probe laser (840 nm) with an energy of 1.476 eV, which falls short of direct excitation across the MoS_2 bandgap (E_g=1.88 eV). Although the double-layered area exhibits slightly higher response amplitude, the difference is not substantial. Subsequently, the pump laser (1040 nm) enters with a pulse duration of approximately 1.5 ps, causing the curves in Figure 2.16(d) and Figure 2.16(f) to rise due to the excitation induced by two-photon absorption (2PA). As the plot solely depicts the variation in 840 nm photon absorption, it can be concluded that the pump beam assists in the absorption of 840 nm photons during this process. The A2 layered structure area exhibits around 1.5 times higher absorption compared to the A1 single-layer nanostructure area, and the absorption continues to increase with longer pulse gaps. These changes in absorption solely result from the introduction of a single laser pulse (1040 nm) preceding the 840 nm probe light. By extending the Δt values, a peak in 840 nm absorption is expected to be achieved.

In order to conduct further investigations, an incident laser energy of 45 mW was employed, and Δt was increased to 33.3 ps, as depicted in Figure 2.16(e) and Figure 2.16(f). For the NAs/MoS_2/NAs nanostructure, the highest relative absorption rate reached 1327.06 a.u, whereas for the NAs/MoS_2 structure, it was 1008.79 a.u, indicating a 1.3-fold increase in absorption for the double-layered design. In the A1 region, the measured results exhibit a decay process after a short time due to the natural relaxation of electron-hole pairs. However, this decay process occurs on a significantly longer timescale compared to the pump laser exposure time of approximately 1.5 ps, aligning well with previous findings [155], [156]. Conversely, absorption in the NAs/MoS_2/NAs region remains relatively stable even at longer Δt values. Additionally, Figure 2.16(f) illustrates the absorption in the gold alignment pad region, allowing for a comparison between locations where the gold is nanostructured and where it forms a continuous film. The sudden decrease in absorption

observed in the gold alignment pad area can be attributed to a rapid increase in the thermoreflectance of the gold material, which occurs when the thermal equilibrium of the gold is disrupted [157]. During the period of thermal non-equilibrium, most photons (including both 840 nm and 1040 nm wavelengths) are reflected from the solid gold, resulting in a decline in the absorption curve. As the system reaches thermal relaxation, thermoreflectance returns to its original value, enabling more photons to transmit through the sample and be detected by the photodiode. This phenomenon also suggests that the overall two-photon absorption (2PA) can be further enhanced by carefully selecting the composition of materials for the nanostructures.

The experimental findings obtained through hsSRS reveal that the NAs/MoS_2/NAs structure exhibits remarkable nonlinear optical properties, primarily attributed to the confinement of incident photon energy within surface plasmons. The pronounced two-photon absorption behavior observed underscores the promising potential of these double-layered structures in a wide range of applications, including near-infrared detection, energy harvesting, spectroscopy for investigating two-photon absorption in organic materials, and various other fields of research.

CHAPTER 3

SILICON CARBIDE SYNTHESIS WITH THE SELECTIVE LASER DEPOSITION TECHNIQUE AND ITS CHARACTERIZATION

3.1 Current Selective Laser Fabrication Method

Selective area pulsed laser deposition (PLD) techniques have emerged as another method for the synthesis of silicon carbide thin films. SiC thin films find applications in a wide range of fields, including electronics, optoelectronics, and high-temperature devices. This section provides an explanation of the current selective area pulsed laser deposition technique for SiC thin film synthesis.

Nowadays, low-cost transitions from existing silicon based integrated circuit to silicon-silicon carbide (Si-SiC) hybrid systems have unique applications [158], such as the integration of high-power microwave devices with digital circuits. The high carrier velocity, large critical breakdown electrical field, and high temperature tolerance are of high interest for advancing device capabilities [159]. Thus, wide bandgap semiconductors such as silicon carbide (SiC) and gallium nitride (GaN) have gained increasing interest due to their ability to manage high power density [160]. Among them, SiC can be grown directly on Si substrates with smooth integration between signal processing digital circuits and radio frequency (RF) devices [161], making it one of the best candidates for future high-power, high-frequency systems.

In the past, significant efforts have been devoted to developing SiC by direct synthesis techniques on Si substrates for monolithic microwave integrated circuits (MMICs), including chemical vapor deposition, sputtering, rapid thermal annealing, and furnace annealing [162]. However, none of them can avoid heating the entire wafer with a long procedure time during the fabrication processes. Unexpected dopants, such as carbon, can easily diffuse into the sample and affect the device performance across the whole wafer, and pre-fabricated silicon devices on the substrate would suffer from dopant diffusion under such high-temperature processing steps.

To overcome these difficulties, a selective area fabrication technique was carried out using a high-power KrF excimer laser [163]. The method not only demonstrates promising results for the

local laser-fabricated Si-SiC device for microwave circuit applications but also shows advantages in reducing processing complexities. The precise control of the laser creates an opportunity for fast and limited area heating in the millimeter range, which reduces adverse impacts on neighboring devices. Operating under ambient environment further justifies its simple and practical advantages.

In order to conduct comprehensive testing, SiC thin films are commonly deposited onto Si substrates to assess their electrical properties. To fabricate such films, a single-sided polished p-type Si wafer serves as the foundation. Thorough cleaning procedures are undertaken to ensure the removal of any oxide layers. Subsequently, a commercially available polymethyl methacrylate (PMMA) layer was spun onto the wafer at a speed of 3000 rpm. This process results in the formation of a PMMA thickness (t) ranging from approximately 1200 to 1300 Å. The inclusion of PMMA in this procedure serves as a solid source of carbon atoms. Next, a high-power KrF excimer laser pulse is focused onto the wafer, operating at a wavelength of 248 nm. As a result, the irradiated PMMA and Si substrates undergo simultaneous dissociation and melting. Through subsequent recrystallization, a thin layer of SiC material is formed atop the Si substrate. To establish reliable electrical contacts, aluminum (Al) is deposited and patterned onto the Si-SiC devices. For ensuring strong adhesion and Ohmic contact to achieve high performance electronic devices, metals such as chromium (Cr) thin film is preliminarily deposited onto the SiC layer.

3.2 COMSOL Simulation

The heat transfer induced by selective laser fabrication can be simulated and analyzed using the COMSOL Multiphysics software [164]. The built-in heat transfer module is a great tool for heat analysis in a variety of physical processes where the laser process is included.

The geometry model for the COMSOL simulation is built based on the actual experiments as in Figure 3.1. To reduce the simulation time, a thick layer of PMMA only covered a small area of the 1-inch Si wafer, where the PMMA layer is large enough to enclose the entire laser-affected area. The wafer thickness is set to be 275 μm as commercially available products, which is thick enough to cover the heat transfer area. The maximum mesh sizes in the PMMA layer and Si wafer are set to be 0.25 μm and 3.4 mm respectively, where the minimum mesh size in the Si wafer is 15.2 μm

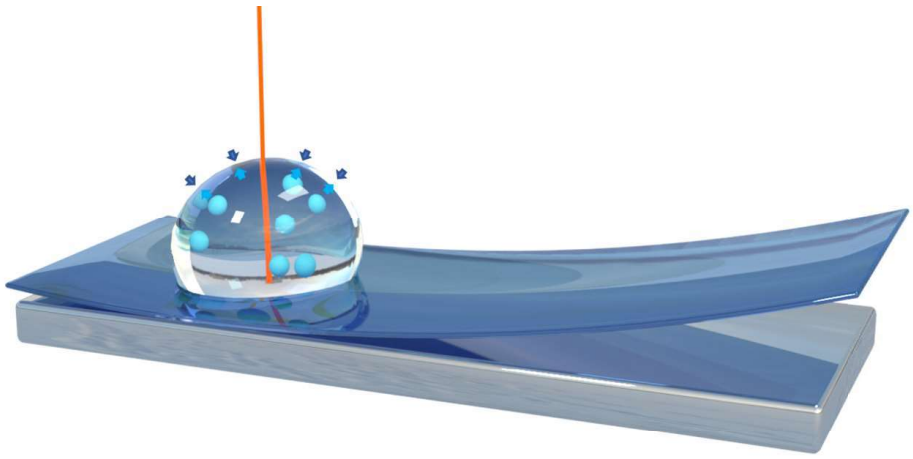

Figure 3.1 Laser fabrication illustration.

to achieve a geometry-independent solution. The resolution of time is set as 5 μs for the simulation efficiency. The primary object of this simulation is to estimate the single-laser pulse-induced heat transfer and to predict the heat distribution profile shortly after the laser pulse.

The temperature in the sample varies due to the absorption of the laser and the cooling mechanisms. Therefore, this COMSOL integrated computational model is associated with four basic

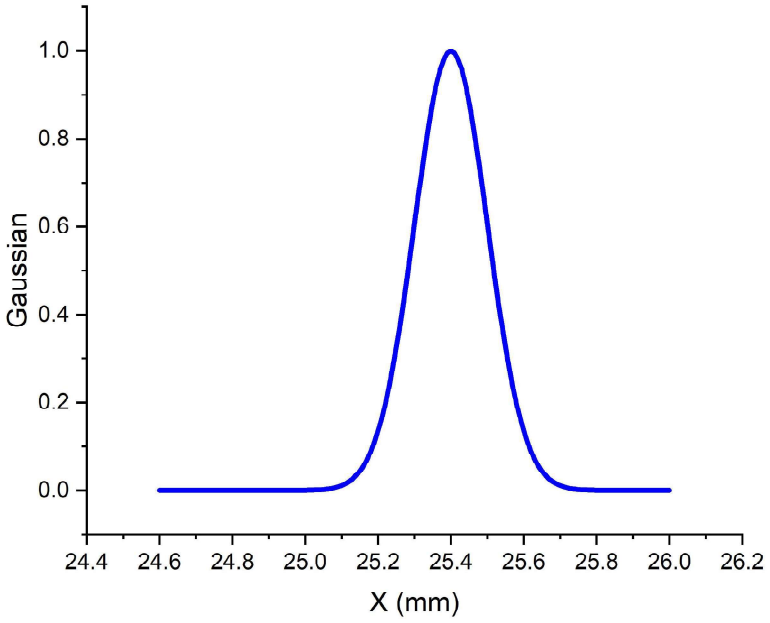

Figure 3.2 Laser energy Gaussian profile at the center of the wafer (X=25.4 mm).

physical phenomena to express the heat exchange. The first one is the simulation of a single-pulse laser, which is the source of heat. When a high-intensity laser with pulse width P_w = 25 ns hits the target, heat can rapidly be delivered to the material. In the simulation, a 320 mJ laser pulse with a 300 μm beam diameter and 25 ns pulse width, which are comparable to the practical experiment factors, is vertically introduced on top of the targeting surface. Laser-induced heat follows a Gaussian profile, as in Figure 3.2. The high-temperature results in material melting and vaporization, which take away some of the heat. In our experiment, the PMMA layer only has several hundred nm for thickness. Therefore, we assume that the loss of heat as a result of the melting or vaporization

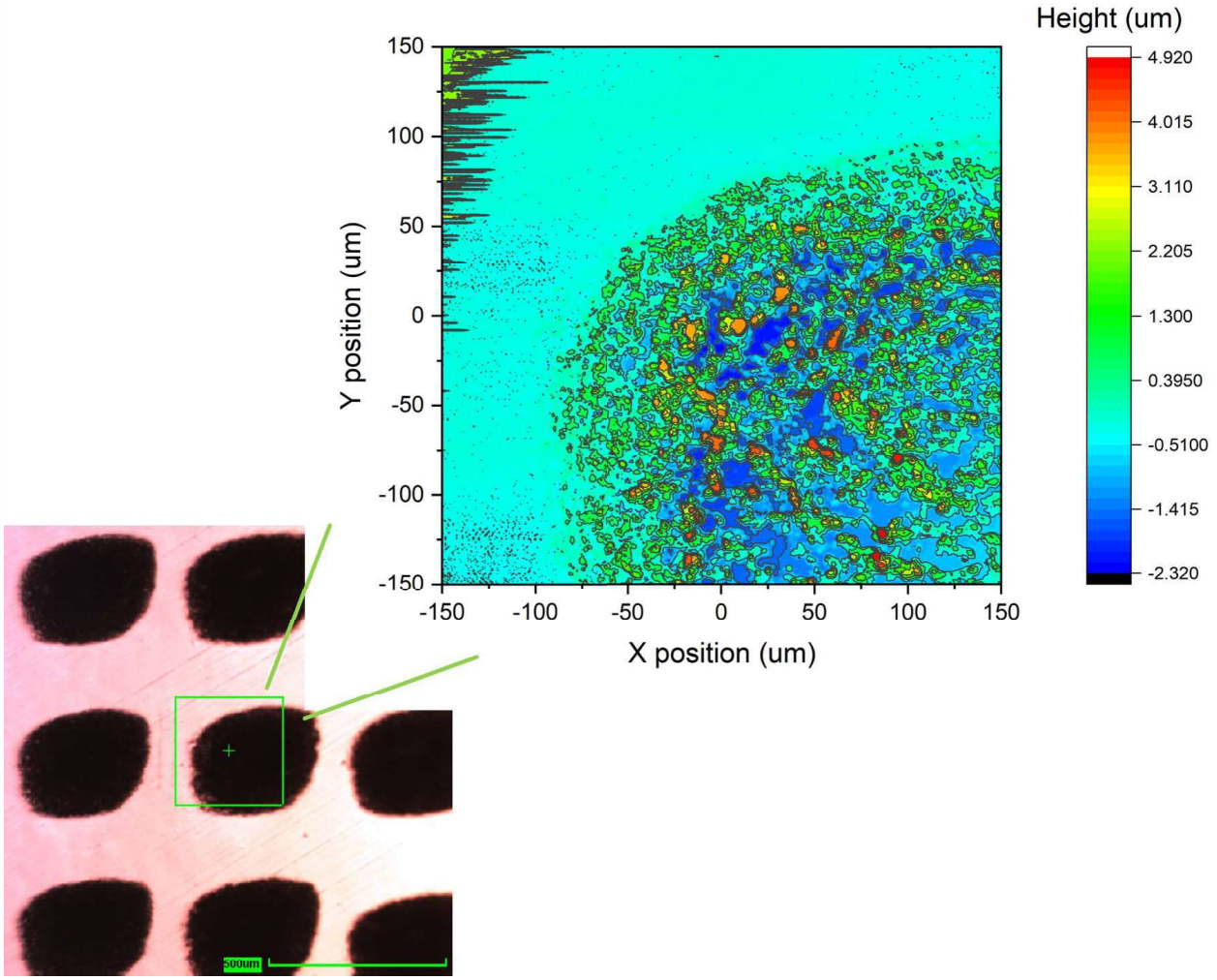

Figure 3.3 Post-laser process nanoscan result. The lower left picture shows the optical view of the laser processed dimples and the nanoscanned area is labeled by the green box. Upper right picture illustrates the nanoscan result, where the laser processed area is distinguished from the un-processed area. The scale bar in the lower left picture is 500 μm.

Name	Value	Description
Tm	1687 K	Si melting temperature
Tv	2628.2 K	Si vaporization temperature
C_p1	700 J/(kg·K)	Si Heat capacity at constant pressure
$\rho 1$	2329 kg/m^3	Si density
$k_{iso}1$	130 W/(m·K)	Si thermal conductivity
ϵ	0.8	Si surface emissivity
R	0.59×(T<Tm)+0.6 5×(T≥Tm)	Si reflectivity
Ta	293.15 K	ambient temperature
h1	30 W/m^2 K	wafer to air Heat transfer coefficient
A1	0.8	wafer Absorptivity [165]
Ep	320 mJ	laser pulse energy
Pw	25 ns	pulse width
D	300 μm	beam diameter
xr	0.0254 m	center location of the laser beam
xd	100 μm	the standard deviation of the Gaussian laser beam
Ed	Ep/(Pw×π/4×D^2) W/m^2	laser average energy density
G	exp(-((x-xr)^2/(2·xd^2)))	laser Gaussian distribution
Pg	A1×Ed×G W/m^2	heat source
W	179 nm	PMMA thickness [166]

Table 3.1 Key parameters used in the COMSOL simulation

of PMMA is not significant to the overall temperature distribution.

In contrast, the wafer-air convection cooling and the wafer surface-air natural radiation are the two main channels for heat relaxations. It is defined that the top surface and the two sides of the simulated wafer are the active areas for both mechanisms since they are exposed to the air directly. The fourth is the visible deformation or melting of the wafer as a result of the heat introduced. It is considered a channel for heat relaxation. A nanoscan result well illustrates the need to include the wafer melting effect, Figure 3.3, where the laser-affected area has a significant rough surface compared to the unprocessed areas. The COMSOL model is designed to consider heat flux transfer during the formation of this region.

Key parameters are concluded as in the following table:

The simulation result concerns the time-dependent variation of the material temperature. According to COMSOL, the heat transfer in a thin structure can be approximated and described by

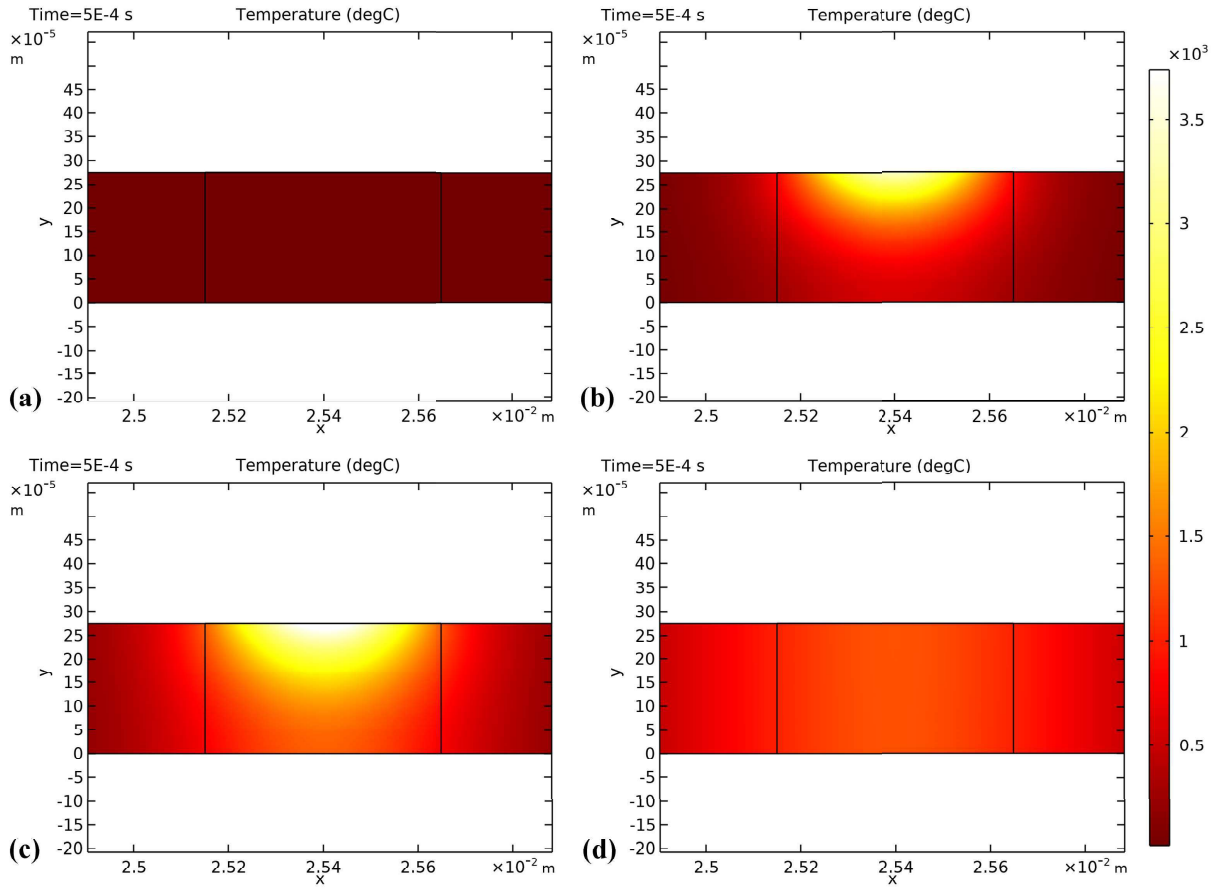

Figure 3.4 Time-dependent COMSOL temperature simulation result of the Si wafer at 320 mJ laser energy setting. The scale bar has a unit in Celsius. (a) Temperature profile of the Si wafer at T = 0 s. The wafer has the same temperature as the ambient environment. (b) Temperature profile of the Si wafer at T = 250 μs, where the heat flux is concentrated near the surface of the structure. (c) Temperature profile of Si wafer at T = 500 μs. The temperature reaches its maximum value at this time then starts cooling. (d) Temperature profile of the Si wafer at T = 1 ms, where the heat is dissipated and the temperature drops toward its initial value.

the following governing equation:

$$\rho C_p \frac{\partial T_s}{\partial t} + \nabla q_s = Q_s \tag{3.1}$$

$$q_s = -k\nabla T \tag{3.2}$$

where ρ is the density of the thin material, C_p specific heat capacity, T material temperature, t time, and k thermal conductivity. Q_s is the heat source applied.

At a 320 mJ laser energy setting, the COMSOL temperature simulation result was obtained in Figure 3.4 at four different time intervals. In Figure 3.4(a), the temperature of the body equals

the ambient environment temperature, 293.15 K. Figure 3.4(b) shows the temperature profile of the wafer at T = 250 μs after triggering the laser heating, where the temperature grows rapidly at the near surface area. With sudden heat introduced ($\geq$ 3500 °C), the PMMA covering material decomposes into gas molecules and forms a plasma cloud. The cloud then explodes and is pushed back, whereas its inner pressure decreases. During this process, carbon atoms diffuse into Si crystal lattice and form SiC eventually. At T = 500 μs, the surface temperature of the wafer reaches its highest value, 6300 °C by the simulation, Figure 3.4(c). For those area whose temperature is higher than Tm will be melted. The melting phenomenon is the sign that indicates the braking of the chemical bond between Si atoms. In Figure 3.4(d), during the energy dissipation process, some of the Si dangling bonds will receive carbon atoms from disassociated PMMA material and form SiC. Others will ideally return to solid Si. Based on similar principles, this selective laser fabrication process can also be applied in applications, such as the selective laser doping [167]–[171], and laser annealing with lower input energy [172], [173].

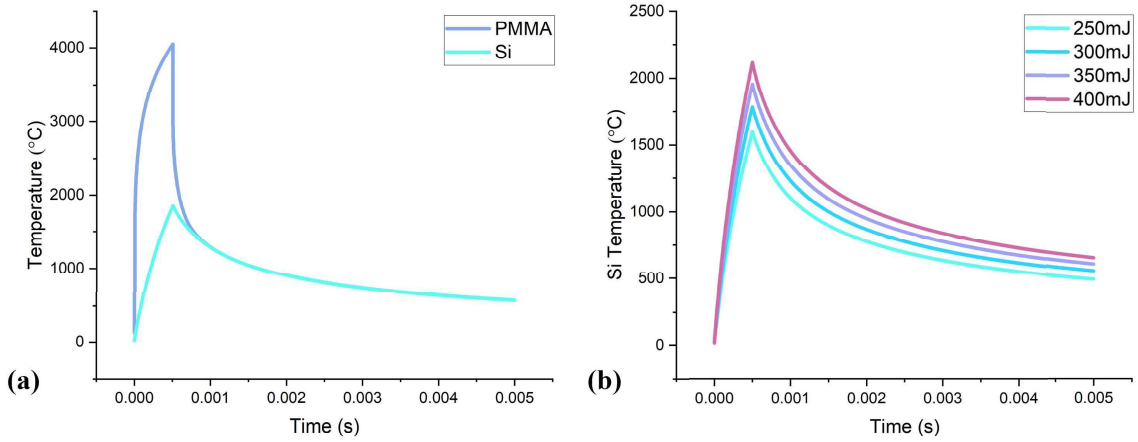

Figure 3.5 Simulated material temperatures with a 5 μs resolution in time. All data were acquired by averaging the temperatures inside the center box of Figure 3.4. (a) Time-dependent temperature variations in PMMA and Si due to the introduced 320 mJ laser. The maximum temperature in Si is lower than that in PMMA. (b) Time-dependent temperatures in Si with laser input energies of 250 to 400 mJ. The higher the energy, there will be aggressive changes in the material temperature.

Figure 3.5 demonstrates the results of the domain-averaged time-dependent temperature simulation of the sample. In Figure 3.5(a), temperature fluctuations are compared between the PMMMA

covering and the Si wafer, where we can see the heat in Si is conducted slower than in PMMA and the maximum temperature is lower as well. With over 4000 °C, it is reasonable to expect PMMA to vaporize. This is also confirmed during the actual experiments. On the other hand, considering the time period that the Si material is above its melting point, the intense change in Figure 3.3 can be explained. Figure 3.5(b) is the parallel comparison of the averaged Si temperature with different laser power settings. From 250 to 400 mJ, higher resulting temperatures can be obtained. This result will be used as a reference to guide the practical experiments since the actual settings are nominally the same as the COMSOL simulations.

In addition, with more heat introduced to the sample, the affected area will be expanded as shown in Figure 3.6. The induced dimples into the silicon are expected to be larger than the laser spot size. The phenomenon must be considered when applying the selective laser fabrication method onto a high density integrated circuit board in order to avoid any potential damage to surrounding circuitry.

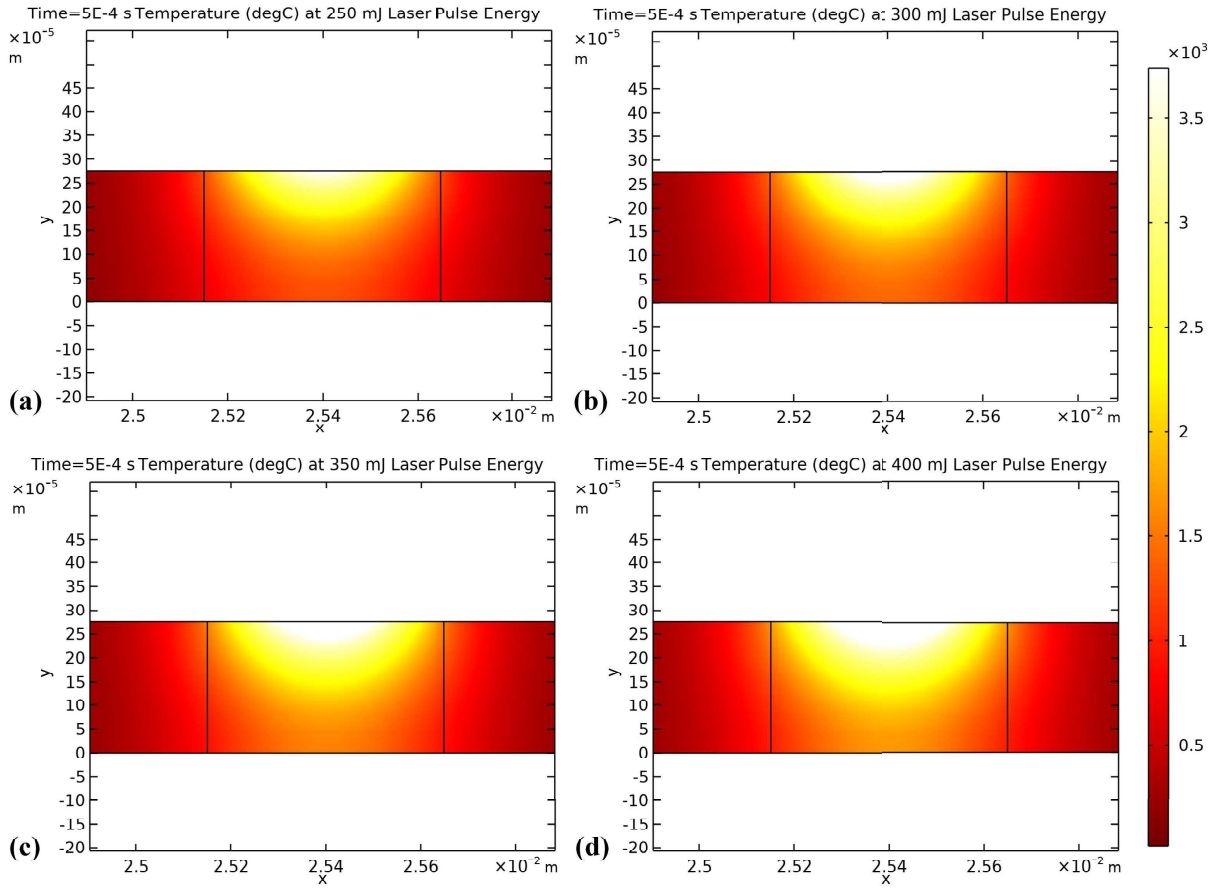

Figure 3.6 Results of the time-dependent COMSOL temperature simulation of Si/PMMA sample with different laser pulse energy at T = 500 μ. Figures (a)-(d) are the heat flux resulting temperature profile with 250 mJ, 300 mJ, 350 mJ, and 400 mJ laser input energies, respectively. It is clear to identify that the laser-influenced area changes at the same time.

3.3 Raman Examination

In addition to the numerous types of elastic scattering of light during the light-matter interactions, a small amount of light will be scattered inelasticly corresponding to different photons of different frequencies from the incident ligth which carry useful chemical structure information [174]. After many years of development, Raman spectroscopy has become a distinguished analysis technique for material characterisation. This is not only limited to chemical identifications but also expanded to investigate the properties of 2D materials as in the previous chapters in this dissertation [175]–[178].

In this section, the processed wafers are explored by Raman spectroscopy. All evaluations are performed in an ambient environment with back scattering geometry and a 532 nm excitation laser.

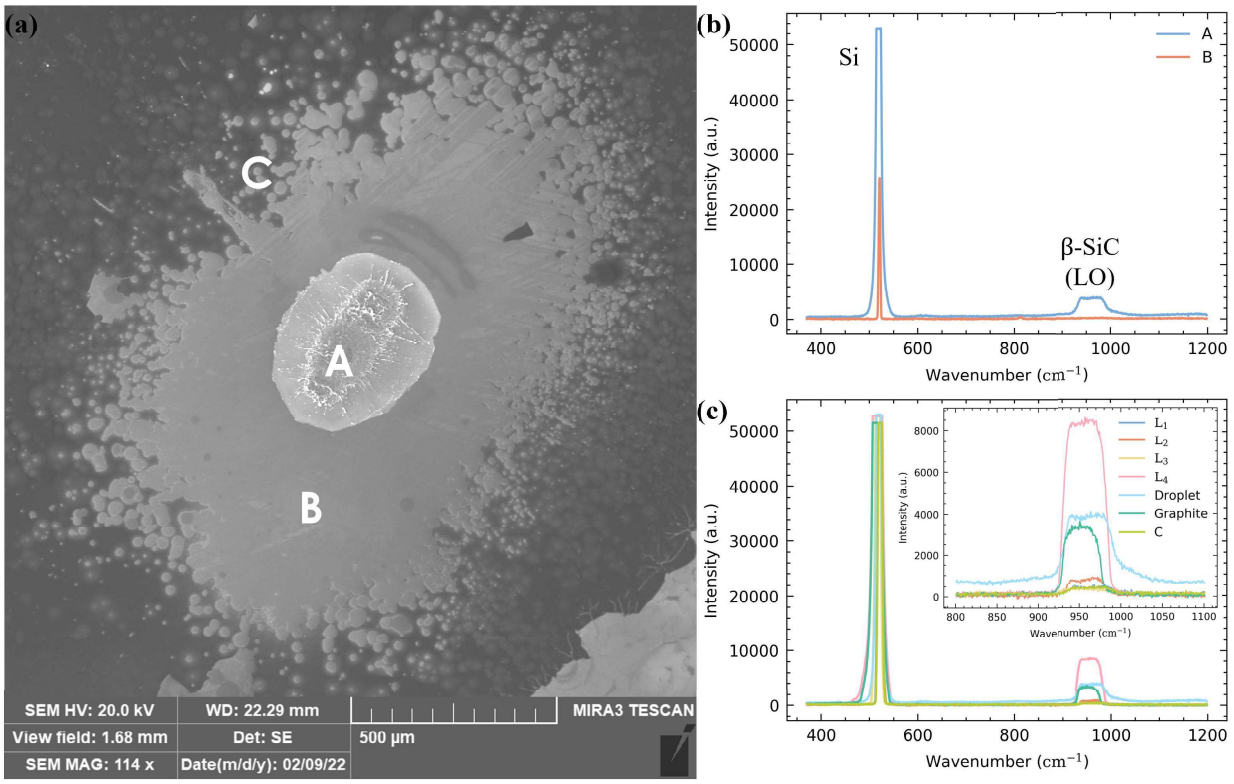

Figure 3.7 SEM image and measured Raman spectra of the Si/SiC laser processed dimple. (a) SEM image of the laser fabricated dot with surrounding areas, labeled as A, B, and C. A: area inside the laser dot. B: bare Si wafer, where the PMMA is melted away by the laser. C: PMMA phase-transition region due to the laser induced temperature. (b) Raman spectra of areas A and B, where the SiC Raman peak can be detected only at region A. (c) Raman spectra for area C and different laser fabrication parameters. An enlarged plot was inserted details SiC peaks locate from 800 cm^{-1} to 1100 cm^{-1}.

The measured Raman spectra was obtained as in Figure 3.7. As in Figure 3.7(a), there are three areas of interest labeled A, B, and C in the scanning electron microscope (SEM) image. Area A is the laser-focused dot that indicates SiC has formed and a Si/SiC junction exists between the film and the substrate. Area B is the surface of the unprocessed Si wafer, where the PMMA is vaporized as a result of excessive heat and is where no SiC is indicated in the Raman spectra. Region C is a result of PMMA phase transition because of the temperature, and where redeposition of material that reflected off the laser plume exists.

Raman signals were first compared between areas A and B, Figure 3.7(b). The peak at 521 cm^{-1} comes from the Si substrate. Signals from 930 cm^{-1} to 990 cm^{-1} are created by the optical and acoustic phonon modes of the β−SiC. Because of the short range ordered SiC crystallite structure,

and the signal from the surrounding Si there is an induced phonon mode damping as indicated by peak broadening that was observed in all samples [179]. In the figure, it is clear to see the peak of the longitudinal optical (LO) mode from region A, which matches previously reported work [180]–[182]. On the contrary, no peak was observed in area B, which confirms the validity of the selective laser fabrication technique. The measurements show no evidence of the transverse optic (TO) mode which peaks at 796 cm^{-1} for all laser processed samples. Since in back scattering geometry, the TO mode of 3C-SiC is not Raman active. The absence peak indicates that there are no stacking errors or interfacial dislocations and offsets between the crystal orientation of the synthesized SiC and Si substrate [183].

To investigate the influence of the quantity of carbon on the SiC generation, multi layer PMMA films were spun onto the Si substrate to increase the quantity of carbon while maintaining the other conditions to be the same. The results of the Raman measurements are plotted as in Figure 3.7(c), where the number of the PMMA layer is indicated as subscripts of L. An enlarged plot is inserted around the SiC peak. From L_1 to L_4, it shows a growing intensity, except for the result of L_3. A relatively stronger Raman intensity here corresponds to thicker fabricated SiC layers. The result suggests a positive trend in SiC thickness by depositing several layers of PMMA prior to the laser process. We interpret this as an increase in carbon content in the laser plume for thicker PMMA films.

To further study the SiC generation, we conducted experiments using a PMMA droplet for even thicker films, and separate experiments using graphite powders (no PMMA involved) as the carbon sources. Both have successfully provided carbon atoms and the created SiC can be detected as in Figure 3.7(c). The result points out that the sources for SiC synthesis are limited not only to carefully spun PMMA layers but also to other materials containing high quantities of carbon atoms.

In Figure 3.7, we also detected SiC Raman signals from area C. We interpret this as the re-deposition of ablated material that reflects back off the plume where some SiC is formed in the laser plume and redeposited onto the substrate in the surrounding area [184].

3.4 Advancements in SiC Synthesis using an Excimer Laser

From Figure 3.7, it is evident that the Raman intensity of the observed peaks exhibits a notable decrease when compared to the dominant Si peak. This discrepancy arises as a consequence of the slender SiC crystal thickness, leading to a restricted light propagation path within the material. Consequently, this limited path length curtails the extent of light-matter interactions, thus posing challenges in the acquisition of distinctive light scattering signals. Consequently, the issue at hand centers on the low SiC yield encountered through the prior methodology of selective laser fabrication, necessitating a resolution to this predicament.

In order to elucidate the underlying cause of the low yield, a comprehensive series of experiments were designed to better understand fundamental principles governing the phenomenon.

3.4.1 Findings from Si Powder Mixtures

The previous results of thicker PMMA films on Si substrates giving larger SiC Raman peaks was the impetus to investigate the possibility of fabricating even thicker films of SiC. To increase the surface area of the PMMA to Si interface, silicon powder was mixed with PMMA and this slurry was deposited on a sapphire substrate. The 248 nm KrF laser was used with a 25 ns single laser pulse and an energy of 264 mJ that was passed through a beam homogenizer. The laser was focused to a spot size of 1 mm^2 for a laser fluence of 453 mJ/cm^2. An optical image of the resulting structure is shown in Figure 3.8. A significant void could be seen under the laser spot location, indicating significant exfoliation during this process.

Raman analysis of the sample at the locations indicated in the optical microscope image shown in Figure 3.9 showed strong Raman peaks associated with SiC material. The SiC peaks could be found up to a millimeter away from the region directly impacted by the laser spot further suggesting significant exfoliation, and SiC formation in the laser plume itself.

3.4.2 Layered Structure for Finer Mixing

In an effort to decrease the SiC particle size, either finer Si powder in PMMA, or thin films of Si and PMMA could be pursued. Since fine Si powder can be pyrophoric, we chose to investigate thin films of amorphous Si, a-Si, and spun on PMMA. It was hypothesized that the SiC film thickness

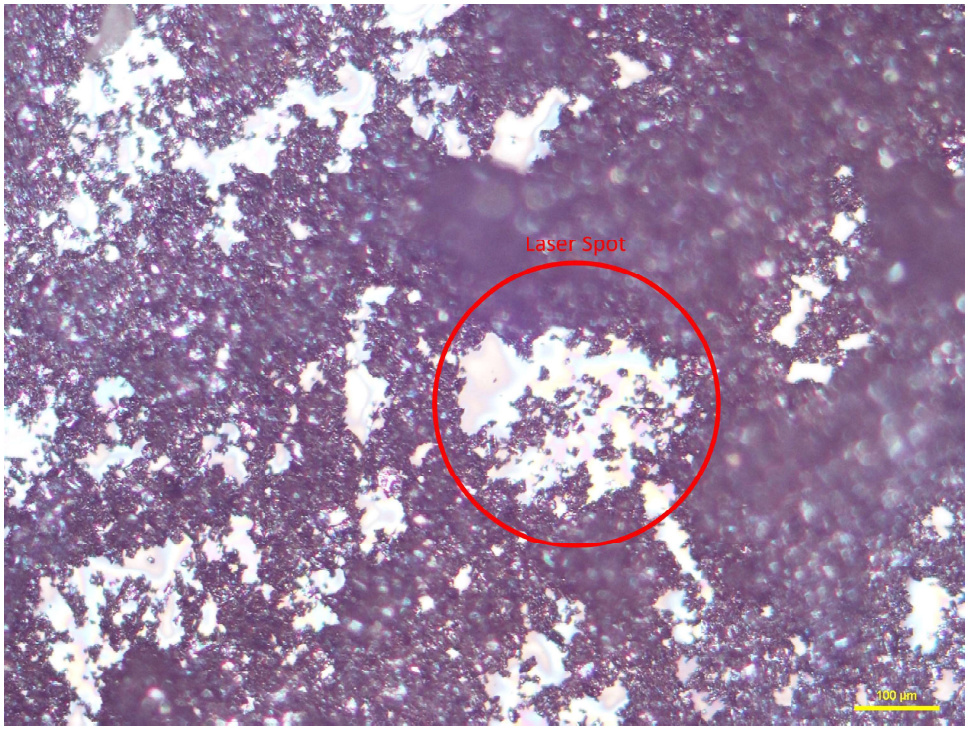

Figure 3.8 In this experimental setup, Si powder was mixed with PMMA. The red-circled area denotes the location targeted by the laser. A void is observed within this region, characterized by the absence of a substantial portion of Si powders. No discernible crystalline molten structure is observed in this void region. The scale bar is 100 µm.

could be controlled by the number of repeat layers of a-Si and PMMA. Figure 3.10 illustrates the implementation of this layered structure on a acetone and methanol cleaned 1-inch quartz (SiO_2) substrate. The layers consist of amorphous silicon (a-Si) interspersed with PMMA, forming the sequence a-Si/PMMA/a-Si/PMMA from bottom to top. Each a-Si layer has a thickness of 850 Å, and a softbake process at 180 °C is employed after each PMMA layer is spin-coated leading to a PMMA layer thickness of 2000 Å.

To explore the efficacy of the proposed layered structure, a series of laser conditions were investigated. Utilizing a KrF excimer laser at a wavelength of 248nm and pulse width of 25ns operating at an operating voltage of 19 kV, equivalent to approximately 264 mJ, distinct laser patterns were generated, each depicting a specific condition. The resulting dots, arranged from left to right in Figure 3.10, represent the following scenarios (designated as S_1 to S_7): continuous laser operation at 10 Hz for a duration of 20 seconds, a single laser pulse deliberately defocused by 2 mm, a precisely focused single laser pulse, two consecutive focused laser pulses, a sequence of

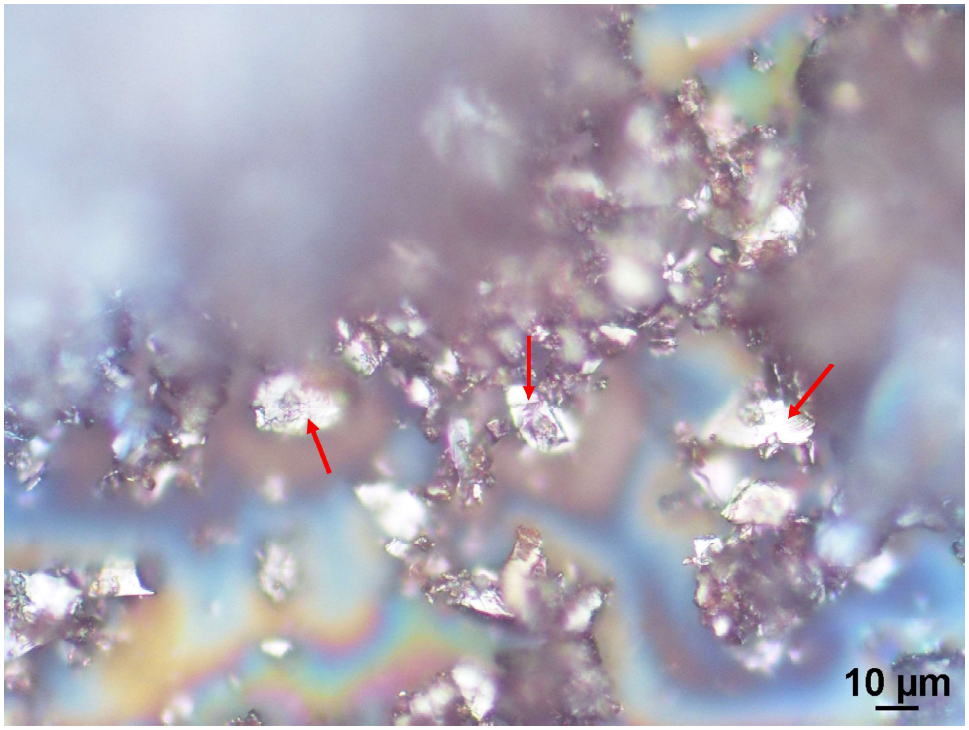

Figure 3.9 Detailed examination of the Si powder under an optical microscope reveals notable findings. The labeled regions, indicated by red arrows, exhibit distinct SiC Raman signals, signifying the presence of SiC material. Moreover, the presence of lustrous molten structures is evident, indicating the transformation of the Si powder under external influences. Importantly, it should be noted that these distinct structures manifest at a notable distance from the laser spot, emphasizing their spatial relationship within the experimental context.

five focused laser pulses, a succession of ten focused laser pulses, followed by another individual focused laser pulse, and concluded with two additional focused laser pulses. These deliberately varied scenarios serve as a valuable experimental platform for investigating the consequences of different laser settings on the resulting film.

The laser-induced dot patterns corresponding to each scenario are depicted in Figure 3.11. Notably, each scenario exhibits a distinct pattern generated by the laser, with the focused laser spots generally displaying a smaller diameter compared to the defocused patterns with the same number of laser pulses. For a more detailed examination of the dot patterns, refer to Figure 3.12, which specifically represents the sixth dot from the left in Figure 3.11. It is worth noting that the other dots exhibit similar structures when observed under higher magnifications. In Figure 3.12, a closer inspection reveals the presence of ring-like patterns accompanied by small particles.

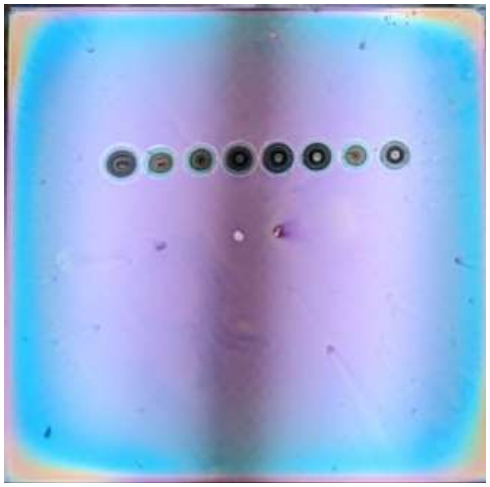

Figure 3.10 The depicted figure showcases a 1-inch quartz substrate featuring a layered structure composed of a-Si/PMMA/a-Si/PMMA. The laser is operated with an operating voltage of 19 kV, corresponding to an approximate energy of 264 mJ. The laser hit spots, arranged from left to right, demonstrate various scenarios: laser running at 10 Hz for 20 seconds, a single laser pulse defocused by 2 mm, a focused single laser pulse, two focused laser pulses, five focused laser pulses, ten focused laser pulses, another single focused laser pulse, and two additional focused laser pulses. Laser spots are placed 2 mm apart.

Raman spectroscopy from scenarios 5, 6 and 7 (as depicted in Figure 3.11) is shown in Figure 3.13. The Raman signals exhibit a peak intensity between the spectral range of 900 cm^{-1} and 980 cm^{-1}, which is specifically associated with SiC. This observed enhancement in peak intensity is particularly significant when comparing it to the results portrayed in Figure 3.7(b) and (c). These findings demonstrate the successful generation of a thicker SiC material through this layered film reactive PLD method. This approach can be further investigated both through COMSOL simulation and experimentally to better optimize the laser fluence, number of laser pulses, and the overall PMMA-Si layer thickness on a silicon substrate. This approach could also be utilized to

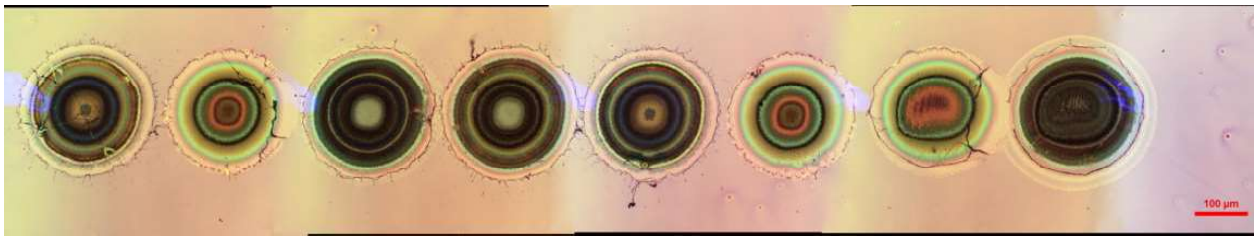

Figure 3.11 Figure presents a collection of microscopic images depicting the laser-induced dot patterns on the quartz substrate. This image provides a visual representation of the unique characteristics and spatial distribution associated with each laser-induced dot pattern. The scale bar is 100 µm.

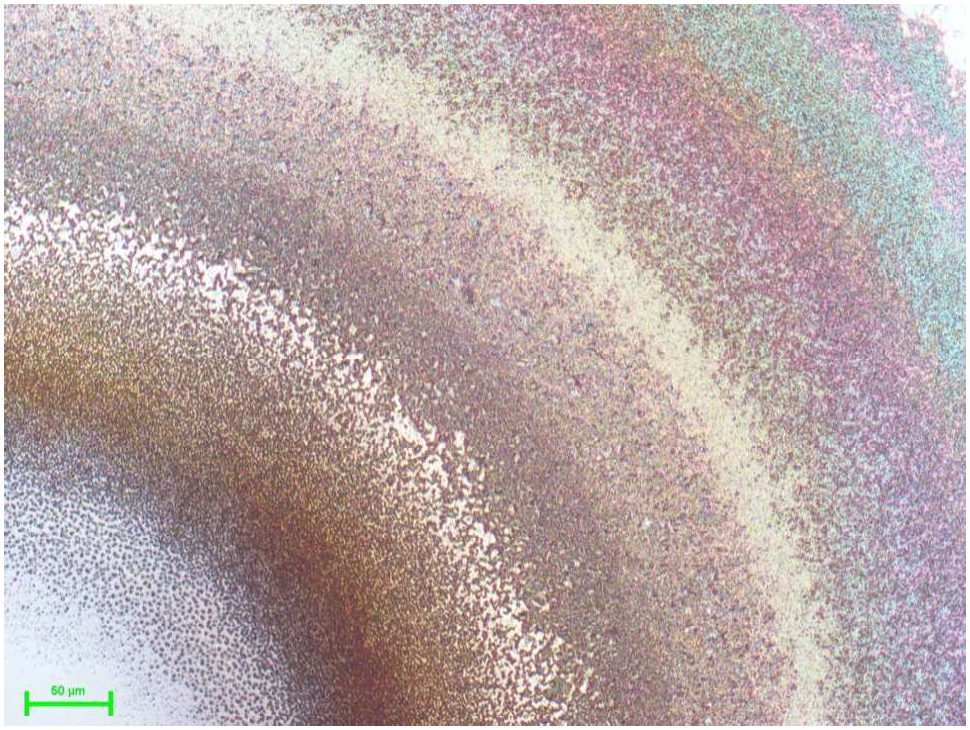

Figure 3.12 A close-up view of the laser dot pattern located in the sixth position from left to right. Upon examination, a distinctive ring-like pattern becomes apparent, accompanied by the presence of small particle-like crystals. The detailed microscopic image captured in this figure offers valuable insights into the unique characteristics and spatial arrangement exhibited by the laser-induced dots in this specific configuration. The scale bar is 50 µm.

deposit fine SiC particles onto a substrate by matrix assisted pulsed laser evaporation (MAPLE) [185].

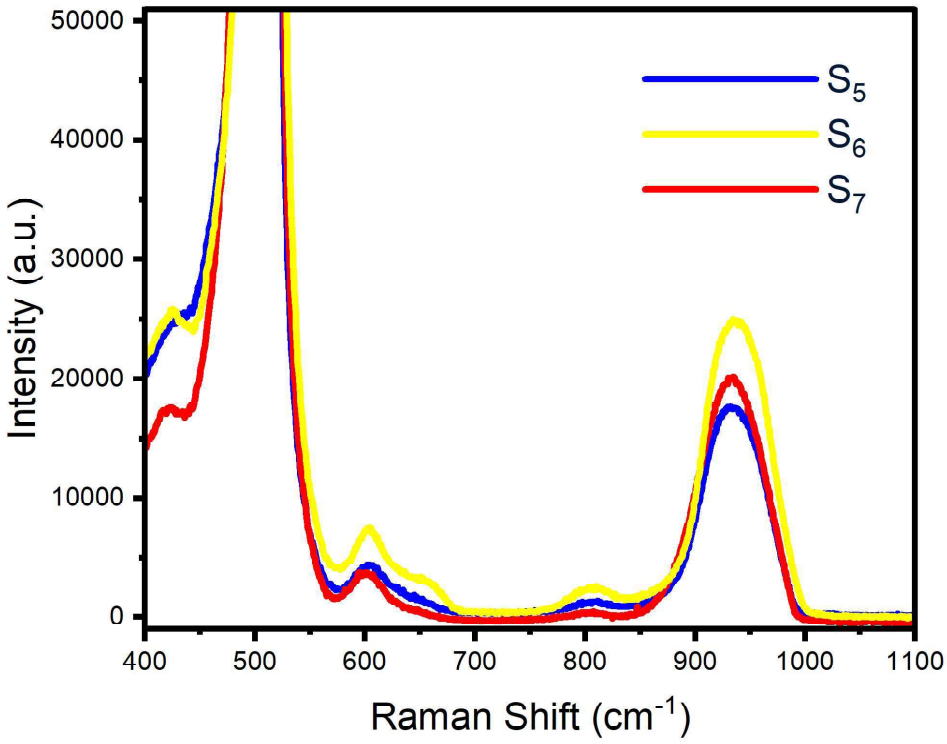

Figure 3.13 Raman spectra obtained from the nanocrystal structures within scenarios S_5, S_6, and S_7 are presented. The Raman signals obtained from these samples exhibit characteristic features indicative of SiC. It is noteworthy that Raman signals from other samples exhibit similar patterns, albeit with slight variations in signal intensity and spatial distribution within each respective laser-induced pattern.

CHAPTER 4

EXPLORING THE SYNTHESIS OF SILICON CARBIDE THROUGH REACTIVE PULSED LASER DEPOSITION

In the previous chapter it was demonstrated that a pulsed laser could be used to reactively convert two solid state source materials into silicon carbide on the surface of a substrate. Some control of the thickness of the resulting SiC was shown to be possible through multiple alternating layers of a-Si and PMMA. This chapter describes a different approach where the source material consisting of multiple alternating layers of a-Si and PMMA are deposited onto a sapphire substrate. The laser is then used to reactively combine the silicon and carbon from the PMMA film while transferring the resulting SiC to a silicon substrate placed in close proximity to the sapphire.

4.1 Introduction

In recent years, the field of radio frequency (RF) power electronics has witnessed a remarkable surge in interest surrounding the remarkable properties of silicon carbide. This wide bandgap semiconductor has evolved from being a promising material to an indispensable component in the realm of power electronic applications, particularly in the automotive industry [186], [187]. When

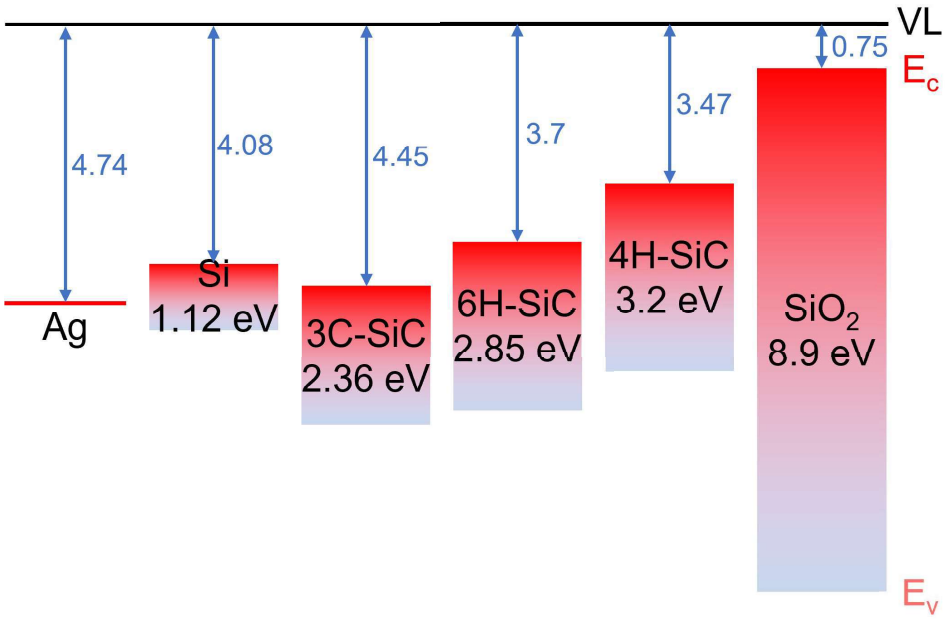

Figure 4.1 Band structures and band offsets of various electronic materials.

compared to conventional silicon based devices, SiC exhibits a remarkable array of superior physical properties. These include a significantly higher breakdown electrical field, an elevated electron saturation velocity, and a wider energy gap. Notably, the larger energy gap effectively reduces the generation of electron-hole pairs through thermal activation, thereby rendering SiC highly suitable for applications requiring high temperature operation and substantial power handling capabilities [160], [188], [189]. In addition to SiC, other wide bandgap materials like gallium nitride (GaN) and diamond (C) have garnered considerable attention in the scientific community. However, it is noteworthy that SiC stands out as the sole material capable of direct growth on Si substrates, enabling integration for signal processing and device operations (Figure 4.1). Particularly in the realm of microwave devices, bulk SiC has emerged as a leading contender for next-generation applications. Extensive research has already showcased the feasibility of diverse device types, encompassing heterojunction bipolar transistors (HBTs), Schottky barrier diodes, metal-semiconductor field-effect transistors (MESFETs), and high-electron-mobility transistors (HEMTs) [190]–[193]. The versatility of these devices has sparked great interest in the field of microwave technology, with extensive research being conducted to explore their applicability in various domains, including telecommunications and aerospace. Moreover, the presence of optically addressable spin-active quantum defects, known as color centers, in SiC has elevated its appeal as a material for quantum computing endeavors. Notably, several color centers, such as the nitrogen vacancy (NV), the negatively charged silicon vacancy at the hexagonal lattice site (h-V_{Si}), and the divacancy ($C_C V_{Si}$), have emerged as highly promising candidates for both experimental investigation and theoretical exploration [194], [195]. To facilitate these studies, the reduction of SiC material to smaller dimensions, such as nanoparticles (NPs) or quantum dots (QDs), is crucial. These downsized forms enable their utilization in photoluminescence (PL) and biological labeling [196].

The current synthesis methods for bulk SiC primarily involve the growth of epitaxial layers on Si substrates, posing significant challenges due to the substantial lattice mismatch and differences in thermal expansion. As a consequence, considerable residual stress is encountered upon cooldown from the elevated growth temperatures [197]. To address the thermal mismatch issues at the

junction, researchers have explored diverse techniques such as plasma-enhanced chemical vapor deposition (PECVD), buffer engineering, and low-temperature molecular beam epitaxy (MBE) [198]–[201]. Another approach to reduce the density of lattice dislocations entails selective epitaxial growth (SEG) or localized growth of the material within a confined region [202], [203]. However, these deposition processes necessitate elevated processing temperatures for the entire wafer, intricate epilayer engineering, or the utilization of carefully selected substrates with epitaxy seeds. Consequently, there is a pressing need to develop a technique for SiC synthesis on wafers containing pre-existing on-chip circuits, while simultaneously confining the high temperatures to the specific area designated for SiC growth.

Synthesis of SiC nanoparticles can be classified into three primary categories: liquid phase processes, solid phase processes, and vapor phase processes [204]. Liquid phase techniques, such as the sol-gel method and pulsed laser ablation in liquid (PLAL), require a subsequent high-temperature annealing step to fabricate SiC or utilize pre-synthesized solid SiC as the target for laser ablation. However, these approaches have inherent limitations. For instance, during the gel heating process in the synthesis of SiC nanoparticles, the particles may gradually transform into nanowires and whiskers due to heterogeneous nucleation and gradient-oriented nucleation mechanisms [205]. Moreover, the PLAL method is not suitable for large-scale preparation [206]. Solid phase processes, including high-energy ball milling, chemical etching, combustion synthesis, and carbothermal reduction, involve either high temperatures to initiate chemical reactions or the use of hazardous chemical solutions for etching [207]–[210]. The final group of growth methods comprises vapor phase techniques, with a primary focus on chemical vapor deposition (CVD). These methods employ a continuous gas flow, high temperature, and low-pressure conditions [211]. Therefore, there is a notable interest in developing a growth technique that can operate under ambient conditions, independent of pre-synthesized SiC, and free from the use of hazardous chemicals.

Recently, a novel technique for the selective fabrication of SiC through a local laser annealing process has been demonstrated [163]. This process utilizes PMMA as a carbon source and a pulsed

laser as the heat source. By subjecting the Si substrate to laser melting and dissociating the PMMA, a SiC thin film is reformed. Although this approach can be performed under ambient conditions, a post-etching procedure is still necessary to shape the SiC material. Furthermore, the method suffers from relatively low output efficiency, which is likely attributed to an incomplete understanding of the underlying mechanisms as illustrated in the previous sections.

To overcome these limitations, this study introduces a novel reactive pulsed laser deposition technique that operates under ambient conditions and eliminates the need for hazardous chemical etching. The process involves the placement of a target source, composed of alternating layers of Si and PMMA, over the desired fabrication region. Subsequently, a homogenized laser beam is employed to generate a localized hot spot that melts the Si and carbon-containing film layers. This process effectively disrupts the chemical bonds within the layers, leading to the ejection of atoms

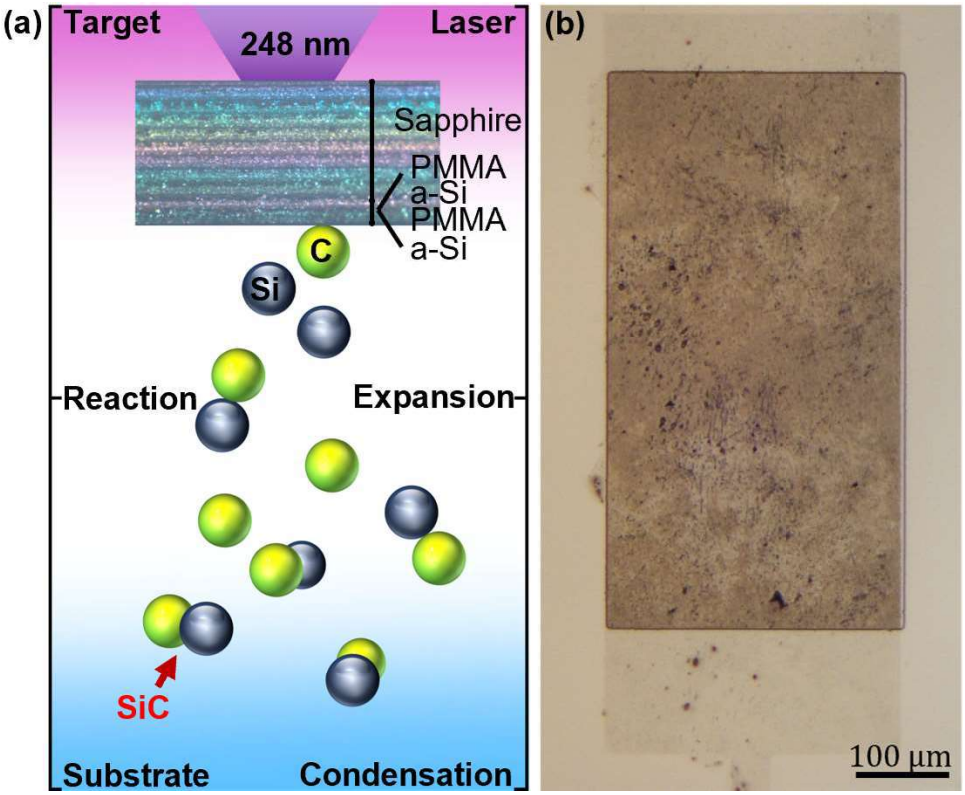

Figure 4.2 Schematic diagram illustrating (a) the target source mechanisms employed during the SiC deposition process, and (b) a representation of the SiC printed structure alongside the photoresist pattern after the proposed process. The SiC material is precisely deposited into a pre-patterned shape utilizing a commercially available photoresist, which can be subsequently modified and refined following the reactive pulsed laser procedure.

from the target source towards the substrate area through laser-induced plasma expulsion [185]. During the expansion of the plasma shockwave, Si and C atoms combine to form SiC nanoparticles, which subsequently condense onto the substrate surface, as depicted in Figure 4.2 (a). Unlike laser ablation, this directional ejection process involves the generation of SiC material during plasma expansion and its ejection towards the substrate [212].

Furthermore, the synthesized SiC particles undergo annealing with the substrate surface due to the localized heat caused by laser light that transmits through the sapphire substrate after expulsion of the PMMA/a-Si film. By employing a single or a few laser pulses, SiC nanoparticles with a random distribution can be generated. Conversely, employing multiple laser pulses allows for the production of a thicker SiC film by simply moving the sapphire to a fresh location between pulses. Leveraging the advantages of a movable stage, this technique enables selective local processing, ranging from SiC nanoparticle deposition to SiC film growth. Additionally, commercially available photoresists can serve as a mask to facilitate the printing of SiC into pre-patterned shapes. It is also feasible to pattern the SiC after the printing process is completed, as demonstrated in Figure 4.2 (b).

This innovative approach was successfully employed to fabricate a diode using SiC/Si material, resulting in a distinct current rectification behavior of the device. Simultaneously, our novel methodology facilitated the generation of SiC nanoparticles, which exhibited photoluminescent properties when excited with different wavelengths.

4.2 Setup and Fabrication

In preparation for the synthesis procedure, a source target is created by coating a transparent sapphire substrate with multiple layers of amorphous Si (a-Si) and PMMA films. Two layers of a-Si with thickness of 85 nm each and two layers of PMMA with 200 nm each. The selection of sapphire as the substrate material for the target is based on its minimal interaction with the incident laser beam, ensuring optimal performance.

As depicted in Figure 4.3, the SiC selective printing system incorporates a computer-controlled high-power KrF excimer laser featuring a pulse duration of 25 ns and a wavelength of λ = 248 nm.

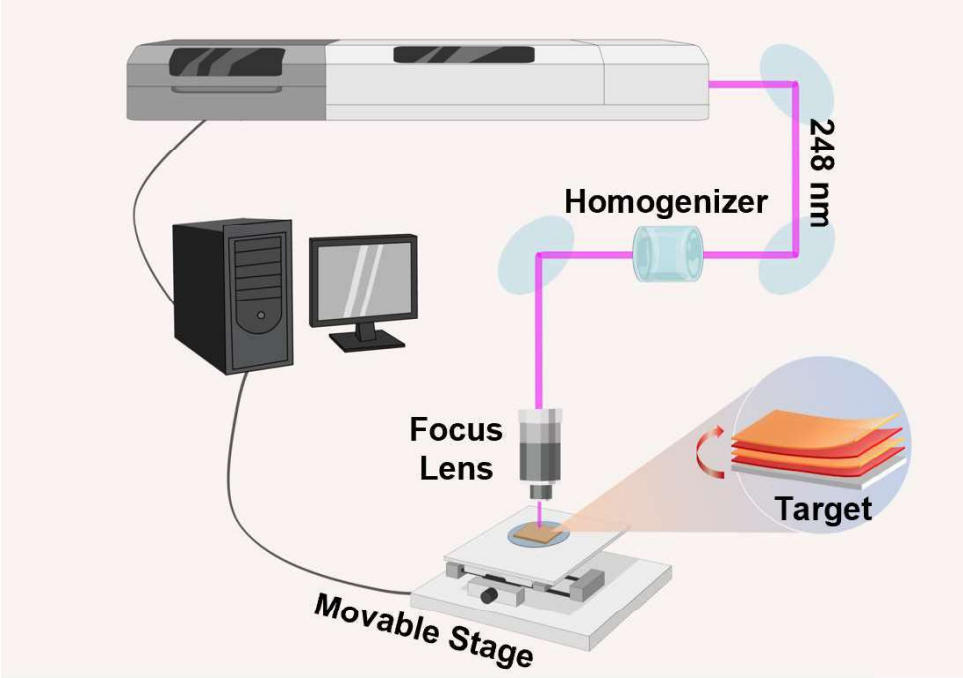

Figure 4.3 Schematic diagram of the SiC selective printing system showcasing its key components, including a high-power KrF excimer laser, reflecting mirrors, beam homogenizer, microscope lens, movable stage, and computer for precise control. Schematic figure was drawn by Figdraw.

To ensure even illumination across the desired focal area, the sample is exposed to the excimer laser beam directed through an optical path specifically designed to homogenize and shape the intensity profile. Subsequently, a microscope focus lens is employed to concentrate the laser onto the surface of the sample substrate. The resulting spot size is measured to be approximately 1 mm^2, with an intensity recorded at 453 mJ/cm^2. Throughout the manufacturing process, the samples are positioned on a movable stage, which is under the precise control of a computer system. By administering commands from the computer, the fabrication process can be executed across the entirety of the wafer.

Quartz (SiO_2) microscope slides and Si wafers were prepared as substrates to investigate the optical and electrical properties of synthesized SiC material. In the fabrication process, the target source was carefully positioned upside down on the substrate, allowing for controlled material ejection towards the desired region. By precisely triggering the computer-controlled laser pulse, the printing procedure described earlier was executed on the substrate surface.

Figure 4.4 presents a comparative Raman spectra analysis, highlighting the effectiveness of two

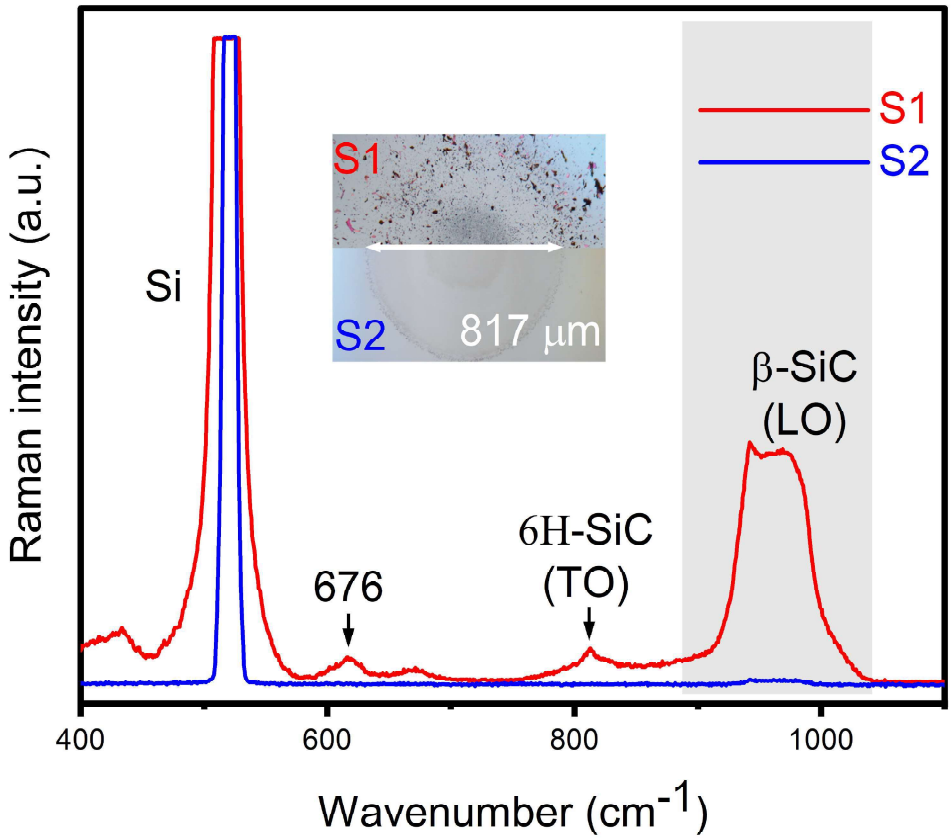

Figure 4.4 Raman spectra comparison of sample S1 and S2, along with their corresponding optical images. Sample S1 was prepared using a Si wafer covered with the sapphire target source, while sample S2 was synthesized using a Si substrate with a PMMA layer of approximately 200 nm thickness.

distinct laser fabrication methods. Sample S1 was generated by utilizing a Si wafer with a sapphire target source covered on top, while sample S2 was synthesized employing a Si substrate with an approximately 200 nm-thick PMMA coating.

Upon exposure to a 532 nm laser, both sample S1 and sample S2 underwent 10 laser pulses, with the sapphire target in S1 remaining stationary to enable a comparative analysis. The resulting Raman spectrum exhibited several broad peaks at approximately 521, 676, 812, and 940 to 980 cm^{-1}. The observed peak broadening can be attributed to various factors [179]. One contributing factor is the damping of phonon modes, which is influenced by the short-range ordering of SiC crystallites. The immediate vicinity surrounding the SiC site contains Si clusters and debris, further contributing to the observed broadening. The 521 cm^{-1} peak corresponds to the Si substrates, while the peaks ranging from 940 cm^{-1} to 980 cm^{-1} are associated with the acoustical and optical modes of β-SiC

[179], [181]. The absence of the transverse optical mode (TO) in the Raman spectrum suggests that the examination solely involved back scattering and indicates a lower presence of stacking faults in the crystal [183]. In this case, the Raman signal from sample S1 exhibits relatively higher intensity compared to that of sample S2, indicating the presence of a considerably thicker film. This difference can be attributed to the significant expulsion of material in this laser processing technique such that the covered target transfers significant material from the sapphire surface to the silicon substrate below it, in contrast to the uncovered case in sample S2 where the synthesized SiC particles disperse away from the substrate. The microscopy image inserted in Figure 4.4 highlights a distinct contrast between the two samples due to the confined plasma and localized heating of the silicon substrate. The Raman spectrum also reveals a prominent peak at 812 cm^{-1}, corresponding to the transverse optical mode (TO) of the 6H-SiC crystal [213]. Additionally, the signal at 676 cm^{-1} is attributed to the scattering of defect-induced transverse and longitudinal acoustic phonon modes [214].

As previously mentioned, employing multiple laser pulses in the proposed method allows for the synthesis of a thicker SiC film. Figure 4.5 presents Nanoscan measurements of the printed SiC film obtained with 2, 5, and 10 laser pulses. The greyed lines in the figure represent the raw data with a resolution of 0.5 μm, while the solid lines indicate the average thickness of each sample across the entire printed area. To ensure an ample supply of source material for printing, the target source was shifted to a new location after each pulse. It is evident from the figure that the use of multiple laser pulses results in the creation of thicker and larger SiC films.

To evaluate the electrical properties of the synthesized SiC, thick films were fabricated on both n-type (N_d = 1×10^{15} cm^{-3}) and p-type (N_a = 1×10^{16} cm^{-3}) doped Si wafers using the proposed technique with 10 laser pulses. A 300 nm thick layer of aluminum (Al) was deposited to establish the metal contact with the Si substrate, while a combination of 30 nm nickel (Ni) and 100 nm Al was deposited on the SiC surface to create the Ohmic contact. The resulting SiC/Si diode structure is depicted in Figure 4.6.

For the study of optical characteristics, the above method was used to print SiC onto a quartz

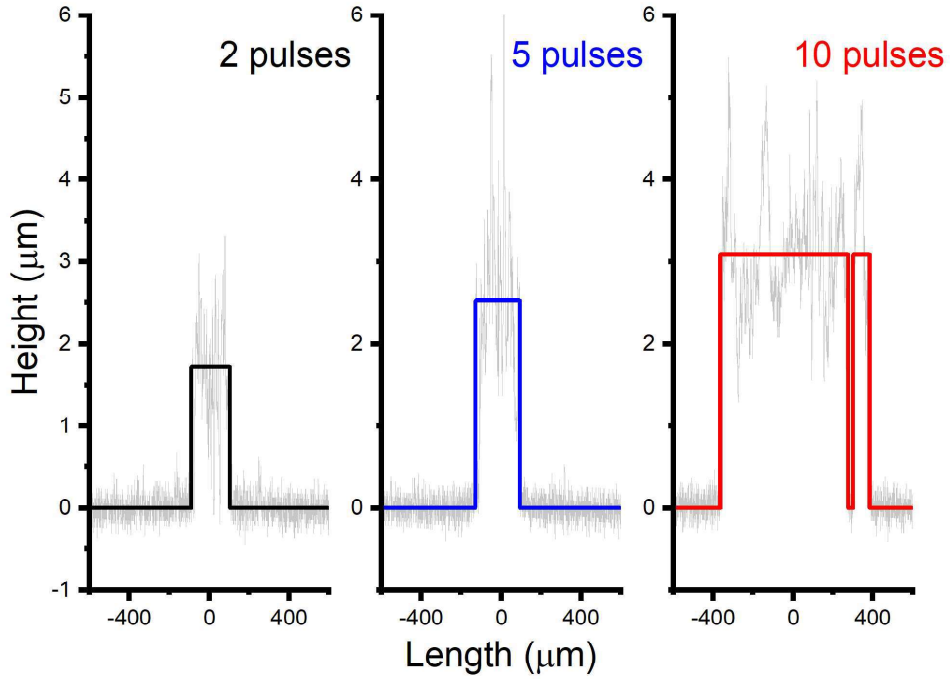

Figure 4.5 Nanoscan characterization of SiC films printed with different numbers of laser pulses. The grey lines in the figure represent scanned data with a resolution of 0.5 μm, while the solid lines indicate the average thickness of the SiC films across the deposited area.

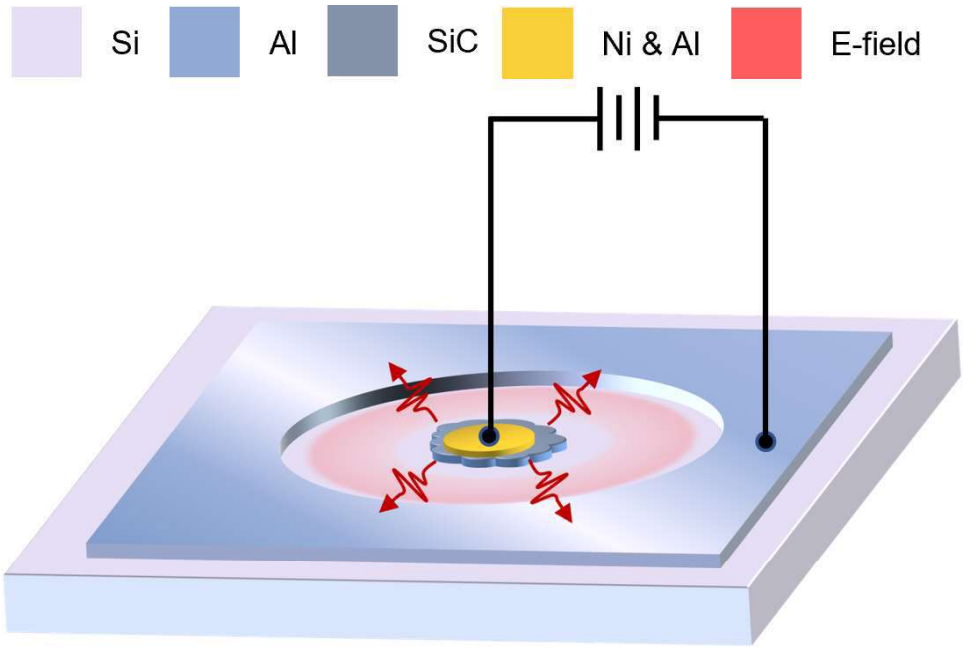

Figure 4.6 Schematic diagram illustrating the SiC/Si diode structure.

substrate. Different light sources with varying wavelengths were used to excite the sample, which was subsequently observed under photoluminescence microscopy. Here, SiC nanoparticles were formed on the quartz substrate with just a single laser pulse, thus enabling the potential formation of plasmons to enhance the photoresponse [215].

4.3 Experimental Results

4.3.1 Current-Voltage Characteristics

All measurements reported in this section were performed under ambient conditions without external light illumination. Figure 4.7 illustrates the charge transport characteristics of the SiC/Si heterostructure with a large metal contact (150 μm diameter). The samples designated as S_n and S_p correspond to n-type and p-type doped Si, respectively. The measured results reveal the typical behavior of a p-n diode, exhibiting current rectification. Notably, sample S_n exhibits an impressive on-off ratio of 1×10^3 when evaluated at 0 V and 60 V, accompanied by a threshold voltage of 37 V. The leakage current densities (J) were recorded as 2.19 μA/cm^2 and 32.59 μA/cm^2 at 0 V and -20 V, respectively. Sample S_p exhibits similar charge transport behavior, albeit with a smaller threshold voltage of 13 V. The current rectifying ratio for S_p is approximately 4×10^2, defined between 0 V and 20 V. The leakage current densities at 0 V and -20 V were measured as 2.32 μA/cm^2 and 12.41 μA/cm^2, respectively. The observed breakdown voltage for both samples occurs around -25 V, indicating the presence of tunneling, where impurity densities negatively affect the breakdown voltage [133]. The localized thermal quenching induced by the laser during fabrication results in increased leakage current and decreased effective breakdown voltage [216], [217].

Figure 4.8 illustrates the dark current-voltage (J-V) curves of the examined samples, presented on a logarithmic scale. The data reveals distinct variations in slope at higher forward biases, indicating the presence of defects at the junctions between the semiconductor and metal components, leading to suboptimal connections. These observed defects can be attributed to the intense local laser exposure during the fabrication process, which generates a high density of disorder trap states. These trap states serve as recombination centers, causing recombination current to surpass diffusion current. This finding highlights the potential for enhancing the quality of SiC materials by optimizing

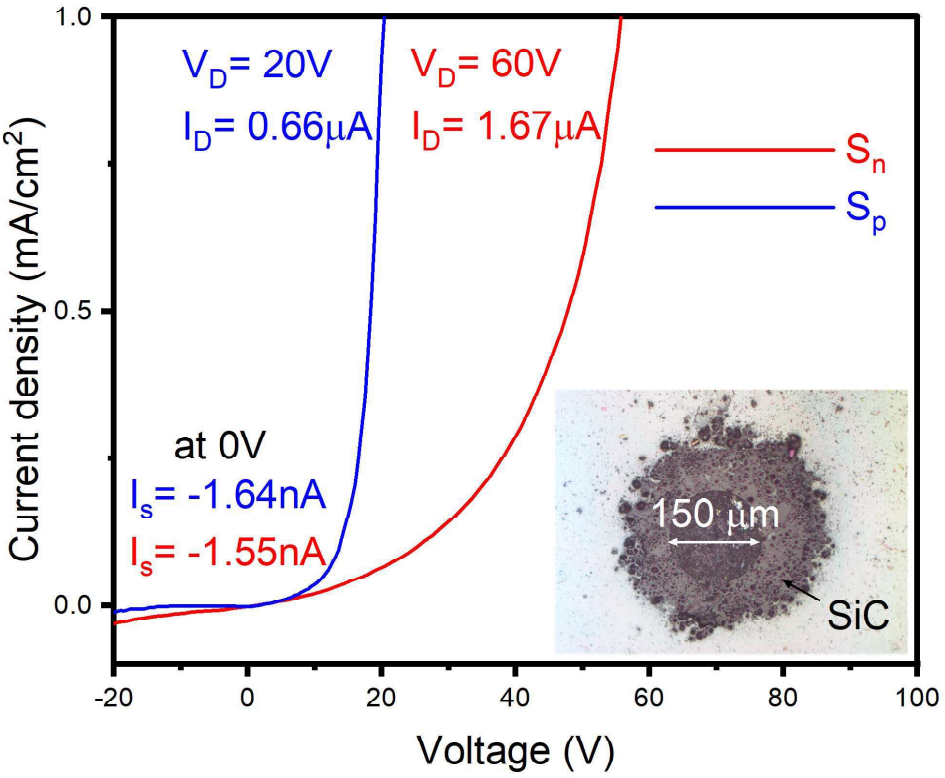

Figure 4.7 Dark current density-voltage (J-V) characteristics of the S_n and S_p heterojunctions. The microscopy image inset showcases the printed SiC material, highlighting the visible 150 μm diameter metal contact area in the center.

the laser power. Moreover, the calculated resistance at lower biases demonstrates that sample S_n exhibits higher resistance compared to S_p. This disparity arises not only from the presence of defects but also from the inherent potential difference at the heterojunction. As depicted in Figure 4.9 (a) and (b), E_n is larger than E_p, resulting in a higher turn-on voltage for S_n. During testing, it should be noted that other current mechanisms, such as multistep recombination-tunneling and trap-assisted tunneling, also influence the rectifying ratio.

4.3.2 Optical Characteristics

SiC, a well-known indirect bandgap semiconductor, is typically characterized by relatively low luminance. However, recent research on 3C-SiC QDs has revealed their remarkable photoluminescence comparable to those of direct bandgap QDs [218]. In the case of group IV semiconductor materials, the emission of light is heavily influenced by the Bohr radius, where the quantum confinement effect dictates a shift towards shorter wavelengths as the material size decreases. Fur-

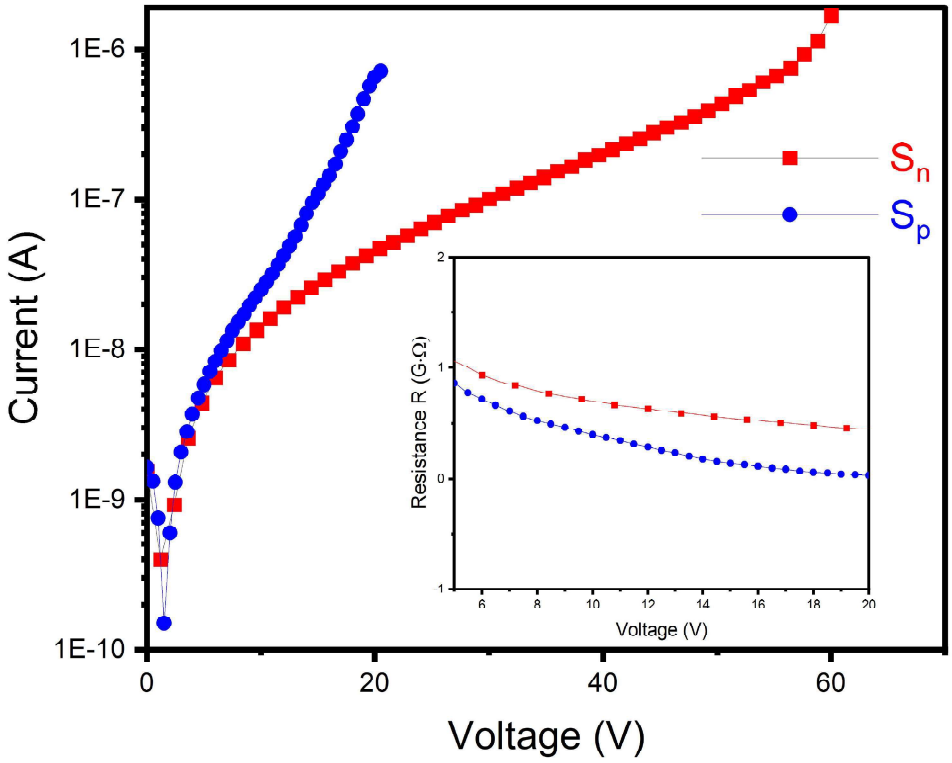

Figure 4.8 Dark current density-voltage (J-V) characteristics of the S_n and S_p heterojunctions. The microscopy image inset showcases the printed SiC material, highlighting the visible metal contact area in the center.

thermore, the presence of interior defects, such as synthesis-dependent substitutional impurities and vacancies, can lead to interband carrier recombinations and correlated luminescence, where the brightness correlates with the concentration of these defects. By leveraging the proposed explosive process, SiC films with natural dislocations and vacancies can be fabricated. In this section, these films will be printed using a single laser pulse without additional modifications, allowing for the investigation of various optical mechanisms spanning from UV to near-infrared light.

To conduct the experiments, a UV light source emitting at a wavelength of λ = 254 nm was utilized, and a filter was employed to eliminate any light below 385 nm. The scanning results are depicted in Figure 4.10, where the baseline signifies the detected light when only the pristine quartz substrate is positioned beneath the detector. The red line represents the detected light when the quartz substrate is coated with the printed SiC nanocrystals. Notably, the figure showcases a significant variation in intensity across a broad spectral range, approximately ranging from 430 nm

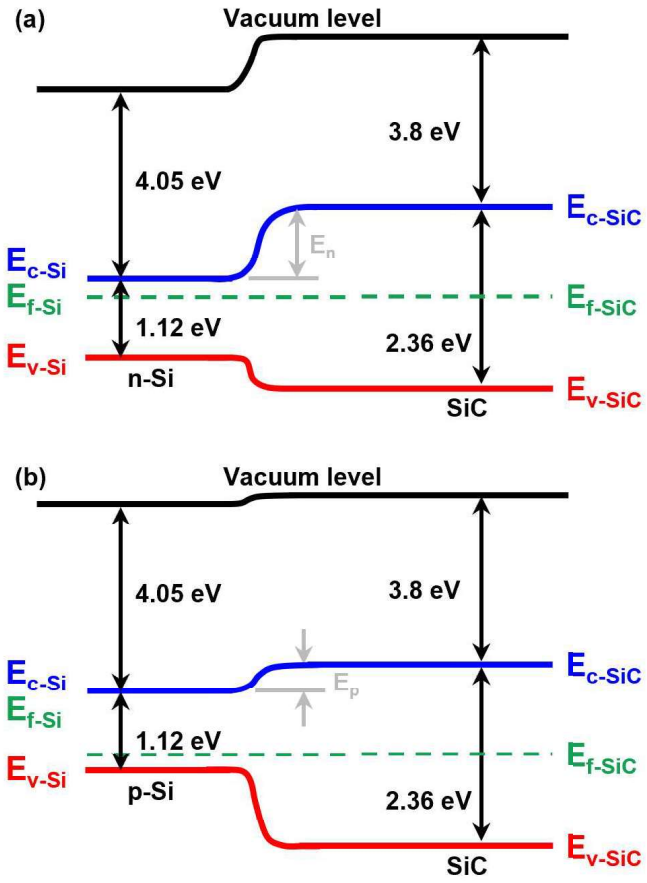

Figure 4.9 Energy band diagrams of the diodes fabricated using selective laser printing at 0 V bias. (a) Depicts the S_n heterojunction with a barrier of E_n, and (b) displays the S_p heterojunction with a lower built-in potential of E_p.

to 680 nm, with the exception of leakage light below the 385 nm wavelength. This broad intensity change captures the intricate optical dynamics associated with the indirect excitation and relaxation of electron-hole pairs on the SiC nanocrystal-coated surface.

When exposed to incident light with a wavelength of 254 nm, the individual photons carry a relatively high energy of E_{ph} = 4.88 eV, surpassing the energy bandgap of 3C-SiC, which has been reported to be 2.36 eV [219]. As a result, the excess energy is dissipated through the generation of phonons and lattice vibrations, which play a crucial role in maintaining momentum conservation during the excitation process. During the relaxation phase, photons are expected to be emitted at a wavelength of 525 nm, which aligns with the bandgap of the material. Notably, this emitted wavelength falls within the range covered by the detected signal, indicating a close correlation

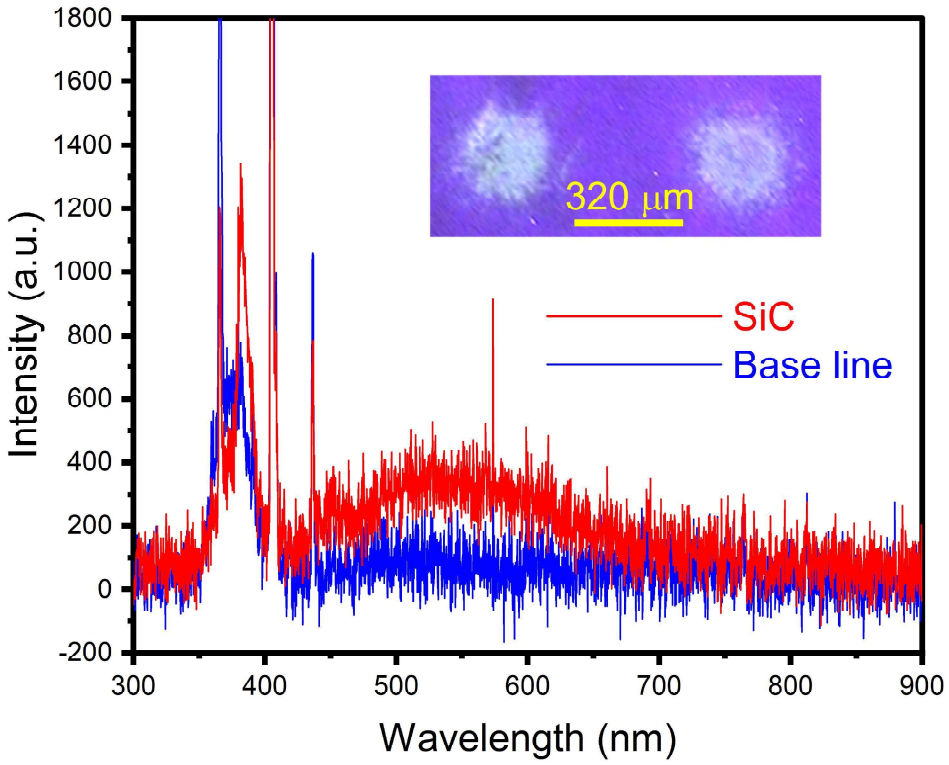

Figure 4.10 Comparison of the photoluminescence emitted by the SiC nanocrystals generated using a single laser pulse with the photoluminescence of the quartz substrate, which serves as the baseline. The photoluminescence microscopy image, depicted in the inset, showcases the emitted light, with the purple background resulting from the inherent wavelength imprecision of the UV light source.

between the relaxation process and the observed spectral variation. Furthermore, Figure 4.10 reveals a prominent peak at 380 nm, corresponding to a photon energy of 3.26 eV. While this could potentially be attributed to the presence of the 4H allotrope of SiC [220], further investigation is necessary to fully comprehend the underlying factors contributing to this peak. Factors such as the precision of the UV light source and the attenuation caused by the filter should be taken into account to gain a comprehensive understanding of this observed phenomenon.

To gain deeper insights into the photoluminescence characteristics of SiC nanocrystals, a visible light source with a wavelength of 540 nm and a photon energy of 2.3 eV, slightly below the bandgap of SiC, was employed. Figure 4.11 presents the photoluminescence microscopy image, illustrating the observed light emission. Despite the incident light's energy being insufficient to induce the photoluminescence effect theoretically, we observed light emission resulting from the

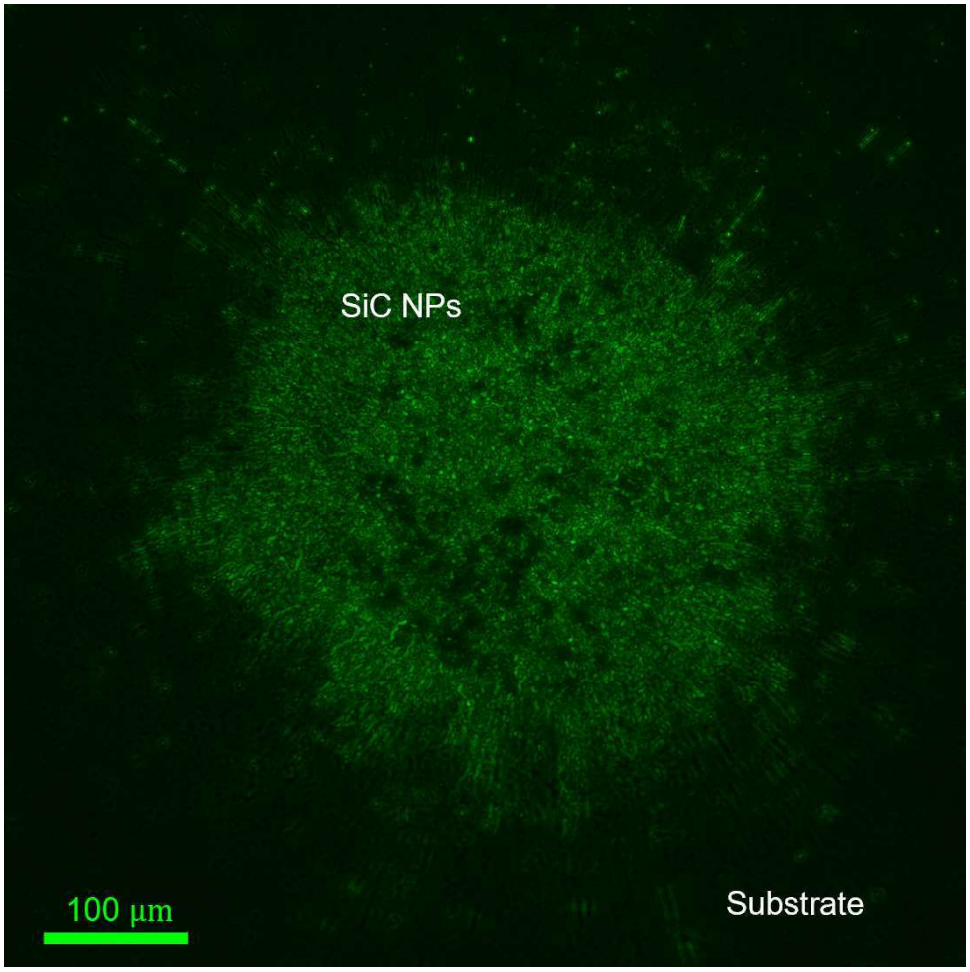

Figure 4.11 Photoluminescence microscopy image of SiC nanoparticles fabricated using the proposed method, excited with a 540 nm light source. The laser-printed SiC nanoparticles are visually represented by the green region, while the quartz substrate appears as a dark area. This image serves as a compelling visual confirmation of the successful implementation of the proposed fabrication technique, showcasing an effective printing area that exhibits notable photoluminescence effects.

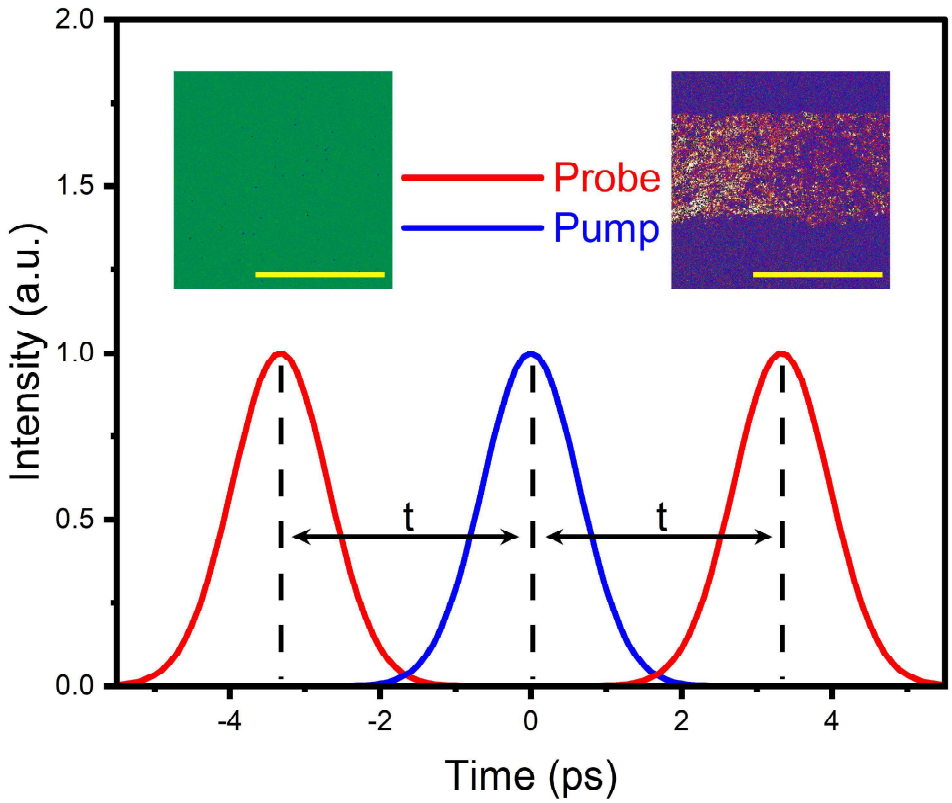

Figure 4.12 Schematic illustration depicting the temporal relationship between the probe and pump pulses, with a precise time interval of t = 3.33 ps. The synchronized photodetector is aligned with the probe pulses, while the specialized filter effectively eliminates the pump light, enabling exclusive detection of the transmitted probe light. The accompanying images at the respective time positions present the calculated 931 nm photon absorption of the sample, exhibiting a discernible pattern and heightened absorption when the pump pulse is introduced, as compared to absorption observed with probe-only incident light. To enhance visibility, the images were adjusted using ImageJ due to their relatively lower contrast compared to metallic nanostructures reported in previous studies [221]. The scale bars in the images indicate a length of 100 µm, serving as a reference for size measurements.

interplay of two photoluminescence mechanisms: quantum confinement and defect-related transitions, with the defects eventually dominating the photon emissions. Interestingly, when subjected to photoluminescence microscopy using an excitation wavelength of 488 nm, no light emission was detected, emphasizing the significant influence of defect types on the energy of the emitted photons. These findings underscore the intricate and multifaceted nature of the photoluminescence behavior exhibited by the synthesized SiC nanoclusters.

To further understand the dynamics of excitation in these randomly distributed SiC nanocrystals,

we utilized an advanced probe and pump system capable of generating near-infrared wavelengths, allowing us to explore their nonlinear optical properties. As depicted in Figure 4.12, our experimental configuration involved directing a probe with a wavelength of 931 nm onto the sample, followed by a pump light at 1040 nm after a precisely timed interval of t = 3.33 ps. Subsequently, an additional probe pulse was directed onto the sample after a further 3.33 ps delay. To achieve pulse durations of 1.5 picoseconds, we intentionally chirped the laser pulses. To capture the transmitted light, we employed a highly sensitive photodetector equipped with a specialized filter designed to effectively eliminate the 1040 nm pump light, enabling us to selectively detect and analyze only the transmitted 931 nm light. By comparing the detected probe light intensity with the intensity of the source, the absorptance of the SiC nanoparticles could be determined. The absorptance differences, elucidating the influence of the 1040 nm photons, are illustrated in the accompanying images in Figure 4.12. Notably, at t = -3.33 ps, the probe light passing through the sample exhibited negligible changes in intensity. However, in the presence of the preceding pump beam, a distinct enhancement in probe photon absorption was observed. This observation provided clear evidence of the SiC material deposited by the reactive pulsed laser, as demonstrated by the scanned picture. Further details and comprehensive results can be found in Figure 4.13.

To enhance the visual contrast between the substrate and the deposited material, a simple pattern was implemented. As shown in Figure 4.13(a), an optical microscopy image reveals the presence of a channel created by pre-spinning photoresist, which served as a guiding path for SiC deposition. Within this channel, the SiC materials are clearly distinguishable, and the laser-induced sputtering process has generated a noticeable pattern visible in the image.

Figure 4.13(b) and (c) present the results obtained through scanning specific regions of interest using the probe and pump system. The red and yellow boxes represent distinct areas. The brighter regions in these images indicate an increase in photon absorption due to the presence of the pump beam.

The underlying physical principles of this phenomenon can be explained by the collective nonlinear interactions between light and matter, specifically through a two-photon absorption

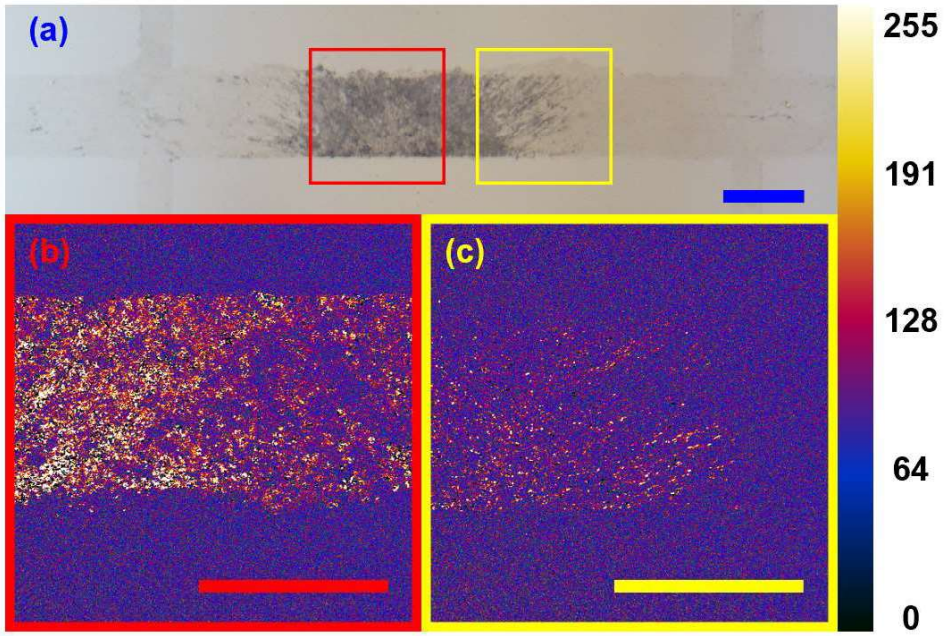

Figure 4.13 (a) Optical microscopy image displaying the deposited area of SiC nanocrystals fabricated using a reactive single-pulsed laser technique. A simple pattern was utilized to facilitate comparison with the substrate material. (b) Probe photon absorption at a wavelength of 931 nm within the red boxed region depicted in (a), highlighting distinct variations compared to the quartz substrate. (c) Probe photon absorption at a wavelength of 931 nm focused on the yellow boxed area shown in (a). Scale bars with a length of 100 µm ensure accurate representation of size. The scanned images were adjusted using ImageJ to enhance contrast, and an arbitrary unit color bar is provided to illustrate the relations of 931 nm photon absorption.

process in the context of our study. Without the 1040 nm (1.19 eV) beam, the 931 nm (1.33 eV) light alone lacks the necessary energy to generate electron-hole pairs. Instead, the energy carried by the incident photons is transferred to crystal vibrations within the material. However, with the introduction of two-photon excitation, the combined photon energy (2.52 eV) becomes sufficient to bridge the bandgap of SiC, allowing for the creation of electron-hole pairs. This distinction is clearly evident in the scanned images. Furthermore, the longer wavelength of the near-infrared beam enables deeper penetration into the material, increasing the likelihood of luminescence originating from defects and trap states.

4.4 Conclusion

In summary, this study introduces a novel SiC reactive pulsed laser deposition technique for the synthesis of SiC nanoparticles and thin films. By utilizing a homogenized laser beam, a

localized hot spot is generated, causing the melting of Si and PMMA layers in a target source. This process triggers a laser-induced plasma plume, resulting in the formation of SiC onto a substrate. The synthesized SiC particles can be conveniently printed onto substrates, either with a random distribution or in pre-patterned shapes, using commercially available photoresists and a liftoff technique. Raman spectroscopy analysis was conducted to validate the successful synthesis of SiC materials. The results from the Raman spectroscopy and nanoscan confirm the presence of SiC and demonstrate that thicker films can be obtained by employing multiple reactive laser pulses. Furthermore, the electrical properties of the synthesized SiC were evaluated through current-voltage characteristics, which revealed typical diode behavior and rectification. The SiC/Si heterostructure showed electron-dominant charge transport, and measurements of leakage current densities were measured for both n-type and p-type doped Si. In addition, the fabricated SiC materials exhibited interesting photoluminescence effects when excited with different wavelengths originating from the semiconductor material or crystal defects. This finding opens possibilities for applications in various fields, including bio-labeling, quantum technologies, and optoelectronics.

In conclusion, the SiC reactive pulsed laser deposition technique presented in this study offers a promising and environmentally friendly approach for the selective synthesis and fabrication of SiC materials. The ability to precisely control the deposition process and achieve desired material properties makes it a highly attractive method with potential applications in diverse fields.

CHAPTER 5

FUTURE RESEARCH DIRECTIONS

5.1 Plasmonic Nanostructure Devices

In the context of plasmonic nanostructure photodetectors, this dissertation has effectively demonstrated the impact of the vertical gap. This phenomenon, intricately linked with semiconductor thickness, offers a streamlined approach to mitigating challenges associated with electron-beam lithography. As a natural progression, the forthcoming stages of research could be directed towards as the following:

1. Exploring Different 2D Semiconductor Materials: The current study has provided valuable insights into the effects of the vertical gap on plasmonic nanostructure photodetectors using MoS_2. A promising direction for future work could involve investigating the behavior of different 2D semiconductor materials within similar plasmonic nanostructure setups. This exploration could shed light on how various energy band gaps and material properties influence the enhancement of electric fields, photocurrent generation, and overall device performance.

2. Optimizing Nanostructure Geometries: The simulation results have demonstrated the significant impact of nanostructure geometries on the enhancement of electric fields and light absorption. Future research could focus on optimizing these geometries to achieve even higher field enhancements and absorption efficiencies. This could involve systematic studies to determine the most favorable configurations for enhanced performance.

3. Characterization of Other Plasmonic Materials: While gold nanoarrays have been the primary focus in this study, there are various other plasmonic materials with distinct properties. Investigating the effects of using different plasmonic materials, such as silver or aluminum, within the proposed photodetector structure could provide insights into how material properties influence plasmonic enhancement and device performance.

4. Multi-Physics Simulations: To gain a more comprehensive understanding of the device behavior, future research could involve multi-physics simulations that consider not only electromagnetic interactions but also thermal effects. This would provide insights into how plasmonic heating

influences carrier generation, recombination, response delay and overall device stability.

5. Nonlinear Optical Effects: The investigation into nonlinear optical absorption presented a glimpse into the potential nonlinear properties of the NAs/MoS_2/NAs structure. Future research could delve deeper into these nonlinear effects and explore their applications in areas such as all-optical signal processing, nonlinear spectroscopy, and nonlinear imaging.

6. Integration with Existing Technologies: Exploring the integration of the proposed photodetector technology with existing electronics and photonics platforms could facilitate the development of practical devices for specific applications.

5.2 Reactive Pulsed Laser Deposition of Silicon Carbide

For reactive pulsed laser deposition of SiC, there are several potential paths for future work that can build upon the presented research and address certain aspects for improvement and advancement. Here are some suggestions for future directions:

1. Ultra-High Vacuum Operation: The article discusses the synthesis of SiC nanoparticles and thin films using a reactive pulsed laser deposition technique under ambient conditions. However, for more controlled and precise material synthesis, you could consider implementing the process in an ultra-high vacuum (UHV) environment. This would help eliminate contamination and undesired dopants from the ambient atmosphere, leading to improved material quality and consistency.

2. Crystal Defect Reduction: The article mentions that the synthesized SiC materials exhibited photoluminescence effects attributed to crystal defects. One can focus on further reducing these crystal defects by optimizing the laser-induced thermal annealing process. Investigate different annealing temperatures, durations, and cooling rates to find conditions that minimize defects and enhance material properties.

3. Quantum Defect Engineering: Since SiC is known for hosting optically addressable spin-active quantum defects (color centers), future research can delve deeper into engineering and characterizing these defects. Explore different techniques to control the formation and concentration of specific color centers, such as NV centers, which have potential applications in quantum sensing and quantum information processing.

4. While the article employs Raman spectroscopy and photoluminescence microscopy for material characterization, consider incorporating more advanced techniques. For example, transmission electron microscopy (TEM) and X-ray diffraction (XRD) can provide detailed insights into crystal structure, nanoparticle size distribution, and lattice defects.

5. Surface Passivation: To improve the performance of SiC-based devices, consider studying surface passivation techniques. Surface defects and dangling bonds can lead to undesirable electronic properties. Developing methods to passivate these surface states can enhance device performance, especially in high-frequency applications.

BIBLIOGRAPHY

[1] Z. Sun and Y. H. Hu, "How magical is magic-angle graphene?" *Matter*, vol. 2, no. 5, pp. 1106–1114, 2020.

[2] K. Kim, A. DaSilva, S. Huang, *et al.*, "Tunable moiré bands and strong correlations in small-twist-angle bilayer graphene," *Proceedings of the National Academy of Sciences*, vol. 114, no. 13, pp. 3364–3369, 2017.

[3] Q. H. Wang, K. Kalantar-Zadeh, A. Kis, J. N. Coleman, and M. S. Strano, "Electronics and optoelectronics of two-dimensional transition metal dichalcogenides," *Nature nanotechnology*, vol. 7, no. 11, pp. 699–712, 2012.

[4] M. Buscema, M. Barkelid, V. Zwiller, H. S. van der Zant, G. A. Steele, and A. Castellanos-Gomez, "Large and tunable photothermoelectric effect in single-layer mos_2," *Nano letters*, vol. 13, no. 2, pp. 358–363, 2013.

[5] H. Xu, J. Wu, Q. Feng, N. Mao, C. Wang, and J. Zhang, "High responsivity and gate tunable graphene-mos_2 hybrid phototransistor," *Small*, vol. 10, no. 11, pp. 2300–2306, 2014.

[6] B. Radisavljevic, A. Radenovic, J. Brivio, V. Giacometti, and A. Kis, "Single-layer mos_2 transistors," *Nature nanotechnology*, vol. 6, no. 3, pp. 147–150, 2011.

[7] Z. Yin, H. Li, H. Li, *et al.*, "Single-layer mos_2 phototransistors," *ACS nano*, vol. 6, no. 1, pp. 74–80, 2012.

[8] S. F. Cogan, D. J. Edell, A. A. Guzelian, Y. Ping Liu, and R. Edell, "Plasma-enhanced chemical vapor deposited silicon carbide as an implantable dielectric coating," *Journal of Biomedical Materials Research Part A: An Official Journal of The Society for Biomaterials, The Japanese Society for Biomaterials, and The Australian Society for Biomaterials and the Korean Society for Biomaterials*, vol. 67, no. 3, pp. 856–867, 2003.

[9] H. Matsunami and T. Kimoto, "Step-controlled epitaxial growth of sic: High quality homoepitaxy," *Materials Science and Engineering: R: Reports*, vol. 20, no. 3, pp. 125–166, 1997.

[10] I. Ferain, C. A. Colinge, and J.-P. Colinge, "Multigate transistors as the future of classical metal–oxide–semiconductor field-effect transistors," *Nature*, vol. 479, no. 7373, pp. 310–316, 2011.

[11] F. Schwierz, J. Pezoldt, and R. Granzner, "Two-dimensional materials and their prospects in transistor electronics," *Nanoscale*, vol. 7, no. 18, pp. 8261–8283, 2015.

[12] M. Chhowalla, D. Jena, and H. Zhang, "Two-dimensional semiconductors for transistors," *Nature Reviews Materials*, vol. 1, no. 11, pp. 1–15, 2016.

[13] M. Li, S. K. Cushing, and N. Wu, "Plasmon-enhanced optical sensors: A review," *Analyst*, vol. 140, no. 2, pp. 386–406, 2015.

[14] H. A. Atwater and A. Polman, "Plasmonics for improved photovoltaic devices," *Nature materials*, vol. 9, no. 3, pp. 205–213, 2010.

[15] J. D. Jackson, *Classical electrodynamics*, 1998.

[16] L. D. Landau, J. S. Bell, M. Kearsley, L. Pitaevskii, E. Lifshitz, and J. Sykes, *Electrodynamics of continuous media*. elsevier, 2013, vol. 8.

[17] P. A. D. Gonçalves and N. M. Peres, *An introduction to graphene plasmonics*. World Scientific, 2016.

[18] S. A. Maier *et al.*, *Plasmonics: fundamentals and applications*. Springer, 2007, vol. 1.

[19] P. A. D. Gonçalves, *Plasmonics and Light–Matter Interactions in Two-Dimensional Materials and in Metal Nanostructures: Classical and Quantum Considerations*. Springer Nature, 2020.

[20] M. Born and E. Wolf, "Principles of optics, 7th (expanded) edition," *United Kingdom: Press Syndicate of the University of Cambridge*, vol. 461, pp. 401–424, 1999.

[21] J. Stratton, "Electromagnetic theory, mcgraw-hill, new york, 1941," *There is no corresponding record for this reference (cit. on p. 10)*, 1941.

[22] K. Spyrou and P. Rudolf, *Functionalization of graphene*, 2014.

[23] A. A. Maradudin, J. R. Sambles, and W. L. Barnes, *Modern plasmonics*. Elsevier, 2014.

[24] H. Raether, "Plasmons on smooth and rough surfaces and on gratings," *Springer tracts in modern physics*, vol. 10, 1988.

[25] M. Freitag, "Nanoelectronics goes flat out," *Nature nanotechnology*, vol. 3, no. 8, pp. 455–457, 2008.

[26] A. K. Geim and I. V. Grigorieva, "Van der waals heterostructures," *Nature*, vol. 499, no. 7459, pp. 419–425, 2013.

[27] Y. Liu, N. O. Weiss, X. Duan, H.-C. Cheng, Y. Huang, and X. Duan, "Van der waals heterostructures and devices," *Nature Reviews Materials*, vol. 1, no. 9, pp. 1–17, 2016.

[28] F. Bonaccorso, Z. Sun, T. Hasan, and A. Ferrari, "Graphene photonics and optoelectronics," *Nature photonics*, vol. 4, no. 9, pp. 611–622, 2010.

[29] F. Xia, H. Wang, D. Xiao, M. Dubey, and A. Ramasubramaniam, "Two-dimensional material nanophotonics," *Nature Photonics*, vol. 8, no. 12, pp. 899–907, 2014.

[30] A. K. Geim and K. S. Novoselov, "The rise of graphene," *Nature materials*, vol. 6, no. 3, pp. 183–191, 2007.

[31] K. S. Novoselov, A. K. Geim, S. V. Morozov, *et al.*, "Two-dimensional gas of massless dirac fermions in graphene," *nature*, vol. 438, no. 7065, pp. 197–200, 2005.

[32] J. Lahiri, Y. Lin, P. Bozkurt, I. I. Oleynik, and M. Batzill, "An extended defect in graphene as a metallic wire," *Nature nanotechnology*, vol. 5, no. 5, pp. 326–329, 2010.

[33] S. Miryala, V. Tenace, A. Calimera, E. Macii, and M. Poncino, "Ultra-low power circuits using graphene p–n junctions and adiabatic computing," *Microprocessors and Microsystems*, vol. 39, no. 8, pp. 962–972, 2015.

[34] K. Novoselov, S. Morozov, T. Mohinddin, *et al.*, "Electronic properties of graphene," *physica status solidi (b)*, vol. 244, no. 11, pp. 4106–4111, 2007.

[35] P. Avouris, Z. Chen, and V. Perebeinos, "Carbon-based electronics," *Nature nanotechnology*, vol. 2, no. 10, pp. 605–615, 2007.

[36] J. H. Gosling, O. Makarovsky, F. Wang, *et al.*, "Universal mobility characteristics of graphene originating from charge scattering by ionised impurities," *Communications Physics*, vol. 4, no. 1, p. 30, 2021.

[37] W. S. Leong, H. Wang, J. Yeo, *et al.*, "Paraffin-enabled graphene transfer," *Nature communications*, vol. 10, no. 1, p. 867, 2019.

[38] H. K. Ng, D. Xiang, A. Suwardi, *et al.*, "Improving carrier mobility in two-dimensional semiconductors with rippled materials," *Nature Electronics*, vol. 5, no. 8, pp. 489–496, 2022.

[39] D. Svintsov, V. Vyurkov, S. Yurchenko, T. Otsuji, and V. Ryzhii, "Hydrodynamic model for electron-hole plasma in graphene," *Journal of Applied Physics*, vol. 111, no. 8, 2012.

[40] Y. Cao, V. Fatemi, S. Fang, *et al.*, "Unconventional superconductivity in magic-angle graphene superlattices," *Nature*, vol. 556, no. 7699, pp. 43–50, 2018.

[41] J. Bai, X. Zhong, S. Jiang, Y. Huang, and X. Duan, "Graphene nanomesh," *Nature nanotechnology*, vol. 5, no. 3, pp. 190–194, 2010.

[42] X. Li and H. Zhu, "Two-dimensional mos_2: Properties, preparation, and applications," *Journal of Materiomics*, vol. 1, no. 1, pp. 33–44, 2015.

[43] S. Andleeb, A. K. Singh, and J. Eom, "Chemical doping of mos_2 multilayer by p-toluene sulfonic acid," *Science and Technology of Advanced Materials*, 2015.

[44] O. Lopez-Sanchez, D. Lembke, M. Kayci, A. Radenovic, and A. Kis, "Ultrasensitive photodetectors based on monolayer mos_2," *Nature nanotechnology*, vol. 8, no. 7, pp. 497–501, 2013.

[45] Y. Zhang, B. Zheng, C. Zhu, *et al.*, "Single-layer transition metal dichalcogenide nanosheet-based nanosensors for rapid, sensitive, and multiplexed detection of dna," *Advanced Materials*, vol. 27, no. 5, pp. 935–939, 2015.

[46] M. Acerce, D. Voiry, and M. Chhowalla, "Metallic 1t phase mos_2 nanosheets as supercapacitor electrode materials," *Nature nanotechnology*, vol. 10, no. 4, pp. 313–318, 2015.

[47] Q. Ding, B. Song, P. Xu, and S. Jin, "Efficient electrocatalytic and photoelectrochemical hydrogen generation using mos_2 and related compounds," *Chem*, vol. 1, no. 5, pp. 699–726, 2016.

[48] H. Li, J. Wu, Z. Yin, and H. Zhang, "Preparation and applications of mechanically exfoliated single-layer and multilayer mos_2 and wse2 nanosheets," *Accounts of chemical research*, vol. 47, no. 4, pp. 1067–1075, 2014.

[49] D. J. Late, B. Liu, H. R. Matte, C. Rao, and V. P. Dravid, "Rapid characterization of ultrathin layers of chalcogenides on sio2/si substrates," *Advanced Functional Materials*, vol. 22, no. 9, pp. 1894–1905, 2012.

[50] R. Kappera, D. Voiry, S. E. Yalcin, *et al.*, "Phase-engineered low-resistance contacts for ultrathin mos_2 transistors," *Nature materials*, vol. 13, no. 12, pp. 1128–1134, 2014.

[51] A. K. Singh, P. Kumar, D. Late, A. Kumar, S. Patel, and J. Singh, "2d layered transition metal dichalcogenides (mos_2): Synthesis, applications and theoretical aspects," *Applied Materials Today*, vol. 13, pp. 242–270, 2018.

[52] D. Jariwala, V. K. Sangwan, D. J. Late, *et al.*, "Band-like transport in high mobility unencapsulated single-layer mos_2 transistors," *Applied Physics Letters*, vol. 102, no. 17, 2013.

[53] B. Radisavljevic, M. B. Whitwick, and A. Kis, "Integrated circuits and logic operations based on single-layer mos_2," *ACS nano*, vol. 5, no. 12, pp. 9934–9938, 2011.

[54] K. F. Mak, C. Lee, J. Hone, J. Shan, and T. F. Heinz, "Atomically thin mos_2: A new direct-gap semiconductor," *Physical review letters*, vol. 105, no. 13, p. 136 805, 2010.

[55] M. Shanmugam, C. A. Durcan, and B. Yu, "Layered semiconductor molybdenum disulfide nanomembrane based schottky-barrier solar cells," *Nanoscale*, vol. 4, no. 23, pp. 7399–

7405, 2012.

[56] M. N. Ashfold, F. Claeyssens, G. M. Fuge, and S. J. Henley, "Pulsed laser ablation and deposition of thin films," *Chemical Society Reviews*, vol. 33, no. 1, pp. 23–31, 2004.

[57] L.-C. Chen, D. Chrisey, and G. Hubler, "Pulsed laser deposition of thin films," *Wiley, New York*, 1994.

[58] P. Willmott and J. Huber, "Pulsed laser vaporization and deposition," *Reviews of Modern Physics*, vol. 72, no. 1, p. 315, 2000.

[59] I. G. Pallikaris and D. S. Siganos, *Excimer laser in situ keratomileusis and photorefractive keratectomy for correction of high myopia*, 1994.

[60] S. Georgiou and A. Koubenakis, "Laser-induced material ejection from model molecular solids and liquids: Mechanisms, implications, and applications," *Chemical reviews*, vol. 103, no. 2, pp. 349–394, 2003.

[61] X. Chen, Y. Lu, Y. Wu, B. J. Cho, W. Song, and D. Dai, "Optical properties of siox nanostructured films by pulsed-laser deposition at different substrate temperatures," *Journal of applied physics*, vol. 96, no. 6, pp. 3180–3186, 2004.

[62] A. A. Salih, A. Nazar, and A. J. Haider, "Antibacterial activity of zno nanoparticle prepared by pulsed laser ablation in liquid for biological sensor," in *2019 12th International Conference on Developments in eSystems Engineering (DeSE)*, IEEE, 2019, pp. 726–729.

[63] A. Daway Thamir, A. J Haider, and G. A Ali, "Preparation of nanostructuretio2 at different temperatures by pulsed laser deposition as solar cell," *Engineering and Technology Journal*, vol. 34, no. 2, pp. 193–204, 2016.

[64] J. Rau, I. Cacciotti, A. De Bonis, *et al.*, "Fe-doped hydroxyapatite coatings for orthopedic and dental implant applications," *Applied surface science*, vol. 307, pp. 301–305, 2014.

[65] D. J. Joe, S. Kim, J. H. Park, *et al.*, "Laser–material interactions for flexible applications," *Advanced materials*, vol. 29, no. 26, p. 1 606 586, 2017.

[66] A. J. Haider, T. Alawsi, M. J. Haider, B. A. Taha, and H. A. Marhoon, "A comprehensive review on pulsed laser deposition technique to effective nanostructure production: Trends and challenges," *Optical and Quantum Electronics*, vol. 54, no. 8, p. 488, 2022.

[67] A. Giardini, V. Marotta, A. Morone, S. Orlando, and G. Parisi, "Thin films deposition in rf generated plasma by reactive pulsed laser ablation," *Applied surface science*, vol. 197, pp. 338–342, 2002.

[68] R. K. Singh and J. Narayan, "A novel method for simulating laser-solid interactions in

semiconductors and layered structures," *Materials Science and Engineering: B*, vol. 3, no. 3, pp. 217–230, 1989.

[69] H. D. Vora, S. Santhanakrishnan, S. P. Harimkar, S. K. Boetcher, and N. B. Dahotre, "One-dimensional multipulse laser machining of structural alumina: Evolution of surface topography," *The International Journal of Advanced Manufacturing Technology*, vol. 68, pp. 69–83, 2013.

[70] A. Miotello and R. Kelly, "Laser-induced phase explosion: New physical problems when a condensed phase approaches the thermodynamic critical temperature," *Applied Physics A*, vol. 69, no. Suppl 1, S67–S73, 1999.

[71] R. Kelly and A. Miotello, "Comments on explosive mechanisms of laser sputtering," *Applied Surface Science*, vol. 96, pp. 205–215, 1996.

[72] V. Oliveira and R. Vilar, "Finite element simulation of pulsed laser ablation of titanium carbide," *Applied surface science*, vol. 253, no. 19, pp. 7810–7814, 2007.

[73] A. Morozov, "Thermal model of pulsed laser ablation: Back flux contribution," *Applied Physics A*, vol. 79, pp. 997–999, 2004.

[74] X. Guo, Q. Xun, Z. Li, and S. Du, "Silicon carbide converters and mems devices for high-temperature power electronics: A critical review," *Micromachines*, vol. 10, no. 6, p. 406, 2019.

[75] b. H. Morkoc, S. Strite, G. Gao, M. Lin, B. Sverdlov, and M. Burns, "Large-band-gap sic, iii-v nitride, and ii-vi znse-based semiconductor device technologies," *Journal of Applied physics*, vol. 76, no. 3, pp. 1363–1398, 1994.

[76] M. E. Levinshtein, S. L. Rumyantsev, and M. S. Shur, *Properties of Advanced Semiconductor Materials: GaN, AlN, InN, BN, SiC, SiGe*. John Wiley & Sons, 2001.

[77] V. Presser and K. G. Nickel, "Silica on silicon carbide," *Critical reviews in solid state and materials sciences*, vol. 33, no. 1, pp. 1–99, 2008.

[78] N. Ohtani, J. Takahashi, M. Katsuno, H. Yashiro, and M. Kanaya, "Development of large single-crystal sic substrates," *Electronics and Communications in Japan (Part II: Electronics)*, vol. 81, no. 6, pp. 8–19, 1998.

[79] H. Pedersen, S. Leone, O. Kordina, *et al.*, "Chloride-based cvd growth of silicon carbide for electronic applications," *Chemical reviews*, vol. 112, no. 4, pp. 2434–2453, 2012.

[80] N. G. Wright, A. B. Horsfall, and K. Vassilevski, "Prospects for sic electronics and sensors," *Materials today*, vol. 11, no. 1-2, pp. 16–21, 2008.

[81] C. Codreanu, M. Avram, E. Carbunescu, and E. Iliescu, "Comparison of 3c–sic, 6h–sic and 4h–sic mesfets performances," *Materials Science in Semiconductor Processing*, vol. 3, no. 1-2, pp. 137–142, 2000.

[82] M. Bhatnagar and B. J. Baliga, "Comparison of 6h-sic, 3c-sic, and si for power devices," *IEEE Transactions on electron devices*, vol. 40, no. 3, pp. 645–655, 1993.

[83] K. Shenai, R. S. Scott, and B. J. Baliga, "Optimum semiconductors for high-power electronics," *IEEE transactions on Electron Devices*, vol. 36, no. 9, pp. 1811–1823, 1989.

[84] A. D. Yoffe, "Semiconductor quantum dots and related systems: Electronic, optical, luminescence and related properties of low dimensional systems," *Advances in physics*, vol. 50, no. 1, pp. 1–208, 2001.

[85] J. Li and A. Steckl, "Nucleation and void formation mechanisms in sic thin film growth on si by carbonization," *Journal of the Electrochemical Society*, vol. 142, no. 2, p. 634, 1995.

[86] J. Ye, S. Zhang, and W. E. Lee, "Novel low temperature synthesis and characterisation of hollow silicon carbide spheres," *Microporous and Mesoporous Materials*, vol. 152, pp. 25–30, 2012.

[87] T. Zhai, L. Li, Y. Ma, *et al.*, "One-dimensional inorganic nanostructures: Synthesis, field-emission and photodetection," *Chemical Society Reviews*, vol. 40, no. 5, pp. 2986–3004, 2011.

[88] X. Lin, S. Lin, Y. Xu, *et al.*, "Ab initio study of electronic and optical behavior of two-dimensional silicon carbide," *Journal of Materials Chemistry C*, vol. 1, no. 11, pp. 2131–2135, 2013.

[89] M. Rauber, I. Alber, S. Müller, *et al.*, "Highly-ordered supportless three-dimensional nanowire networks with tunable complexity and interwire connectivity for device integration," *Nano letters*, vol. 11, no. 6, pp. 2304–2310, 2011.

[90] F. La Via, M. Camarda, and A. La Magna, "Mechanisms of growth and defect properties of epitaxial sic," *Applied Physics Reviews*, vol. 1, no. 3, 2014.

[91] J. Zhang, W. Li, Q. Jia, L. Lin, J. Huang, and S. Zhang, "Molten salt assisted synthesis of 3c–sic nanowire and its photoluminescence properties," *Ceramics International*, vol. 41, no. 10, pp. 12 614–12 620, 2015.

[92] J. Seo, S. Sankarasubramanian, and B. Lee, "Templated, carbothermal reduction synthesis of mesoporous silicon carbide from carbon nanotube–mesoporous silica core–shell composite," *Bulletin of Materials Science*, vol. 41, pp. 1–6, 2018.

[93] K. Sun, T. Wang, W. Gong, *et al.*, "Synthesis and potential applications of silicon carbide

nanomaterials/nanocomposites," *Ceramics International*, 2022.

[94] M. Raju, S. Sen, D. Sarkar, and C. Jacob, "Synthesis of 3c-silicon carbide 1d structures by carbothermal reduction process," *Journal of Alloys and Compounds*, vol. 857, p. 158 243, 2021.

[95] Z. An, H. Wang, C. Zhu, H. Cao, and J. Xue, "Synthesis and formation mechanism of porous silicon carbide stacked by nanoparticles from precipitated silica/glucose composites," *Journal of Materials Science*, vol. 54, no. 4, pp. 2787–2795, 2019.

[96] V. Chesnokov, V. Luchihina, and I. Prosvirin, "Effect of the carbon nanomaterials structure on silica carbothermal reduction," *Diamond and Related Materials*, vol. 60, pp. 14–19, 2015.

[97] T. Taguchi, S. Yamamoto, K. Kodama, and H. Asaoka, "Synthesis of heterostructured sic and c–sic nanotubes by ion irradiation-induced changes in crystallinity," *Carbon*, vol. 95, pp. 279–285, 2015.

[98] T. Taguchi, S. Yamamoto, and H. Ohba, "Synthesis and formation mechanism of novel double-thick-walled silicon carbide nanotubes from multiwalled carbon nanotubes," *Applied Surface Science*, vol. 551, p. 149 421, 2021.

[99] Y. Zhang, L. Sheng, Y. Fang, *et al.*, "Synthesis of 3c-sic nanowires from a graphene/si configuration obtained by arc discharge method," *Chemical Physics Letters*, vol. 678, pp. 17–22, 2017.

[100] Q. Wang, Y. Li, S. Jin, and S. Sang, "Catalyst-free hybridization of silicon carbide whiskers and expanded graphite by vapor deposition method," *Ceramics International*, vol. 41, no. 10, pp. 14 359–14 366, 2015.

[101] Y. Liu, H. Hou, X. He, and W. Yang, "Mesporous 3 c-sic hollow fibers," *Scientific Reports*, vol. 7, no. 1, p. 1893, 2017.

[102] H. Chen, J. Jiang, and H. Zhao, "Synthesis of highly dispersed silicon carbide powders by a solvothermal-assisted sol–gel process," *Applied Physics A*, vol. 124, pp. 1–5, 2018.

[103] M. Li, L. Jiang, Y. Sun, T. Xiao, P. Xiang, and X. Tan, "Synthesis and structural evolution of hydrogenated amorphous silicon carbide thin film with carbon nanostructures," *Journal of Non-Crystalline Solids*, vol. 503, pp. 252–259, 2019.

[104] M. Zhang, J. Zhao, Z. Li, *et al.*, "Bamboo-like 3c-sic nanowires with periodical fluctuating diameter: Homogeneous synthesis, synergistic growth mechanism, and their luminescence properties," *Journal of Solid State Chemistry*, vol. 243, pp. 247–252, 2016.

[105] W. Wang, Y. Wang, L. Gu, *et al.*, "Sic@ si core–shell nanowires on carbon paper as a

hybrid anode for lithium-ion batteries," *Journal of Power Sources*, vol. 293, pp. 492–497, 2015.

[106] Y. Hua, S. Bai, H. Wan, X. Chen, T. Hu, and J. Gong, "Research on controllable synthesis of silicon carbide whiskers and particles on graphite by chemical vapor reaction," *Journal of Materials Science*, vol. 54, no. 3, pp. 2016–2024, 2019.

[107] J. Liang, S. Nishida, M. Arai, and N. Shigekawa, "Effects of thermal annealing process on the electrical properties of p+-si/n-sic heterojunctions," *Applied Physics Letters*, vol. 104, no. 16, 2014.

[108] A. Pérez-Tomás, M. Jennings, M. Davis, *et al.*, "Characterization and modeling of nn si/sic heterojunction diodes," *Journal of applied physics*, vol. 102, no. 1, 2007.

[109] M. Hoshi, T. Hayashi, H. Tanaka, and S. Yamagami, "Novel sic power devices utilizing a si/4h-sic heterojunction," in *2007 Power Conversion Conference-Nagoya*, IEEE, 2007, pp. 373–376.

[110] T. Hayashi, Y. Shimoida, H. Tanaka, S. Yamagami, S. Tanimoto, and M. Hoshi, "Novel power si/4h-sic heterojunction tunneling transistor (hett)," in *Materials science forum*, Trans Tech Publ, vol. 527, 2006, pp. 1453–1456.

[111] A. Nazarov, Y. N. Vovk, V. Lysenko, V. Turchanikov, V. Scryshevskii, and S. Ashok, "Carrier transport in amorphous sic/crystalline silicon heterojunctions," *Journal of Applied Physics*, vol. 89, no. 8, pp. 4422–4428, 2001.

[112] P. Gammon, A. Pérez-Tomás, M. Jennings, *et al.*, "Interface characteristics of nn and pn ge/sic heterojunction diodes formed by molecular beam epitaxy deposition," *Journal of Applied Physics*, vol. 107, no. 12, 2010.

[113] H. Hanafusa, A. Ohta, R. Ashihara, *et al.*, "Properties of al ohmic contacts to n-type 4h-sic employing a phosphorus-doped and crystallized amorphous-silicon interlayer," in *Materials Science Forum*, Trans Tech Publ, vol. 778, 2014, pp. 649–652.

[114] R. Anderson, "Germanium-gallium arsenide heterojunctions," *IBM Journal of Research and Development*, vol. 4, no. 3, pp. 283–287, 1960.

[115] M. Zimmermann, N. Lindlein, R. Voelkel, and K. J. Weible, "Microlens laser beam homogenizer: From theory to application," in *Laser Beam Shaping VIII*, SPIE, vol. 6663, 2007, pp. 9–21.

[116] K. Kanzler and A. Stockham, "Diffractive laser beam shaping for holography," in *Laser Beam Shaping X*, SPIE, vol. 7430, 2009, pp. 41–46.

[117] B. R. Frieden, "Lossless conversion of a plane laser wave to a plane wave of uniform

irradiance," *Applied Optics*, vol. 4, no. 11, pp. 1400–1403, 1965.

[118] M. Chen, J. Berkowitz-Mattuck, and P. Glaser, "The use of a kaleidoscope to obtain uniform flux over a large area in a solar or arc imaging furnace," *Applied Optics*, vol. 2, no. 3, pp. 265–271, 1963.

[119] Z. Wang, G. Zhu, Y. Huang, X. Zhu, and C. Zhu, "Analytical model of microlens array system homogenizer," *Optics & Laser Technology*, vol. 75, pp. 214–220, 2015.

[120] L. Yong and H. Jiasheng, "Laser beam shaping techniques," *Laser journal*, vol. 29, no. 6, pp. 1–4, 2008.

[121] R. Voelkel and K. J. Weible, "Laser beam homogenizing: Limitations and constraints," in *Optical Fabrication, Testing, and Metrology III*, SPIE, vol. 7102, 2008, pp. 222–233.

[122] F. La Via, A. Severino, R. Anzalone, *et al.*, "From thin film to bulk 3c-sic growth: Understanding the mechanism of defects reduction," *Materials Science in Semiconductor Processing*, vol. 78, pp. 57–68, 2018.

[123] D. Mendez, A. Aouni, F. Morales, *et al.*, "Defect morphology and strain of cvd grown 3c–sic layers: Effect of the carbonization process," *physica status solidi (a)*, vol. 202, no. 4, pp. 561–565, 2005.

[124] K.-T. Lin, H. Lin, and B. Jia, "Plasmonic nanostructures in photodetection, energy conversion and beyond," *Nanophotonics*, vol. 9, no. 10, pp. 3135–3163, 2020.

[125] X. Chen, B. Jia, J. K. Saha, *et al.*, "Broadband enhancement in thin-film amorphous silicon solar cells enabled by nucleated silver nanoparticles," *Nano letters*, vol. 12, no. 5, pp. 2187–2192, 2012.

[126] H. A. Atwater and A. Polman, "Plasmonics for improved photovoltaic devices," *Materials for sustainable energy: a collection of peer-reviewed research and review articles from Nature Publishing Group*, pp. 1–11, 2011.

[127] S. Pillai, K. Catchpole, T. Trupke, and M. Green, "Surface plasmon enhanced silicon solar cells," *Journal of applied physics*, vol. 101, no. 9, p. 093 105, 2007.

[128] L. Y. Tobing, G.-Y. Goh, A. D. Mueller, L. Ke, Y. Luo, and D.-H. Zhang, "Polarization invariant plasmonic nanostructures for sensing applications," *Scientific reports*, vol. 7, no. 1, pp. 1–14, 2017.

[129] C. Clavero, "Plasmon-induced hot-electron generation at nanoparticle/metal-oxide interfaces for photovoltaic and photocatalytic devices," *Nature Photonics*, vol. 8, no. 2, pp. 95–103, 2014.

[130] S. Mubeen, J. Lee, N. Singh, S. Krämer, G. D. Stucky, and M. Moskovits, "An autonomous photosynthetic device in which all charge carriers derive from surface plasmons," *Nature nanotechnology*, vol. 8, no. 4, pp. 247–251, 2013.

[131] Y. Tian and T. Tatsuma, "Mechanisms and applications of plasmon-induced charge separation at tio2 films loaded with gold nanoparticles," *Journal of the American Chemical Society*, vol. 127, no. 20, pp. 7632–7637, 2005.

[132] M. Moskovits, "The case for plasmon-derived hot carrier devices," *Nature Nanotechnology*, vol. 10, no. 1, pp. 6–8, 2015.

[133] S. M. Sze, Y. Li, and K. K. Ng, *Physics of semiconductor devices*. John wiley & sons, 2021.

[134] E. J. Santos and E. Kaxiras, "Electrically driven tuning of the dielectric constant in mos_2 layers," *ACS nano*, vol. 7, no. 12, pp. 10 741–10 746, 2013.

[135] P. K. Jain, S. Eustis, and M. A. El-Sayed, "Plasmon coupling in nanorod assemblies: Optical absorption, discrete dipole approximation simulation, and exciton-coupling model," *The Journal of Physical Chemistry B*, vol. 110, no. 37, pp. 18 243–18 253, 2006.

[136] D. A. Genov, A. K. Sarychev, V. M. Shalaev, and A. Wei, "Resonant field enhancements from metal nanoparticle arrays," *Nano Letters*, vol. 4, no. 1, pp. 153–158, 2004.

[137] K.-S. Lee and M. A. El-Sayed, "Gold and silver nanoparticles in sensing and imaging: Sensitivity of plasmon response to size, shape, and metal composition," *The Journal of Physical Chemistry B*, vol. 110, no. 39, pp. 19 220–19 225, 2006.

[138] M. W. Knight, Y. Wang, A. S. Urban, *et al.*, "Embedding plasmonic nanostructure diodes enhances hot electron emission," *Nano letters*, vol. 13, no. 4, pp. 1687–1692, 2013.

[139] A. Sobhani, M. W. Knight, Y. Wang, *et al.*, "Narrowband photodetection in the near-infrared with a plasmon-induced hot electron device," *Nature communications*, vol. 4, no. 1, pp. 1–6, 2013.

[140] J. Li, C. Nie, F. Sun, *et al.*, "Enhancement of the photoresponse of monolayer mos_2 photodetectors induced by a nanoparticle grating," *ACS applied materials & interfaces*, vol. 12, no. 7, pp. 8429–8436, 2020.

[141] X. Liu, T. Galfsky, Z. Sun, *et al.*, "Strong light–matter coupling in two-dimensional atomic crystals," *Nature Photonics*, vol. 9, no. 1, pp. 30–34, 2015.

[142] R. S. Kim, J. Zhu, J. H. Park, *et al.*, "E-beam deposited ag-nanoparticles plasmonic organic solar cell and its absorption enhancement analysis using fdtd-based cylindrical nano-particle optical model," *Optics express*, vol. 20, no. 12, pp. 12 649–12 657, 2012.

[143] G.-Y. Yao, Q.-L. Liu, and Z.-Y. Zhao, "Studied localized surface plasmon resonance effects of au nanoparticles on tio2 by fdtd simulations," *Catalysts*, vol. 8, no. 6, p. 236, 2018.

[144] R. Pan, J. Kang, Y. Li, Z. Zhang, R. Li, and Y. Yang, "Highly enhanced photoluminescence of monolayer mos_2 in plasmonic hybrids with double-layer stacked ag nanoparticles," *ACS Applied Materials & Interfaces*, vol. 14, no. 10, pp. 12 495–12 503, 2022.

[145] Y. Huang, E. Sutter, N. N. Shi, *et al.*, "Reliable exfoliation of large-area high-quality flakes of graphene and other two-dimensional materials," *ACS nano*, vol. 9, no. 11, pp. 10 612–10 620, 2015.

[146] A. Akbari and P. Berini, "Schottky contact surface-plasmon detector integrated with an asymmetric metal stripe waveguide," *Applied Physics Letters*, vol. 95, no. 2, p. 021 104, 2009.

[147] M. L. Brongersma, N. J. Halas, and P. Nordlander, "Plasmon-induced hot carrier science and technology," *Nature nanotechnology*, vol. 10, no. 1, pp. 25–34, 2015.

[148] B. Y. Zheng, H. Zhao, A. Manjavacas, M. McClain, P. Nordlander, and N. J. Halas, "Distinguishing between plasmon-induced and photoexcited carriers in a device geometry," *Nature communications*, vol. 6, no. 1, p. 7797, 2015.

[149] M. W. Knight, H. Sobhani, P. Nordlander, and N. J. Halas, "Photodetection with active optical antennas," *Science*, vol. 332, no. 6030, pp. 702–704, 2011.

[150] J. Lee, S. Yang, J. Lee, *et al.*, "Extraordinary optical transmission and second harmonic generation in sub–10-nm plasmonic coaxial aperture," *Nanophotonics*, vol. 9, no. 10, pp. 3295–3302, 2020.

[151] H. Im, K. C. Bantz, N. C. Lindquist, C. L. Haynes, and S.-H. Oh, "Vertically oriented sub-10-nm plasmonic nanogap arrays," *Nano letters*, vol. 10, no. 6, pp. 2231–2236, 2010.

[152] A. Bagnall, W. Liang, E. Marseglia, and B. Welber, "Raman studies of mos_2 at high pressure," *Physica B+ C*, vol. 99, no. 1-4, pp. 343–346, 1980.

[153] A. R. Izadpour, H. D. Jahromi, and M. H. Sheikhi, "Plasmonic enhancement of colloidal quantum dot infrared photodetector photosensitivity," *IEEE Journal of Quantum Electronics*, vol. 54, no. 3, pp. 1–7, 2018.

[154] J. Olesiak-Banska, M. Waszkielewicz, P. Obstarczyk, and M. Samoc, "Two-photon absorption and photoluminescence of colloidal gold nanoparticles and nanoclusters," *Chemical society reviews*, vol. 48, no. 15, pp. 4087–4117, 2019.

[155] M. Hu and G. V. Hartland, "Heat dissipation for au particles in aqueous solution: Relaxation time versus size," *The Journal of Physical Chemistry B*, vol. 106, no. 28, pp. 7029–7033,

2002.

[156] X. Chen, Y. Chen, M. Yan, and M. Qiu, "Nanosecond photothermal effects in plasmonic nanostructures," *ACS nano*, vol. 6, no. 3, pp. 2550–2557, 2012.

[157] E. L. Radue, J. A. Tomko, A. Giri, *et al.*, "Hot electron thermoreflectance coefficient of gold during electron–phonon nonequilibrium," *Acs Photonics*, vol. 5, no. 12, pp. 4880–4887, 2018.

[158] J. Wang, Y. Xun, X. Liu, S. Yu, and N. Jiang, "Soft switching circuit of high-frequency active neutral point clamped inverter based on SiC/Si hybrid device," *Journal of Power Electronics*, vol. 21, no. 1, pp. 71–84, 2021.

[159] F. Roccaforte, P. Fiorenza, G. Greco, *et al.*, "Emerging trends in wide band gap semiconductors (SiC and GaN) technology for power devices," *Microelectronic Engineering*, vol. 187, pp. 66–77, 2018.

[160] U. K. Mishra, L. Shen, T. E. Kazior, and Y.-F. Wu, "GaN-based RF power devices and amplifiers," *Proceedings of the IEEE*, vol. 96, no. 2, pp. 287–305, 2008.

[161] C. Dimitrakopoulos, Y.-M. Lin, A. Grill, *et al.*, "Wafer-scale epitaxial graphene growth on the Si-face of hexagonal SiC (0001) for high frequency transistors," *Journal of Vacuum Science & Technology B, Nanotechnology and Microelectronics: Materials, Processing, Measurement, and Phenomena*, vol. 28, no. 5, pp. 985–992, 2010.

[162] P. Yih, J. Li, and A. Steckl, "SiC/Si heterojunction diodes fabricated by self-selective and by blanket rapid thermal chemical vapor deposition," *IEEE Transactions on Electron Devices*, vol. 41, no. 3, pp. 281–287, 1994. DOI: 10.1109/16.275210.

[163] A. Kaur, T. Hogan, and P. Chahal, "Selective fabrication of sic/si heterojunction diodes by local laser annealing process for microwave circuit applications," *IEEE Journal of the Electron Devices Society*, vol. 5, no. 5, pp. 291–298, 2017.

[164] M. Darif, N. Semmar, and F. Orléans Cedex, "Numerical simulation of si nanosecond laser annealing by comsol multiphysics," in *Proceedings of the COMSOL Conference 2008 Hannover*, 2008, pp. 567–571.

[165] T. Trupke, E. Daub, and P. Würfel, "Absorptivity of silicon solar cells obtained from luminescence," *Solar energy materials and solar cells*, vol. 53, pp. 103–114, 1-2 1998, ISSN: 0927-0248.

[166] L. Shamsuddin, S. S. MdIzah, and K. Mohamed, "Comparative study of pmma 120k and 996k for electron beam lithography application," *Australian Journal of Basic and Applied Sciences*, vol. 15, pp. 55–58, 2014.

[167] P. Prathap, J. Bartringer, and A. Slaoui, "Selective emitter formation by laser doping of spin-on sources," *Applied surface science*, vol. 278, pp. 173–179, 2013.

[168] S. Coutanson, E. Fogarassy, and J. Venturini, "Mechanisms and application of the excimer laser doping from spin-on glass sources for usj fabrication," *Applied surface science*, vol. 252, no. 13, pp. 4502–4505, 2006.

[169] A. Jiménez, E. Napolitani, A. Datas, *et al.*, "N-type doping of sic-passivated ge by pulsed laser melting towards the development of interdigitated back contact thermophotovoltaic devices," *Solar Energy Materials and Solar Cells*, vol. 235, p. 111 463, 2022.

[170] K. Imokawa, T. Kurashige, A. Suwa, *et al.*, "Fabrication of cmos invertors in si thin-film-transistors by laser doping using a chemical solution coating," *IEEE Journal of the Electron Devices Society*, vol. 8, pp. 27–32, 2019.

[171] C.-H. Kim, S.-H. Jung, J.-H. Jeon, and M.-K. Han, "A simple low-temperature laser-doping employing phosphosilicate glass and borosilicate glass films for the source and drain formation in poly-si thin film transistors," *Thin solid films*, vol. 397, no. 1-2, pp. 4–7, 2001.

[172] S. Zhang, R. Li, Z. Yao, *et al.*, "Laser annealing towards high-performance monolayer mos_2 and wse2 field effect transistors," *Nanotechnology*, vol. 31, no. 30, 30LT02, 2020.

[173] E. Paneerselvam, N. J. Vasa, D. Nakamura, *et al.*, "Pulsed laser deposition of sic thin films and influence of laser-assisted annealing," *Materials Today: Proceedings*, vol. 35, pp. 312–317, 2021.

[174] D. A. Long, "Raman spectroscopy," *New York*, vol. 1, 1977.

[175] B. H. Hokr, J. N. Bixler, G. D. Noojin, *et al.*, "Single-shot stand-off chemical identification of powders using random raman lasing," *Proceedings of the National Academy of Sciences*, vol. 111, no. 34, pp. 12 320–12 324, 2014.

[176] P. Venezuela, M. Lazzeri, and F. Mauri, "Theory of double-resonant raman spectra in graphene: Intensity and line shape of defect-induced and two-phonon bands," *Physical Review B*, vol. 84, no. 3, p. 035 433, 2011.

[177] L. Malard, M. A. Pimenta, G. Dresselhaus, and M. Dresselhaus, "Raman spectroscopy in graphene," *Physics reports*, vol. 473, no. 5-6, pp. 51–87, 2009.

[178] R. Yan, J. R. Simpson, S. Bertolazzi, *et al.*, "Thermal conductivity of monolayer molybdenum disulfide obtained from temperature-dependent raman spectroscopy," *ACS nano*, vol. 8, no. 1, pp. 986–993, 2014.

[179] J. K. Seo, Y.-H. Joung, Y. Park, and W. S. Choi, "Substrate temperature effect on the sic

passivation layer synthesized by an rf magnetron sputtering method," *Thin Solid Films*, vol. 519, no. 20, pp. 6654–6657, 2011.

[180] Z. Feng, A. Mascarenhas, W. Choyke, and J. Powell, "Raman scattering studies of chemical-vapor-deposited cubic sic films of (100) si," *Journal of applied physics*, vol. 64, no. 6, pp. 3176–3186, 1988.

[181] J. Wasyluk, T. S. Perova, S. A. Kukushkin, A. V. Osipov, N. A. Feoktistov, and S. A. Grudinkin, "Raman investigation of different polytypes in sic thin films grown by solid-gas phase epitaxy on si (111) and 6h-sic substrates," in *Materials science forum*, Trans Tech Publ, vol. 645, 2010, pp. 359–362.

[182] B. Wang, J. Yin, D. Chen, *et al.*, "Optical and surface properties of 3c–sic thin epitaxial films grown at different temperatures on 4h–sic substrates," *Superlattices and Microstructures*, vol. 156, p. 106 960, 2021.

[183] J. Zhu, S. Liu, and J. Liang, "Raman study on residual strains in thin 3c-sic epitaxial layers grown on si (001)," *Thin Solid Films*, vol. 368, no. 2, pp. 307–311, 2000.

[184] D. B. Chrisey and G. K. Hubler, "Pulsed laser deposition of thin films. john whiley and sons," *New York, NY*, 1994.

[185] A. Piqué, "The matrix-assisted pulsed laser evaporation (maple) process: Origins and future directions," *Applied Physics A*, vol. 105, pp. 517–528, 2011.

[186] L. F. Alves, R. C. Gomes, P. Lefranc, *et al.*, "Sic power devices in power electronics: An overview," in *2017 Brazilian Power Electronics Conference (COBEP)*, IEEE, 2017, pp. 1–8.

[187] R. T. Yadlapalli, A. Kotapati, R. Kandipati, and C. S. Koritala, "A review on energy efficient technologies for electric vehicle applications," *Journal of Energy Storage*, vol. 50, p. 104 212, 2022.

[188] I. Mazumder, A. Biswas, and C. Mondal, "4h-sic semi-circle gate power mosfet with low on-resistance and high breakdown voltage," in *2022 IEEE Calcutta Conference (CALCON)*, IEEE, 2022, pp. 80–83.

[189] D. Bharti and A. Islam, "Optimization of sic umosfet structure for improvement of breakdown voltage and on-resistance," *IEEE Transactions on Electron Devices*, vol. 65, no. 2, pp. 615–621, 2017.

[190] R. N. Simons and P. G. Neudeck, "Intermodulation-distortion performance of silicon-carbide schottky-barrier rf mixer diodes," *IEEE transactions on microwave theory and techniques*, vol. 51, no. 2, pp. 669–672, 2003.

[191] Z. Shen, J. Chen, B. Li, G. Li, Z. Zhang, and X. Hou, "Recent progress in sic nanowires as electromagnetic microwaves absorbing materials," *Journal of Alloys and Compounds*, vol. 815, p. 152 388, 2020.

[192] R. S. Pengelly, S. M. Wood, J. W. Milligan, S. T. Sheppard, and W. L. Pribble, "A review of gan on sic high electron-mobility power transistors and mmics," *IEEE Transactions on Microwave Theory and Techniques*, vol. 60, no. 6, pp. 1764–1783, 2012.

[193] T. Xun, Y. Zhao, H. Yang, *et al.*, "Developments of pulsed electron beam sources for high-power microwave applications," *IEEE Access*, vol. 8, pp. 101 351–101 358, 2020.

[194] D. M. Lukin, C. Dory, M. A. Guidry, *et al.*, "4h-silicon-carbide-on-insulator for integrated quantum and nonlinear photonics," *Nature Photonics*, vol. 14, no. 5, pp. 330–334, 2020.

[195] N. Morioka, C. Babin, R. Nagy, *et al.*, "Spin-controlled generation of indistinguishable and distinguishable photons from silicon vacancy centres in silicon carbide," *Nature communications*, vol. 11, no. 1, p. 2516, 2020.

[196] W. Qi, M. Li, and L. Zhao, "One-step fabrication of photoluminescent sic quantum dots through a radiation technique," *New Journal of Chemistry*, vol. 44, no. 31, pp. 13 301–13 307, 2020.

[197] A. Moridi, H. Ruan, L. Zhang, and M. Liu, "Residual stresses in thin film systems: Effects of lattice mismatch, thermal mismatch and interface dislocations," *International Journal of Solids and Structures*, vol. 50, no. 22-23, pp. 3562–3569, 2013.

[198] F. Medjdoub, M. Zegaoui, B. Grimbert, D. Ducatteau, N. Rolland, and P. Rolland, "First demonstration of high-power gan-on-silicon transistors at 40 ghz," *IEEE electron device letters*, vol. 33, no. 8, pp. 1168–1170, 2012.

[199] N. Nepal, D. S. Katzer, B. P. Downey, *et al.*, "Heteroepitaxial growth of β-ga2o3 films on sic via molecular beam epitaxy," *Journal of Vacuum Science & Technology A: Vacuum, Surfaces, and Films*, vol. 38, no. 6, p. 063 406, 2020.

[200] A. Fissel, B. Schröter, and W. Richter, "Low-temperature growth of sic thin films on si and 6h–sic by solid-source molecular beam epitaxy," *Applied physics letters*, vol. 66, no. 23, pp. 3182–3184, 1995.

[201] Q. Cheng, S. Xu, J. Long, and K. Ostrikov, "Low-temperature pecvd of nanodevice-grade nc-3c-sic," *Chemical Vapor Deposition*, vol. 13, no. 10, pp. 561–566, 2007.

[202] E. Fitzgerald, "The effect of substrate growth area on misfit and threading dislocation densities in mismatched heterostructures," *Journal of Vacuum Science & Technology B: Microelectronics Processing and Phenomena*, vol. 7, no. 4, pp. 782–788, 1989.

[203] G. Ferro, "3c-sic heteroepitaxial growth on silicon: The quest for holy grail," *Critical Reviews in Solid State and Materials Sciences*, vol. 40, no. 1, pp. 56–76, 2015.

[204] Y. Wang, S. Dong, X. Li, C. Hong, and X. Zhang, "Synthesis, properties, and multifarious applications of sic nanoparticles: A review," *Ceramics International*, vol. 48, no. 7, pp. 8882–8913, 2022.

[205] A. Najafi, F. Golestani-Fard, and H. Rezaie, "Improvement of sic nanopowder synthesis by sol–gel method via teos/resin phenolic precursors," *Journal of Sol-Gel Science and Technology*, vol. 75, pp. 255–263, 2015.

[206] X. Yu, S. Terakawa, S. Hayashi, *et al.*, "Carbonization of silicon nanoparticles via ablation induced by femtosecond laser pulses in hexane," *Arabian Journal for Science and Engineering*, vol. 42, pp. 4221–4226, 2017.

[207] S. Manikandan and J. Jancirani, "A study of preparation and characterization of nano-sized sic powder using high energy ball milling," in *Applied Mechanics and Materials*, Trans Tech Publ, vol. 592, 2014, pp. 13–17.

[208] D. Beke, J. Valenta, G. Károlyházy, *et al.*, "Room-temperature defect qubits in ultrasmall nanocrystals," *The Journal of Physical Chemistry Letters*, vol. 11, no. 5, pp. 1675–1681, 2020.

[209] Y. Zhong, L. L. Shaw, M. Manjarres, and M. F. Zawrah, "Synthesis of silicon carbide nanopowder using silica fume," *Journal of the American Ceramic Society*, vol. 93, no. 10, pp. 3159–3167, 2010.

[210] R. Ma, J. Shi, W. Lin, and J. Chen, "Synthesis and sintering of nanocrystalline sic ceramic powders," *Materials Chemistry and Physics*, vol. 253, p. 123 445, 2020.

[211] S.-M. Ko, S.-M. Koo, W.-S. Cho, K.-T. Hwnag, and J.-H. Kim, "Synthesis of sic nanopowder from organic precursors using rf inductively coupled thermal plasma," *Ceramics international*, vol. 38, no. 3, pp. 1959–1963, 2012.

[212] J. P. Singh and S. N. Thakur, *Laser-induced breakdown spectroscopy*. Elsevier, 2020.

[213] G. Wei, W. Qin, G. Wang, *et al.*, "The synthesis and ultraviolet photoluminescence of 6h–sic nanowires by microwave method," *Journal of Physics D: Applied Physics*, vol. 41, no. 23, p. 235 102, 2008.

[214] S. G. Sundaresan, A. V. Davydov, M. D. Vaudin, *et al.*, "Growth of silicon carbide nanowires by a microwave heating-assisted physical vapor transport process using group viii metal catalysts," *Chemistry of Materials*, vol. 19, no. 23, pp. 5531–5537, 2007.

[215] S. Zhou, X. Pi, Z. Ni, *et al.*, "Comparative study on the localized surface plasmon resonance

of boron-and phosphorus-doped silicon nanocrystals," *ACS nano*, vol. 9, no. 1, pp. 378–386, 2015.

[216] K. Fu, H. Fu, X. Huang, *et al.*, "Reverse leakage analysis for as-grown and regrown vertical gan-on-gan schottky barrier diodes," *IEEE Journal of the Electron Devices Society*, vol. 8, pp. 74–83, 2020.

[217] L. Wang, C. Zhang, F. Liu, H. Zheng, and G. J. Cheng, "Ultrafast pulsed laser stealth dicing of 4h-sic wafer: Structure evolution and defect generation," *Journal of Manufacturing Processes*, vol. 81, pp. 562–570, 2022.

[218] J. Fan, H. Li, J. Jiang, L. K. So, Y. W. Lam, and P. K. Chu, "3c–sic nanocrystals as fluorescent biological labels," *Small*, vol. 4, no. 8, pp. 1058–1062, 2008.

[219] J. Jian and J. Sun, "A review of recent progress on silicon carbide for photoelectrochemical water splitting," *Solar RRL*, vol. 4, no. 7, p. 2 000 111, 2020.

[220] A. K. Agarwal, S. Seshadri, and L. B. Rowland, "Temperature dependence of fowler-nordheim current in 6h-and 4h-sic mos capacitors," *IEEE Electron Device Letters*, vol. 18, no. 12, pp. 592–594, 1997.

[221] M. Kauranen and A. V. Zayats, "Nonlinear plasmonics," *Nature photonics*, vol. 6, no. 11, pp. 737–748, 2012.